Université de Sherbrooke

Radiolysis of supercritical water (SCW) by radiations of different qualities: Formation of local, transient "acid spikes" at early times, and their consequences as potential sources of corrosion in proposed Generation IV SCW-cooled nuclear reactors. A Monte Carlo track chemistry simulation study

Par

Md Mohsin PATWARY

Département de médecine nucléaire et radiobiologie

Mémoire présenté à la Faculté de médecine et des sciences de la santé
en vue de l'obtention du diplôme de maître ès sciences (M.Sc.)
en sciences des radiations et imagerie biomédicale

Sherbrooke, Québec, Canada
Janvier 2019

Membres du jury d'évaluation

Pr Armand SOLDERA, Département de chimie, Faculté des sciences
Pr Richard J. WAGNER, Département de médecine nucléaire et radiobiologie
Pr Jean-Paul JAY-GERIN, Département de médecine nucléaire et radiobiologie

RÉSUMÉ

Étude par simulation Monte Carlo de la radiolyse de l'eau supercritique par des radiations de différentes qualités : formation *in situ* de « pics d'acidité » transitoires aux temps courts, et leurs conséquences comme sources potentielles de corrosion dans les réacteurs nucléaires de quatrième génération refroidis à l'eau supercritique

Par

Md Mohsin Patwary

Département de médecine nucléaire et radiobiologie

Mémoire présenté à la Faculté de médecine et des sciences de la santé en vue de l'obtention du diplôme de maître ès sciences (M.Sc.) en sciences des radiations et imagerie biomédicale, Faculté de médecine et des sciences de la santé, Université de Sherbrooke, Sherbrooke, Québec, Canada, J1H 5N4

La chimie sous rayonnement est un domaine d'études fort diversifié. Les industries nucléaires, où s'inscrit le récent projet de réacteurs dit de « quatrième génération » (Gen-IV), s'intéressent principalement à la chimie de l'eau qui intervient dans le cœur des réacteurs, pour des raisons évidentes de coûts et de sécurité. L'eau supercritique (ESC) est un liquide de refroidissement potentiel ayant été proposé pour être utilisé dans l'un des concepts possibles du projet nucléaire Gen-IV. Dans la présente étude, la chimie sous rayonnement de l'ESC à 400 °C a été examinée à l'aide de simulations Monte Carlo, en se concentrant sur les « pics d'acidité » transitoires ultra-rapides qui se forment le long des trajectoires du rayonnement. Cette radiolyse a été effectuée avec des neutrons de 2 MeV et des protons de 300 MeV dans le but de rendre compte des rayonnements à fort et faible transferts d'énergie linéaire (TEL) qui existent au sein d'un réacteur. Nos programmes de simulation ont été adaptés pour tenir compte des propriétés exceptionnelles de l'ESC à 400 °C, et aussi pour permettre de réaliser notre étude en fonction de la densité de l'eau (entre 0,15 et 0,6 g/cm^3). Les résultats de nos simulations ont été comparés au peu de données expérimentalement disponibles, ainsi qu'aux données obtenus à l'aide du logiciel SRIM (« Stopping and Range of Ions in Matter »). Ces comparaisons étaient nécessaires, car un certain nombre d'approximations ont dû être faites lors de l'élaboration de nos programmes. En plus des différentes espèces importantes générées par la radiolyse (e^-_{aq}, $^\bullet OH$, H_2O_2, H_2, *etc.*), nous avons aussi observé la formation d'un nombre substantiel de protons (H^+) le long des trajectoires de rayonnements autant à fort et faible TEL et pour toutes les densités d'eau considérées. Nos simulations ont ainsi permis de calculer et de quantifier les variations locales d'acidité correspondantes avec le temps. Nous avons trouvé des valeurs de pH aussi faibles que ~1 aux temps les plus courts, valeurs qui augmentaient peu à peu après un certain temps jusqu'à atteindre la neutralité. La durée et l'ampleur de cette acidité locale peuvent inciter l'expérimentateur à examiner le rôle probable qu'elle peut jouer en termes de corrosion dans les réacteurs refroidis à l'ESC.

Mots-clés: Radiolyse de l'eau, transfert d'énergie linéaire (TEL), température, simulations Monte Carlo, rendements radicalaires et moléculaires, pH, effet des « pics d'acidité » dans les trajectoires en fonction du temps, corrosion.

ABSTRACT

Radiolysis of supercritical water (SCW) by radiations of different qualities: Formation of local, transient "acid spikes" at early times, and their consequences as potential sources of corrosion in proposed Generation IV SCW-cooled nuclear reactors. A Monte Carlo track chemistry simulation study.

By

Md Mohsin Patwary

Département de médecine nucléaire et radiobiologie

Thesis presented at the Faculty of Medicine and Health Sciences in order to obtain the Master of Sciences (M.Sc.) degree in Radiation Sciences and Biomedical Imaging, Faculty of Medicine and Health Sciences, Université de Sherbrooke, Sherbrooke, Québec, Canada, J1H 5N4

The domain of study of radiation chemistry is diversified. Nuclear industries, where Gen-IV project is the newest edition, are especially concerned with the radiation chemistries inside the nuclear reactor core, as various issues of costs and safeties are always involved. Supercritical water (SCW) is a potential reactor coolant that may be used in one of the possible designs of the Gen-IV nuclear project. In this study, the radiation chemistry of supercritical water at 400 °C was looked into using Monte Carlo track chemistry simulations, focusing particularly on the generation of ultrafast transient "acid spikes" along the radiation track. In this work, radiolysis of supercritical water with 2 MeV neutrons and 300 MeV protons was studied to cover both the high and low linear energy transfer (LET) radiations that can possibly exist in the reactor. Our simulation programs were adapted to account for the exceptional properties of supercritical water as compared to water at a lower temperature, and to allow us to perform our study as a function of the density of water (0.15-0.6 g/cm^3). Data obtained from our simulations were compared with the few experimentally available data and with the data obtained with the SRIM ("Stopping and Range of Ions in Matter") software. These comparisons were necessary as a number of approximations had to be made during the development of our programs. In addition to the different important radiolytically generated species (including e^-_{aq}, $^\bullet OH$, H_2O_2, H_2, *etc.*), we also observed the formation of a substantial number of protons (H^+) along the radiation trajectories at low and high LET and for all water densities considered. Using our programs, we calculated and quantified the local variations of the pH along the track with time. We found pH values as low as ~1 at the shortest times, values that increased little by little after a certain time until reaching neutrality. The duration and magnitude of this local acidity may prompt the experimentalist to examine the likely role it may play in terms of corrosion in SCW-cooled reactors.

Keywords: Water radiolysis, linear energy transfer (LET), temperature, Monte Carlo simulations, radical and molecular yields, pH, "acid-spike" effect along the radiation tracks as a function of time, corrosion.

TABLE OF CONTENTS

LIST OF FIGURES

Chapter 1: Introduction

Chapter 3: Methodology

Chapter 4: Article (5 figures)

Chapter 5: Discussion

LIST OF TABLES

LIST OF ABBREVIATIONS

D	Diffusion coefficient
DEA	Dissociative electron attachment
DNA	Deoxyribonucleic acid
$\mathbf{e^-_{aq}}$	Hydrated electron
eV	Electron-volt
BWR	Boiling water reactor
***G*(X)**	Experimental yield of the final product X
PWR	Pressurized water reactor
IRT	Independent reaction times
k	Reaction rate constant
keV	Kilo electron-volts
LET	Linear energy transfer
SCW	Supercritical water
MeV	Mega electron-volts
µm	Micrometer
µs	Microsecond
ps	Picosecond
SCC	Stress corrosion cracking
ΔG	Cumulative yield variation
M	Molar (mol/L)
CAB	Core and Bond

1. INTRODUCTION

1.1. History and development of radiation chemistry

Radiation was discovered just slightly more than a century ago, with a profound prospect on both industry and medicine. The invention of radiation dates back to 1895, when Wilhelm Conrad Röntgen happened to discover the generation of X-rays from a cathode ray tube. In 1896, Henri Becquerel discovered another form of penetrating rays; natural phosphorescence or radioactivity of uranium. Around the same time, Marie Curie, a Polish scientist, discovered the radioactivity of polonium (Curie and Curie, 1898*a*) and radium (Curie et al., 1898*b*). It had been of so much importance to know the associated chemistry of radiation in different systems and the probable impact of it on those media, just from the beginning, when radiation was started to be used for different purposes including medicinal applications. The study of radiation chemistry involves the determination of the types of intermediate species, their chemical evolution and the types of chemical reactions possible between the species. The importance of this study became obvious after the incorporation of first powerful X-ray machines in 1930 and concerns were grown up on the probable biological impact of this low LET radiation on the human body.

The first suggestion that radiation through water splits it up, came from the work of Debierne (1914) who first hypothesized that water was broken down into $H^{\bullet}$ and $^{\bullet}OH$ radicals. However, much experimental evidence was not supporting the idea. Later, it was suggested by Risse (1930) and Fricke (1935) that radiation produced "activated water" instead. This activated water, in the presence of enough concentration of solutes, would give different types of products. And to see the impact of activated water, it would be important to keep the solute concentration as low as possible. The study of radiation chemistry got a boost during World War-II, when the collaborative works between Canada and USA, to see the impact of radiation and radiolysis products on the stability of materials, were being done extensively. These studies established the generation of different free radicals and reactive molecular products from radiolysis of water (Jonah, 1995; Jonah and Rao, 2001).

During all of the last century, radiation chemistry advanced a lot. A number of various factors and mechanisms have been explained and established. It is now established that liquid-phase radiation chemistry of water produces primarily e^-_{aq}, $H^\bullet$, H_2, $^\bullet OH$, H_2O_2, H^+, OH^-, and a little of $HO_2^\bullet$. A number of works on all the mechanisms involved with these species has also been done. After the first experimental proof of the existence of the hydrated electron in irradiated solution by Hart and Boag (1962) (see also Hart and Anbar, 1970), numerous research works were published to understand the influence of the pH, the temperature, the ionic character and the isotopic substitution on the absorption spectrum (Herbert and Coons, 2017) of this species. This species continues to attract significant attention due to its role in radiation chemistry, including in DNA damage, and because questions persist regarding its detailed structure in bulk (Ichino and Fessenden, 2007). The redox potential of the solvated electron was accurately measured using both experimental and theoretical measurements and its relative propensity to react with nucleobases to ultimately produce different types of products has also been determined (Ma et al., 2017). A number of different studies on the precursor of this solvated electron (often named as “dry” or “presolvated” electrons) were also made. An extensive research has also established that the bimolecular reactions of solvated electrons are responsible for the early stage generation of molecular hydrogen in the system. It is already established that these dry electrons can also influence the damage of the DNA bases and structure (Cadet et al., 2014; Ma et al., 2017). Owing to the very high reactivity of $^\bullet OH$ radicals, they take part quickly in different types of reactions (like radical transfer reactions) with the molecules in the system (Madugundu et al., 2013; von Sonntag, 2006). The hallmarks of the impact of $^\bullet OH$ radicals on DNA biomolecules has already been established (Balasubramanian et al., 1998). In this sequence, some work has also been done on the probable impact of radiolytically generated H^+ ions in different systems, especially the biological systems (Byakov and Stepanov, 2006; Kanike et al., 2015; Islam et al., 2018).

When radiation is to be used for various purposes, it is very important to know how much of the energy through radiation is provided to the system. The unit, in this case, is ‘dose’, which can be both based on radiation flux in the air or the amount absorbed by the medium. For calculating the dose, if the chemical system involves an

aqueous solution containing substances made, for example, of light-weight atoms, that solution will have absorption and scattering properties that will closely approximate the behaviour of tissue (Stenström and Lohmann, 1933). Fricke solution came first from this idea. Studies of the ferrous sulfate system, which was composed of aqueous ferrous sulfate in dilute sulfuric acid, revealed that the reaction was independent of the initial ferrous ion concentration from 4×10^{-5} to 10^{-2} M ferrous sulfate in 0.8 N sulfuric acid (Fricke and Morse, 1927, 1929). This led to the conclusion that the primary action of the rays was on the water, resulting in the production of active water molecules. By then, it was not yet established that water breaks down to produce different active species. Rather it was thought that irradiation produces a form of water named "activated water". The activated water molecules, then, transformed the ferrous ions into the ferric. As long as ferrous ions remained in solution, the percentage of ferrous ion transformed to ferric ions was linearly related to dose. It was also observed that the conversion was dependent on the concentration of oxygen in the solution. This was the first developmental stage of dissymmetry technique, which improved a lot later to account for the wide variation of solution characteristics, radiation types (like neutron beam) (Fricke and Hart, 1966) and to ensure authenticity and reproducibility. Later, a number of different modifications were done on this dosimeter. At present different types of other dosimetry techniques like gel dosimetry and alanine dosimetry have been started to be used (Baldock, 2009; Vaiente et al., 2016).

The study of radiation chemistry had been boosted up by the arrival of a technique known as pulse radiolysis in the 1960s, which was being extensively used for understanding the kinetics of irradiated systems. This technique was utilized in determining the reaction rate constants including the probable reactions between the species generated from radiolysis. By 1988, rate constants of almost 3000 reactions had been compiled and determined using this sensitive instrumental technique (Markovic, 1989). These rate constants for different reactions of the irradiated system not only paved the way to understand the mechanism undergoing into the system but also they were proved to be one of the most important tools for simulation of the irradiated system.

Nowadays, the domain of radiation chemistry has been diversified. The basic knowledge of radiation chemistry is now brought to the applied field. Various types of radiations are now being used for radio-therapeutic purposes. Radiation chemistry is thought to be a way to produce molecular hydrogen by the breaking down of water. A specialized section of Deep River ("Canadian Nuclear Laboratories", formerly "Atomic Agency of Canada Ltd."), Canada has been devoted to this purpose. The domain of radiation chemistry has even extended to astrology and astrophysics. The origin of life is now being correlated to the early age of meteoroids where radiation induced the production of amino acids, which is the fundamental element of proteins. Recently, for example, Esmaili et al. (2018) were able to mimic a condition of radiation similar to that of in meteoroids and this condition was found to produce amino acids. This will certainly be an addition to the ongoing research on how life was created in the Earth.

1.2. Radiation and radiolysis

Radiation can be described as energy or particles with certain energy from a source that travels through space or other media. Light, heat, microwaves and wireless communications are also different forms of radiation. When radiations are directed into an object or a medium, some of the radiating entities interact with the particles of the medium and energy of them can be absorbed or scattered. These absorption and scattering cause attenuation of the energy of radiation. The rest of the radiating entities may travel completely through the object even without interacting with any of the species of the medium. The most important types of interactions, with which the attenuation occurs, are excitation and ionization of the species of the medium. When the energy of the irradiating beam is enough to cross the ionization threshold, it produces ionization of the species of the medium. This ionizing beam of radiation can also be of two types, directly ionizing or indirectly ionizing. Directly ionizing radiations take out electrons due to the columbic interaction, as they carry charge (*e.g.*, proton beam, alpha rays, *etc.*), whereas an indirectly ionizing radiation ionizes a water molecule by removing an electron from the system. If the medium is water, excited or ionized water molecules are produced, which establish thermal and chemical equilibrium, later, and produce a number of different active species including free

radicals, ions and molecular products. These newly produced species diffuse in space in a three-dimensional way (taking the form of an expanding sphere, called a "spur") and take part in different reactions with various species in the medium (water, oxygen and other added species) or among themselves (Spinks and Woods, 1990; Ferradini and Jay-Gerin, 1999; Mozumder, 1999; Mozumder and Hatano, 2004; Hatano et al., 2011). After a certain time (~μs), the spur expansion is finished and the spurs merge to homogeneously distribute all the species throughout the medium. This breaking down of water and the subsequent stages of interaction afterwards are cumulatively called the radiolysis of water.

During water radiolysis, the extent of production of each individual species is expressed with the help of a "*G*-value". It represents the production of each individual species on a molecule/100 eV basis (for conversion into SI units (mol J^{-1}): 1 molecule/100 eV ≈ 1.0364×10^{-7} mol/J). *G*-values can be replaced with *g*-values, which are specific for the *primary* yield of species. The primary yield of species is defined as the yield of a species at the end of spur expansion and the beginning of the time where all the species are homogeneously distributed into the medium. For low-LET radiation, the radiolysis of pure, de-aerated (air-free) liquid water can be represented conceptually by the following global equation, written for an absorbed energy of 100 eV:

$$g(\text{-}H_2O)\ H_2O \longrightarrow g(e^-_{aq})\ e^-_{aq} + g(H^\bullet)\ H^\bullet + g(H_2)\ H_2 + g(H^+)\ H^+ + g(OH^-)\ OH^- + g(^\bullet OH)\ ^\bullet OH + g(H_2O_2)\ H_2O + g(HO_2^\bullet/O_2^{\bullet-})\ HO_2^\bullet/O_2^{\bullet-} + \ldots \quad (1.a)$$

For ^{60}Co γ-irradiated neutral water at 25 °C (Tippyamontri et al., 2009)

$g(e^-_{aq}) = 2.65$ $g(H^\bullet) = 0.6$ $g(H_2) = 0.45$ $g(^\bullet OH) = 2.8$

$g(H_2O_2) = 0.68$ molecule per 100 eV.

The yield of various species varies according to the type and energy of the radiation. For example, $HO_2^\bullet$ is a radiolytically generated primary product whose yield depends greatly on the LET ("linear energy transfer", described later) or amount of energy deposited.

These product yields are connected by the following equations:

$$g(e^-_{aq}) + g(OH^-) = g(H^+)$$

$$g(e^-_{aq}) + g(H^\bullet) + 2g(H_2) = g(^\bullet OH) + 2g(H_2O_2) + 3g(HO_2^\bullet/O_2^{\bullet-}). \quad (1.b)$$

One of the main goals in the study of the radiation chemistry of water is to determine the yields of radiolytically generated species and their time evolution, under different irradiation conditions. This study is important in understanding the fundamental processes undergoing during radiolysis, which later can be used for various applications.

1.3. How much energy is deposited: LET

Radiolysis of water happens when some energy from the irradiating beam is deposited into the medium. So, to understand the exact mechanism of radiolysis, it is very important to know the amount of energy transferred to the medium. The most pertinent qualitative description is that of the spatial distribution of the collisions by which the electrons (or other ionizing and exciting particles, which are responsible for the actual energy dissipation), lose their energy. This concept has been termed "linear energy transfer" (LET) and is defined in terms of the energy lost per unit path length by the particle (Danzker et al., 1959). This value is also termed as "stopping power" in radiation physics. Mathematically, it is expressed by the following formula:

$$\mathrm{LET} = -\frac{\mathrm{d}E}{\mathrm{d}x}, \quad (1.c)$$

where dE is the average energy locally (*i.e.*, in the vicinity of the particle track) transferred to the medium by the particle in traversing a distance dx (ICRU Report 16, 1970). Usually, LET values are expressed in units of keV per micron (keV/μm) (the conversion into SI units is: 1 keV/μm ≈ 1.602×10^{-19} J/nm). The LET is a function of properties of both the irradiating beam and the medium. For an irradiating beam, the energy, charge, and kinetic energies are the most deterministic factors of LET, whereas medium density, temperature, type of medium, *etc.*, are the properties of the medium that determine the LET. There are different theories and corresponding theoretical data on the determination of stopping power of charged particles in matter. Braggs rule on

stopping power was one of the most initial approaches in this case, which had been studied a lot later and recently some new additions (like the chemical binding effect) has been made to the original theory (Thwaites, 1983). Stopping range and power of different ions in a biological system have also been worked on in recent years (El-Ghossain, 2017). The Bethe theory of stopping power describes the average energy loss due to the electromagnetic interactions between fast charged particles and the electrons in absorber atoms. For kinetic energies of ions that are small compared with their rest-mass energies, the non-relativistic stopping power formula of Bethe (Bethe, 1930; Bethe and Ashkin, 1953) is given by (in SI units):

$$-\frac{dE}{dx}=\left(\frac{1}{4\pi\varepsilon_{o}}\right)^{2}\frac{4\pi N Z^{2}e^{4}}{m_{o}V^{2}}\ln\left(\frac{2m_{o}V^{2}}{I}\right), \tag{1.d}$$

where Ze is the charge on the incident ion, V is the ion velocity, m_o is the rest mass of the electron, N is the number of electrons per cubic meter of the absorbing material, and I is the mean of all the ionization and excitation potentials of the bound electrons in the absorber. For liquid water, $I = 79.7 \pm 0.5$ eV (Bichsel and Hiraoka, 1992).

According to the formula, the LET is proportional to the Z^2 term, that is, the square of the charge of the particles of the irradiating beam. It also depends on the velocity of the beam. In the formula the velocity term comes twice: once in the denominator and another in the logarithmic numerator. With the increase of V^2 term, the contribution from logarithmic term increases but at the same time, the LET value is lowered due to the V^2 term in the numerator. This is a compromising situation and is the reason behind the appearance of the Bragg peak of radiation in a medium (LaVerne, 2000, 2004).

1.4. LET, track structure, and types of products

As said earlier, the track is composed of individual energy deposition events and the staggering pathways of generated secondary electrons. The radiation track structure is of crucial importance in specifying the precise spatial location and identity of all the radiolytic species and free-radical intermediates generated during radiolysis, and their subsequent interaction with the constituents in the medium they are passing through.

Chemical and biological damage, caused by directly or indirectly ionizing radiations, is attributable to the action of the charged particle tracks in the absorbing medium (Watt and Alkharam, 1994). Track structure also determines the type of products that are more likely to be produced during radiolysis. To explain the relationship between LET, track structure, and types of products, we will divide the discussion for this section into the following two sub-sections:

1. Low-LET radiation
2. High-LET radiation.

1.4.1 Low-LET radiation

Low-LET radiation means lower energy deposition on a unit length basis of the track. If we consider that a certain amount of energy is deposited in a collision event, we can easily figure it out that a low-LET radiation means the lower frequency of energy deposition events. Each energy deposition events ultimately leads to the generation of a spatially expanding region, which is called a "spur" (Magee, 1953). Therefore, a low-energy radiation track should contain a number of individual spurs spaced well away from each other and uninfluenced by the nearby spurs. To visualize the situation, Let us consider the track structure of a low-LET radiation, as shown in Fig. 1.1:

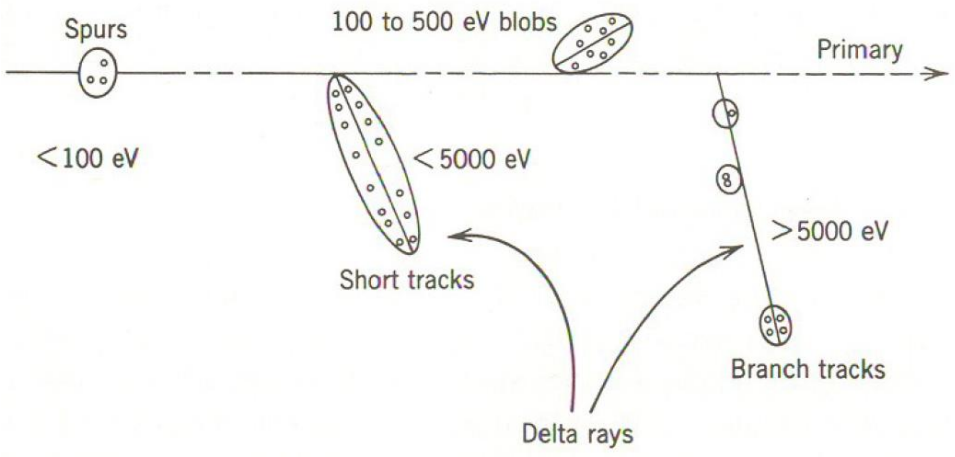

Figure 1.1 – Track structure. Entities are classified as spurs (spherical entities, up to 100 eV), blobs (spherical or ellipsoidal, 100-500 eV) and short tracks (cylindrical, 500 eV- 5 keV) for a primary high-energy electron (not to scale). From Burton (1969).

The track of a low LET radiating beam is divided into individual and non-overlapping entities like spurs, blobs and short tracks (Mozumder and Magee, 1966*a*,*b*). The spur category contains all track entities created by the energy losses between the lowest excitation energy of water and 100 eV; in most cases, there are one to three ion pairs in such isolated spatial areas and about the same number of excited molecules. For blobs, the amount of energy deposition is in the range of 100-500 eV. Secondary electrons of energy greater than 5 keV produce a short track of their own in any direction. Short and branched tracks are, collectively, described as δ-rays (Islam et al., 2018).

1.4.2 High-LET radiation

High-LET radiation means higher energy deposition in a per unit length basis**,** which again means the higher frequency of energy deposition events. As mentioned earlier, each of the individual energy deposition events forms an expanding spur, ultimately. For high-LET radiation, due to the higher frequency or density of the spur, the spurs merge with each other to form a cylindrical track (Fig. 1.2):

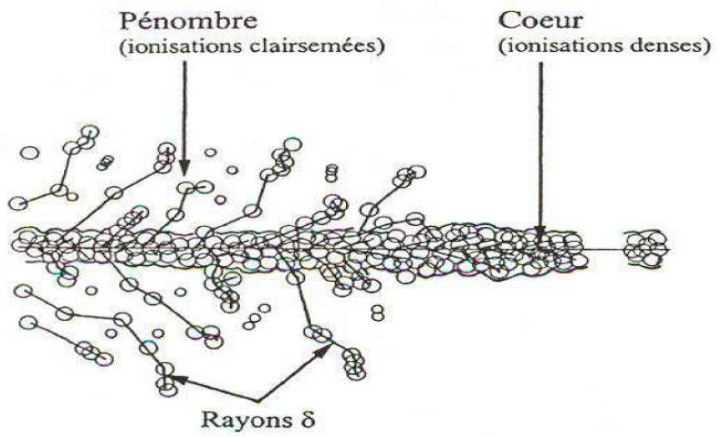

Figure 1.2 – Primary energy-loss events in high-LET radiation tracks (Ferradini, 1979).

This track consists of a cylindrical "core" and a surrounding region traversed by the emergent, comparatively low-LET secondary electrons, called the "penumbra". For this type of track structure, species produced due to radiolysis may be influenced by the species produced by its neighbour. The next very important point to consider in this case is to know about the entities that determines the LET of the radiating beam in a medium. The amount of energy, the velocity of the radiating beam, the mass of the charged particle and the amount of charge of the radiating particle determines the LET.

The track structure or the density of the spur determines the extent and types of products that will be produced from radiolysis (Burns and Sims, 1981). The higher density of spurs that cumulatively produces a cylindrical track structure, allows more free radicals to come in contact with each other and as a result, there is more chance for the reaction between free radicals to produce more molecular products. For radiolysis of water with low-LET radiation, the species from each spur is independent of others and that is why the free radical species do not encounter much of the other free radicals. As a result, it is much probable for the production of free radicals in case of low-LET radiolysis. According to literature, it has been observed that (Anderson and Hart, 1961; Islam et al., 2017; Swiatla-Wojcik and Buxton, 1998) high LET increases the chance of production of H_2 and H_2O_2 whereas at low LET, the yields of $^{\bullet}OH$, $H^{\bullet}$, and e^-_{aq} are favored. The difference in the type of products affects the way the species interacts with the medium.

1.5. The radiolysis process

A radiation is actually a way of energy transfer and practically is equivalent to energy. When a flow of energy passes through a medium, it, in some way, influences the system and the molecules in the system. For this reason, the radiating beam, along its pathway continuously deposit some energy and gradually loses its energy. According to our simulations, the average energy deposition per collision is ~47 eV even for an energetic proton passing through water (Kanike et al., 2015). The complex events that accompany the absorption of high energy photons or the passage of fast charged particles in liquid water can be divided into three consecutive, temporal stages: physical, physicochemical, and chemical stages (Platzman, 1958; Kuppermann, 1959). These stages correspond with the initial dissipation of energy in the system, the establishment of thermal equilibrium, and the establishment of chemical equilibrium, respectively (Hatano et al., 2011). The following section will be a short description of the individual events that occur in these three consecutive temporal stages during radiolysis (Fig. 1.3).

1.5.1 The physical stage

The first stage in the radiation history in the water system is the physical stage. In this stage, energy is transferred to the system. This energy transformation takes place in the time range of 10^{-16} s. The result of this energy transfer is the production, along the path of the radiation, of a large number of ionized and electronically excited water molecules (denoted as $H_2O^{\bullet+}$ and $H_2O^*_{elec}$, respectively) and free electrons:

$$H_2O \rightarrow H_2O^{\bullet+} + e^- \qquad (1.e)$$

$$H_2O \rightarrow H_2O^*_{elec} \qquad (1.f)$$

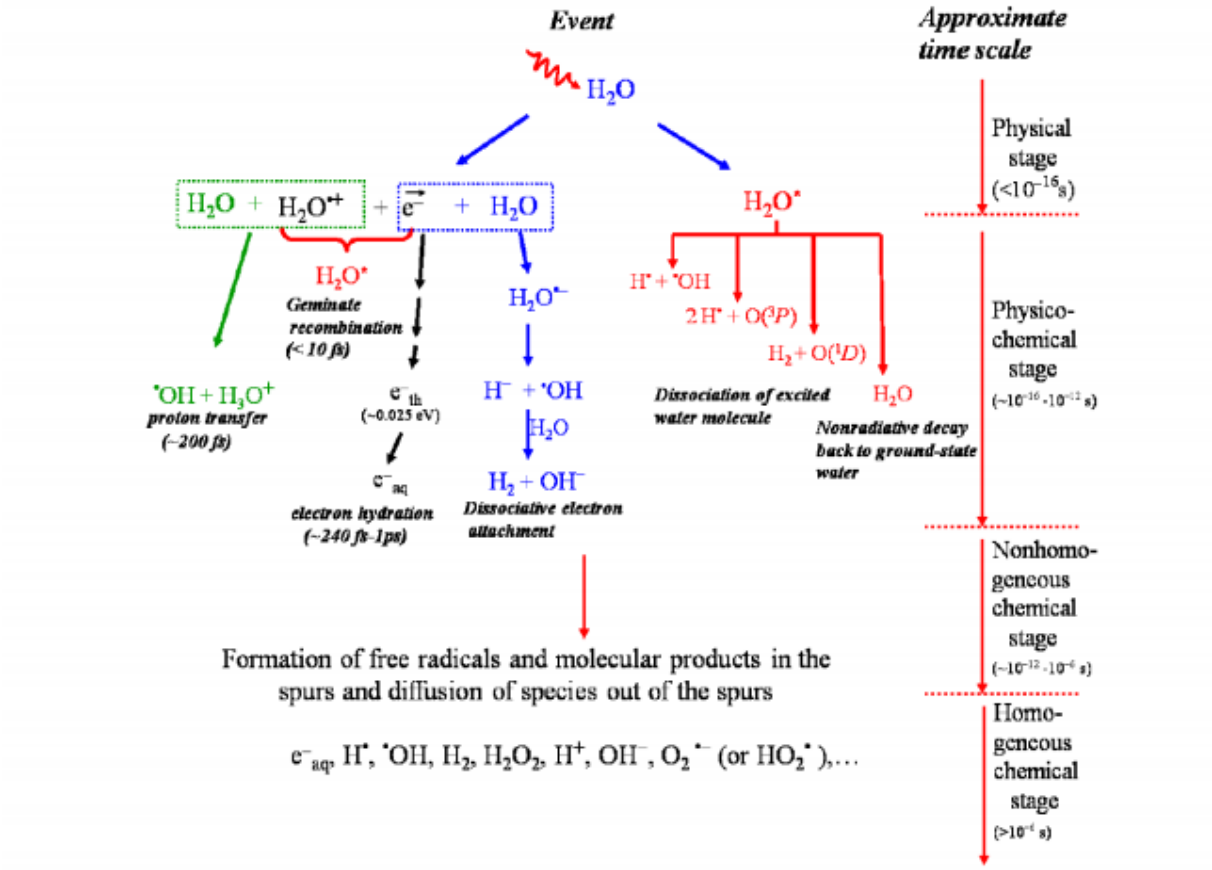

Figure 1.3 – Time scale of events that occur in the low-LET radiolysis of pure, deaerated liquid water (Meesungnoen, 2007). As a guide to the eyes, we used different colors in the figure in order to contrast the individual processes occurring during the radiolysis of water.

It is to be noted that $H_2O^*_{elec}$ here represents many excited states, including the so-called "superexcited" states (Platzman, 1962*a*) and the excitations of collective

electronic oscillations of the "plasmon" type (Heller et al., 1974; Kaplan and Miterev, 1987; Wilson et al., 2001). The ejected electrons, in this case, often have enough energy to ionize or excite other water molecules. Because of ionization, newer secondary electrons are produced into the system, where the electrons are of the wide range of energy, and they can, by themselves, produce their own track of varying lengths.

1.5.2 The physicochemical stage

After the physical stage, we have three main species along the track. These species are unstable and have a very short half-life of around 10^{-14}-10^{-12} s. They follow a number of different pathways including bond rupture, energy transfer, *etc.*, to give different species, which later start to diffuse in space and cumulatively take the form of a spur.

During the physicochemical stage, the following pathways may be followed by the initial species to pacify their instability

1. $$H_2O^{\bullet+} \rightarrow H^+ + {}^{\bullet}OH \qquad (1.g)$$

   The H^+ ions so produced see water molecules in their immediate environment, and become hydrated into a hydrated protonic form. ${}^{\bullet}OH$ produced is mostly unaffected in this stage, which is evident after analyzing its halftime of reaction with different reacting species in pure water.

2. a. The energetic ("dry") secondary electrons lose their kinetic energy by a sequence of interactions with the medium until they attain thermal energies (~0.025 eV at 25 °C) after ~40 ps. In the course of thermalization, the slowing down electrons can be recaptured by water cations, due to the columbic interaction, leading to the vibrationally excited form of water (Meesungnoen et al., 2013; Brocklehurst, 1977):

   $$e^- + H_2O^{\bullet+} \rightarrow H_2O^*_{vib} . \qquad (1.h)$$

2. b. The secondary electrons may have enough energy to cause other ionization events along their tracks, which they do until they have enough energy. Eventually, their

energies fall below the first excitation threshold of water, this is ~7.3 eV. Electrons, in this case, are called "subexcitation electrons" (Goulet et al., 1990, 1996). In this stage, electrons excite the rotational and vibrational modes of water losing further energy to reach thermalization. Once a secondary electron is thermalized, it can be localized or trapped in a pre-existing well of potential energy of appropriate depth. In this case, water dipoles rearrange themselves surrounding the charged electrons. The ultimate stage of electrons is the hydrated form which has its course and interactions into the medium (Ferradini and Jay-Gerin, 1999; Mozumder, 1999).

2. c. In the course of thermalization, the electrons may get attached to water molecules to produce resonant and transient water anion, which may subsequently dissociate. This type of interaction, the so-called "dissociative electron attachment, or DEA" has been observed in amorphous solid water at ~20 K for electron energies between ~5-12 eV. This transient negative ion dissociates to produce the hydride anion (H^-), which later attaches to water and breaks it down to produce molecular hydrogen. This proposed mechanism of H_2 production has received strong support from recent experiments that have shown that the previously accepted nonscavengeable yield of hydrogen is in fact due to the precursors of e^-_{aq} and it can be lowered with appropriate scavengers of dry electrons at high concentrations (Cobut et al., 1996; Sterniczuk and Bartels, 2016).

$$e^- + H_2O \rightarrow H_2O^- \quad (1.i)$$

$$H_2O^- \rightarrow H^- + {}^\bullet OH \quad (1.j)$$

$$H^- + H_2O \rightarrow H_2 + OH^- \quad (1.k)$$

3. The excited water molecules are produced from the physical and physicochemical stage. The fate of these excited water molecules is poorly known in the liquid water phase. However, fortunately, only a small fraction of the total primary radiolysis products comes from the dissociation of excited water molecules in comparison to that of the ionized water molecules. In addition, most of the excited water molecules go back to their ground state by simply emitting the excess energy. In our simulations, the excited water molecules were assumed to follow the

following decay pathways (Cobut et al., 1998; Meesungnoen and Jay-Gerin, 2005; Swiatla-Wojcik and Buxton, 1995).

$$H_2O^* \rightarrow H^\bullet + HO^\bullet \quad (1.l)$$

$$H_2O^* \rightarrow H_2 + O(^1D) \quad (1.m)$$

$$H_2O^* \rightarrow 2H^\bullet + O(^3P) \quad (1.n)$$

$$H_2O^* \rightarrow H_2O + \text{excess energy.} \quad (1.o)$$

Here, *D* and *P* stand for singlet and triplet states of oxygen. Singlet oxygen $O(^1D)$ produced in this reaction reacts very efficiently with water to form hydrogen peroxide and hydroxyl radical (Biedenkapp et al., 1970; Taube, 1957). In contrast, ground-state oxygen atoms $^\bullet O^\bullet(^3P)$ in aqueous solution are rather inert to water but react with most additives (Amichai and Treinin, 1969).

The different radiolytic species, produced during this stage, start to diffuse in space in a three-dimensional geometry and cumulatively form the shape either of an expanding sphere ("spur") for the case of a low-LET radiation or of a cylindrical track for a high-LET radiation.

1.5.3 The chemical stage

The chemical stage is the final stage of the stepwise radiolysis process of water. The species generated from the earlier stages start to diffuse into space during which they encounter other species. During these encounters, they can react with each other and with other species present in the medium, the extent of which is determined by many factors including the reaction rate constants between the corresponding species and the concentration of a particular species into the medium. The chemical stage can be divided into two subgroups named nonhomogeneous and homogeneous chemical stages. The stage of "nonhomogeneous chemistry", which occurs first, is considered to be finished when the expanding spurs or tracks merge and the species becomes homogeneously distributed throughout the medium. This situation occurs in the range of time around a few microseconds. Beyond this time, the reactions, which occur in the bulk solution, can usually be described as a conventional homogeneous chemical

system. This is the second part of the chemical stage, the so-called stage of "homogeneous chemistry". The radical and molecular products which emerge from the spurs/tracks are then available for reactions with homogeneously distributed solutes (if any) present (in low or moderate concentrations) at the time of irradiation. There can be a number of possible reactions into the medium depending on the types of solutes added to the medium and the species generated from earlier stages of radiolysis. For example, for the species H^+ and OH^-, which are produced in the physicochemical and earlier chemical stages, they may take part in any of the following reactions:

Reactions involving H^+

Almost all the H^+ are produced during the physicochemical stage of radiolysis. In the later stages, they are just consumed by different reactions, such as

Reactions	k ($M^{-1}s^{-1}$) (at 25 °C)	
$e^-_{aq} + H^+ \rightarrow H^\bullet$	2.11×10^{10}	(1.p)
$H^+ + O^{\bullet-} \rightarrow {}^\bullet OH$	4.78×10^{10}	(1.q)
$H^+ + O_2^{\bullet-} \rightarrow HO_2^\bullet$	4.78×10^{10}	(1.r)
$H^+ + OH^- \rightarrow H_2O$	11.3×10^{10}	(1.s)
$H^+ + O_3^{\bullet-} \rightarrow {}^\bullet OH + O_2$	9.0×10^{10}	(1.t)
$H^+ + HO_2^- \rightarrow H_2O_2$	5.0×10^{10}	(1.u)

As most of these reactions involve oxygen, and if the program is run in an oxygen-free environment, most of these reactions are contributing negligibly to the overall consumption of H^+ (even though most of them have very high reaction rates). The real competition will be mainly between H^+ and e^-_{aq} and OH^-.

Reactions involving OH^-

In addition to the contribution of OH^- from the physicochemical stage, this species is also produced to some extent in the chemical stage. The following reactions that involve the production and the major routes of consumption of OH^- are:

Reactions	k ($M^{-1}s^{-1}$) (at 25 °C)	
$H^\bullet + e^-_{aq} (+ H_2O) \rightarrow H_2 + OH^-$	2.5×10^{10}	(1.v)
$^\bullet OH + OH^- \rightarrow O^{\bullet-} + H_2O$	1.3×10^{10}	(1.w)
$e^-_{aq} + H_2O \rightarrow H^\bullet + OH^-$	15.8	(1.x)
$H^+ + OH^- \rightarrow H_2O$	11.3×10^{10}	(1.y)

1.6 Interaction of charged particles with water

When a beam of charged particles passes through water, the basic type of interaction between the charged particles and the electrons of the water molecules in the medium is the Coulomb interaction, which ultimately ionizes the water molecules directly. In this case, a direct particle to particle contact is not necessary (Mozumder and Hatano, 2004; Toburen, 2004; Anderson, 1984; IAEA-TECDOC-799, 1995; Spohr, 1990). In case where the energy of the fast charged particle is too high, the direct coulombic interaction may not be so important. In that case, the energy of the beam is enough to cause an electron to be ejected from the atom and this process will be the predominant one. This is one of the reasons why a 300 MeV proton beam is considered to be equivalent to the high-energy gamma radiation.

Because of ionization, water cations and free energetic electrons are produced. These electrons often contain enough energy and are often capable of producing other ionizations of the water molecules in the system along their course. An incident charged ion will produce a number of secondary electrons. In this way, the primary high-energy electron can produce a large number (~ 4×10^4 by a 1 MeV particle) of secondary or higher-order electrons (it is customary to refer to all those electrons that are not primary as "secondary") (ICRU Report 55, 1996). The vast majority of these secondary electrons have low initial kinetic energies with a distribution that lies essentially below 100 eV and a most probable energy below 10 eV (Cobut et al., 1998;

LaVerne and Pimblott, 1995; Mirsaleh Kohan et al., 2013). In most cases, they lose all their excess energy by multiple quasi-elastic (*i.e.*, elastic plus phonon excitations) and inelastic interactions with their environment, including ionization and/or excitations of electronic, intramolecular vibrational or rotational modes of the target molecules and quickly reach thermal equilibrium (*i.e.*, they are "thermalized"). The extent of each of these possible interaction types is dependent on the complex function of the target medium and the energy range of the incident electron. In most of the cases, it is characterized by a probability factor named "cross section", which determines the propensity of a particular interaction type. In a medium, the total interaction cross section is the sum of the cross sections of all the probable interactions. This cross-section can also be correlated with the number of species on a unit volume to calculate the distance between two successive interaction events, which is important in determining the overall track structures:

$$\sigma = \sum_{i} \sigma_i \tag{1.z}$$

$$\lambda = \frac{1}{N\sigma} \tag{1.aa}$$

Here, λ = the distance between two successive interaction events

σ = total cross section

σ_i = cross section for each individual interaction type

N = total number of molecules per unit volume of the medium.

Cross section data are very important to quantify the probability of the various types of interactions that radiation will have with a given medium. That is why the values of cross sections for various types of interactions between radiation and matter have been reported in many works (Emfietzoglou et al., 2001; Hatano et al., 2011; Nikjoo et al., 2012).

In the course of its thermalization, a water molecule may form a transient water anion ($H_2O^{\bullet -}$) by temporarily capturing the ejected electron resonantly. This water anion will later undergo dissociation to produce a hydride anion H^- (Fedor et al., 2006; Ram et al., 2009). These hydride anions are responsible for the production of non-

scavengeable molecular hydrogen at early times by reaction with a neighboring water molecule, which is justified by a number of experiments (Platzman, 1962*b*; Goulet and Jay-Gerin, 1989; Meesungnoen et al., 2015; Sterniczuk and Bartels, 2016). The thermalized electrons later lose further energy to get trapped in a well of water dipoles. These trapped or "wet" electrons subsequently transform into hydrated or aqueous electrons (Marsalek et al., 2012; Mozumder, 1999; Hart and Anbar, 1970; Walker, 1967; Herbert and Coons, 2017).

In the course of its passage through a water medium, a radiation beam leaves behind a series of events, a number of products (either free radicals or molecular products), which cumulatively takes the form of a track or pathway. The diffusion of secondary electrons, in the earliest times, form the sub-routes of the tracks. At a longer time, this track expands in a three-dimensional way due to the diffusion of species produced in the track.

1.7 Interaction of photons with water

γ-rays are electromagnetic radiations emitted either from a nucleus or an annihilation reaction between matter and antimatter. X-rays are electromagnetic radiations emitted by charged particles (usually electrons) in changing atomic levels or in slowing down in a Coulomb force field. X- and γ-rays have identical properties, only differing in origin. While passing through a medium, high-energy photons may take part in any of the following three different types of interactions, namely, photo-electric, Compton scattering, and pair production (Anderson, 1984; Spinks and Woods, 1990).

For photoelectric type interactions, energetic γ-rays transfer their energy to the materials and eject an electron from the matter leaving behind a hole in the molecular orbital of the matter. Later this hole is filled by an electron from other orbitals leaving behind another hole and release of some energy. This phenomenon gives rise to the generation of a cascade of characteristic X-rays in the system. This photoelectric type interaction is dominant for low-energy γ-rays.

In the case of Compton scattering, some part of the energy of γ-ray is transferred to the electron of the matter resulting in the transformation of electrons to a state of

higher energy. Later the electrons come back to the original state emitting the energy they absorbed. Because of this interaction, the generated photons (from the irradiating γ-rays, and the photons generated from the matter) travel in different directions other than the original photon path.

The process of pair production is possible for photons with an energy greater than 1.02 MeV. Pair production converts the photon into a positron-electron pair in the field of the atomic nucleus. In a practical situation, pair production is not a predominant one unless the energy of γ-rays is more than several MeV.

Concretely, in any manner whatsoever, a γ-ray beam has an impact on the water, the final result of the impact being the production of an excited or ionized water molecule.

1.8 Interaction of neutrons with water

The interaction of a neutron with matter is relatively different from those of other radiations like a proton or alpha. Because neutrons carry no charge, their interaction with electrons is exceedingly small, and primary ionization by neutrons is a completely negligible effect. The interaction of neutrons with matter is confined to nuclear effects. Depending on the energy of the incident neutron particle, there are different types of interactions like scattering, absorptions, nuclear reactions and capture processes (Butarbutar et al., 2014*a*; Mozumder and Hatano, 2004; Rinard, 1991; Tippayamontri et al., 2009).

Table 1.1 – Neutron energy ranges (Anderson, 1984).

Category of neutrons	Corresponding energy
High-energy neutrons	$E > 10$ MeV
Fast neutrons	500 keV $< E < 10$ MeV
Intermediate neutrons	1 keV $< E < 500$ keV
Slow neutrons	0.025 eV $< E < 1$ keV
Thermal neutrons	$E \approx 0.025$ eV
Cold neutrons	$E < 0.025$ eV, often as low as 0.001 eV

The classification of the types of interactions, from scattering to capture, is based on the relative energy of the neutrons. Neutrons are also classified based on the energy they possess (Table 1.1). The different types of interactions that neutrons can make with matter are summarized in Fig. 1.4.

Interaction of neutrons with a medium may be of one of the two major types: scattering or absorption. When a neutron is scattered by a nucleus, its speed and direction change but the nucleus is left with the same number of protons and neutrons it had before the interaction. Scattering processes can be subdivided into elastic and inelastic scattering processes. In inelastic scattering processes, part of the energy of the incident neutron is taken up by the nucleus and thus transfers the nucleus to an excited state and the total kinetic energy before and after the collision events does not remain conserved.

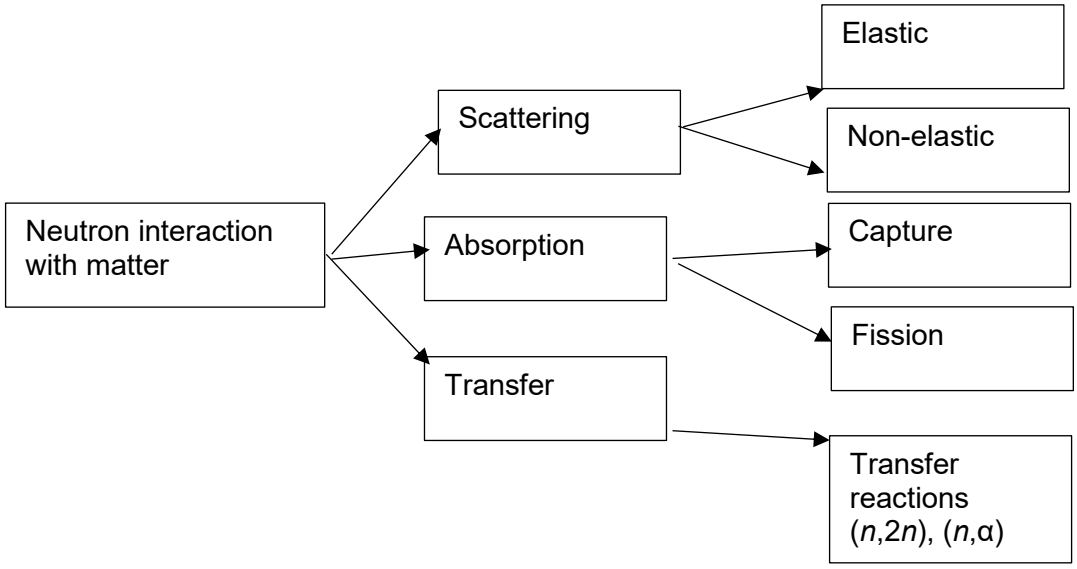

Figure 1.4 – Classification of the interactions of a neutron with matter.

The nucleus-neutron system loses some energy, which does not contribute to their overall momentum and kinetic energy. These excited nuclei eventually lead to the emission of gamma radiation. The neutron with remaining energy travels and makes other interactions. In elastic scattering, the energy of the neutron is shared between the neutron and recoiling nucleus and thus ultimately the total momentum before and after

collision remains constant. For the cases where the excited states of the nucleus are so high in energy, elastic scattering becomes the only mode of interaction (between elastic and inelastic). For the hydrogen nucleus, it does not have any excited states and for this reason, no inelastic interaction actually takes place (Tippyamontri et al., 2009). The neutron may also be captured by a nucleus, which ultimately leads the nucleus to an unstable stage. The nucleus may rearrange its internal structure and release one or more γ-rays. Charged particles may also be emitted the more common ones being protons, deuterons, and α-particles (Rinard, 1991). These charged particles often have their own course in the medium and may produce radiolysis products. For example, this capturing of the neutron by the atomic nucleus is responsible for the boron neutron capture reaction in a nuclear power plant giving two He^{2+} and Li^{3+} recoiling ions, which is the basis of the "Boron Neutron Capture Therapy" or BNCT (Islam et al., 2018).

The type of interaction a neutron will make with matter is dependent on the neutron energy and the cross section of matter for the neutron. The standard unit of measurement of the microscopic cross section is the *barn* (1 barn = 10^{-24} cm^2).

For the high-energy neutrons, the most important type of interaction is inelastic collisions, especially with heavy nuclei. For a low-energy neutron beam (up to intermediate energy), the most important types of reactions of neutrons are elastic scattering and a series of nuclear reactions. In this case, most slowing down is accomplished through a process of many successive elastic collisions with nuclei. Because of the conservation of momentum, a neutron of energy E_o, making an elastic collision with a heavy nucleus, bounces off with most of its original energy, giving up a wide range of energy (up to a maximum) to the recoil. At each scattering site, the neutron loses energy and is thereby moderated or slowed to lower energy. On the other hand, if the energy of the neutron beam is too high, inelastic scattering may also take place. In that case, the recoil nuclei by themselves may even elevate to an excited state. Later, it emits γ-rays into the system. The extent of energy that can be transferred to the recoil nuclei can be calculated. For incoming neutrons with nonrelativistic kinetic energy E_n (<< 939 MeV), conservation of momentum and energy in the centre-of-mass

(CM) coordinate system gives the following relation for the energy of the recoil nucleus:

$$E_r = \frac{2A}{(1+A)^2}(1-\cos\varphi_{\mathrm{CM}})E_n, \tag{1.bb}$$

where A is the mass number of the nucleus, E_r is the energy of the recoil nucleus, E_n is the energy of the incoming neutron beam, and φ_{CM} is the scattering angle of the neutron in the centre-of-mass coordinate system. This equation can be used to get the energy of recoil nuclei for a set of the initial energy of neutrons and a corresponding scattering angle. This type of relationship may also be achieved for a corresponding scattering angle of recoil nucleus (where the target nucleus is set to be at rest initially) as follows:

$$E_r = \frac{4A}{(1+A)^2}(\cos\theta)^2 E_n, \tag{1.cc}$$

where θ is the scattering angle of the recoil nucleus. According to this equation, the energy of the recoil nucleus may vary from a very high to a very low value. The maximum energy of the recoil nucleus is given by

$$(E_r)_{\max} = \frac{4A}{(1+A)^2}E_n \ . \tag{1.dd}$$

A chart is given below (Table 1.2), which shows the maximum energy of different recoil nucleus generated from neutron interaction.

Table 1.2 – Relative amount of energy taken away by different recoil nuclei.

Recoil nucleus	Atomic weight	Maximum energy as a fraction of neutron energy
${}_{1}^{1}\mathrm{H}$	1	1
${}_{1}^{2}\mathrm{H}$	2	0.89
${}_{2}^{3}\mathrm{He}$	3	0.75
${}_{2}^{4}\mathrm{He}$	4	0.640
${}_{6}^{12}\mathrm{C}$	12	0.284
${}_{8}^{16}\mathrm{O}$	16	0.221

For our case of interest, we mainly work with the water system, which consists of two hydrogen atoms and an oxygen atom per molecule. Moreover, from Table 1.2, it is clear that the hydrogen atom will take up the major part of the energy. It is estimated that these hydrogens take about 85% of the total energy of the neutron, which ultimately leads to the production of recoil protons.

The following formula is used to calculate the energy deposition in each successive interaction by the irradiating neutron beam. The deposited energy is then taken to be the energy of recoil protons.

$$\ln\left(\frac{E_{\mathrm{o}}}{E_{\mathrm{n}}}\right) = \mathrm{n}\left[1 + \frac{(A-1)^2}{2A}\ln\left(\frac{A-1}{A+1}\right)\right] \qquad \text{(1.ee)}$$

where E_{n} is the energy after n-th individual elastic scattering collision, A is the atomic number of the recoil ion being considered. For protons, A is 1. During the calculation of the recoil proton energy, the energy left after the first recoil released is calculated and is then deducted from the original neutron energy to get the energy of the recoil proton. The remaining neutron energy is used later to calculate the energy of another recoil proton. In this present study, the number of recoil protons to be considered in the simulations depends on the minimum energy limitation of our program (see *infra*).

The final neutron yields (for given radiolytic species X) are then calculated by summing the G values for each considered recoil proton weighted by its fraction of the total neutron energy absorbed (Tippayamontri et al., 2009; Butarbutar et al., 2014*a*,*b*):

$$G(\mathrm{X}) = \frac{\sum_{\mathrm{i}} \left(G(\mathrm{X})_{p_\mathrm{i}} E_{p_\mathrm{i}} \right)}{E_\mathrm{T}}, \tag{1.ff}$$

where $G(\mathrm{X})_{p_\mathrm{i}}$ is the free radical or molecular yield associated with the recoil proton p_i and

$$E_\mathrm{T} = \sum_{\mathrm{i}} E_{p_\mathrm{i}} \tag{1.gg}$$

is the sum of all considered recoil proton energies.

1.9 Importance of water radiolysis in the biological system

Nature is full of different types of radiations generated from different sources including the radioactive nucleus and other extra-terrestrial sources. A human body contains almost 80% of water by its weight and this water is continuously subjected to radiolysis from different types of radiation in many ways (both intentional and non-intentional). This radiolysis phenomenon even would not be of so much importance if the dose rate and track chemistry involved in the radiolysis were not associated with this. In general, water radiolysis produces different reactive species including free radicals, molecular products and ions. Our body also has its metabolic system that produces different active species as the metabolites. It is estimated that our body produces as many free radicals in a day as a radiation dose of 35 Gy would produce from water radiolysis. The question can be how we are still alive! The answer is in the radiation dose rate and the concentration of radical species in contact with the biomolecules. Radiation-induced free radicals are produced in close proximity of important biomolecules in an appreciably high concentration. This concentrated region is efficient enough to initiate damage to the biomolecules. The impact of radiation dose rate can be understood from the relative amount of damage to the body from eating a banana every day for years and eating a very small piece of Cs-137 only once. Eating banana deposits a very small amount of potassium in the body, which is radioactive.

The impact of radiation on biological system starts with the direct effect, which takes place in the timescale of femtoseconds. In direct effects, the radiating beam directly interacts with the biologically important molecules and destroys their molecular structure (Sharma et al., 2011; Symons, 1994). These destroyed molecular structures, later, may produce carcinogenic effects. The extent of damage from direct effects is dependent on the LET of the irradiating beam (for high-LET radiation as with α-particles, the extent of the direct effect is significant), dose rate, and the concentration of the species. Direct radiation damage is initiated in the time range of ~10^{-14}–10^{-12} s with the breaking of different types of chemical bonds in the biological system including S–H, O–H, N–H, and C–H bonds of biological molecules.

The indirect effect is generated from the interaction of the biological molecules with the radiolytically generated active species like free radicals, ions and molecular products, which are oxidizing in nature, generally. The most important type of free radical reaction is the transformation of the free radical to other species. In fact, free radicals do this during interactions with biological molecules. Because of this transformation, the biological molecules become free radicals themselves. These newly produced species then starts reacting in a number of ways including electron transfer, dissociation of molecules, formation of adducts of two free radicals, *etc*. Many of these products are not compatible with the usual biological system and generate different biological consequences.

Both $^{\bullet}OH$ and e_{aq}^- react with the nucleobases at diffusion-controlled rates, adding to unsaturated bonds and abstracting $^{\bullet}H$ from methyl and deoxyribose substituents (von Sonntag, 2006). For purine nucleobases, $^{\bullet}OH$ adds at C_4, C_5, and C_8, generating reactive adduct radicals that lead to a variety of products, for example giving 8-hydroxypurines, which are considered as a well-known hallmark for oxidative DNA damage. Pyrimidine olefins are also susceptible to $^{\bullet}OH$ addition, particularly at C_5 and C_6, generating pyrimidine glycols in the presence of O_2 (Reisz et al., 2014). The capacities of hydrated (e_{aq}^-) and prehydrated electrons to facilitate DNA strand breaks have drawn attention only recently but appear to play an important role in the cumulative effects of ionizing radiation on DNA (Simons, 2006; Wang et al., 2009). In

fact, it has been shown by both solid and gas phase experiments that single DNA bases possess low-energy resonances at subexcitation energies and that they are subjected to subsequent decomposition (DEA) (Boulanouar et al., 2013; Denifl et al., 2004; Pan et al., 2003). Another structural constituent of DNA, deoxyribose sugar, is also found to be sensitive to the attack of low-energy electrons, which can lead to a sugar-phosphodiester strand break. A study on pentose and hexose has also proved the presence of this type of reactions of sugar with very low-energy electrons and it is supposed to be true for sugars generally (Sommerfeld, 2007).

Another biomolecule target of radiation-generated oxidative species is the lipid layer within cell membranes. Lipid layer in the cell membrane can directly be impacted by radiation. In addition to this direct impact it has been observed that the irradiation targeting cell membrane may induce cellular apoptosis via induced ceramide level, which was the same with cells without a nucleus (Haimovitz-Friedman et al., 1994). This, actually, reveals a way of cellular damage without the participation of nucleic materials. Polyunsaturated fatty acids react with different radicals, especially $^{\bullet}OH$, to form radicals of fatty acids. This then transfers its radical to the generation of different types of products (Fritz and Petersen, 2011). *In vivo* evidence for increased levels of reactive aldehyde, malondialdehyde (MDA), in response to ionizing radiations has been shown in the kidney, lung, and liver of rats exposed to 8 Gy of total body irradiation (Girotti, 1998). High level of LOOH or hydroperoxide may ultimately lead to cell membrane lysis and apoptosis (Şener et al., 2006).

Proteins are also one of the most abundant groups of ingredients in the cell and are a subject to the attack of radiolytically generated species. *In vivo* evidence for the oxidative modification of proteins in response to ionizing radiation has been observed in the mouse brain and rat liver as judged by the increase in protein carbonylation (El-Missiry et al., 2007). Radicals, including $^{\bullet}OH$ and others, are believed to preferentially react with the protein amide backbone over the amino-acid side chains, readily abstracting hydrogen atoms and forming α-carbon-centred radicals. This ultimately leads to the breaking down of protein backbone along with the other modification of all the twenty amino acids with very high corresponding rate constants at physiological pH

(Blum and Fridovich, 1985; Davies, 2005). Aromatic amino acids are significantly high in reactivity towards •OH radicals, which leads to the production of phenoxyl radicals. In the absence of reductants, these radicals form dimers and other inter and intra conjugated compounds. This type of protein oxidation has been implicated in the progression of many different diseases, including diabetes, inflammation, sepsis, Alzheimer's disease, multiple sclerosis, Parkinson's disease, and many cancers (Dexter and Jenner, 2013; Hensley et al., 1994; Yang et al., 2011).

1.10 Importance of water radiolysis in the nuclear industry

The environment inside the reactor core of a nuclear power plant is robust in the sense that it is exposed to extreme conditions of very high temperatures and pressures. In addition to that, the constant flow of fluid into the system makes the materials of construction very much vulnerable to the attack of various reactive species because continuous flow washes away the adjacent protective oxide film from the material surface. Moreover, radiation itself may be responsible for the dislocations of atoms from the well-organized crystallized form of materials, which creates microgrooves on the surface of materials making the materials prone to attack (Cattant et al., 2008; Lister and Cook, 2014). Under these conditions, a slight increase in the total number of reactive species into the system may prove dangerous for the overall working age of the materials. Radiolysis of water continuously does the job. A mixed field of different types of radiations including γ-rays and other low-energy charged particles always exists into the core (Jarczyk et al., 1961). That is the reason why the field of radiation chemistry for the core of the nuclear reactor is still open and a major part of the design consideration of a nuclear power plant. Numerous studies are available in the literature just to see the propensity or pathways of corrosions into the materials of the system (Cattant et al., 2008; Neeb, 1997; Uchida, 2008; IAEA, 2011). It is believed that there is a correlation between the radiolytically generated species and the corrosion or the mechanism of corrosion. This is important because a proper knowledge and understanding of the mechanism of corrosion helps in finding the appropriate environment of operation of a nuclear power plant. In such a context, the control of water chemistry is a major requirement for plant operators. This control has been

carefully optimized over many decades of operating experience to minimize in-core materials degradation processes and of course to optimize plant performance. It is continually updated as operating experience evolves. Excellent reviews have been published on the basics of water chemistry practices in current generation water-cooled reactors (Cohen, 1980; Kritsky, 1999; Uchida and Katsumura, 2013).

In connection with controlling the chemistry of the coolants of water-cooled power reactors, let us recall here briefly some essential aspects. Perhaps most importantly, mitigation and suppression of the production of oxidative species are currently achieved by adding an extra amount of molecular hydrogen to the system (McCracken et al., 1998; Takiguchi et al., 2004). Interestingly, dissolved ammonia (NH_3) was also used for reactor control. This technique gave good results, which is of no surprise since the reaction of NH_3 with the radiolysis products of water ($^{\bullet}OH$ and $H^{\bullet}$) leads to the formation of H_2.

It is customary to maintain a definite pH ($pH_{300\,^{\circ}C}$ = 7.2-7.3) in the reactor water but the problem is that it changes continuously. This change in pH is also an indication of the impact of radiolytically generated species into the reactor core. For suppressing the fluctuations in pH in the system nuclear reactors use an alkalizing agent, most often lithium hydroxide (LiOH) or potassium hydroxide, as a pH stabilizer (Cohen, 1980; Aaltonen and Hanninen, 1997).

Boron is another important element in a nuclear reactor and it is used as the moderator. This boron may capture a neutron in the reactor core and produce a so-called "boron-neutron capture reaction". This reaction later produces two recoil ions, namely, a lithium ion and a α-particle. In some previous papers from our laboratory (Islam et al., 2017, 2018), it was established that the radiolysis of water by these high-LET ions produces large amounts of H_3O^+ at early times, which renders the "native" track regions temporarily very acidic. Although these "acid spikes' have never been invoked in water, they could have important consequences as they could promote a corrosive environment that would lead to a progressive degradation of reactor components (see *infra*).

In some reactors, hydrazine has also been used for H_2 generation to suppress water radiolysis. Hydrazine is an inorganic chemical agent (N_2H_4), which preferentially takes up an electron in spontaneous redox reactions in the material surface of the reactor core, thus controlling the overall ECP on the surface (Nakano et al., 2014; Uchida, 2008). ECP stands here for the "electrochemical corrosion potential" and it is a measure of the propensity of electrochemical reaction on the surface of a material. This option is nevertheless disadvantaged by environmental restrictions placed on hydrazine use in many jurisdictions.

The conductance of water is defined as the capacity of water to conduct electric current through it. In normal conditions, water is very slightly dissociated to produce a slight amount of H^+ and OH^-. Therefore, the conductivity is low. However, when there is an increase in the number of ions or radicals or active species in the water, there is a rapid increase in its conductivity. Nowadays the conductivity of water is considered to be a good measure of the overall water quality and a sudden change in conductivity is a sign that corrective action must be taken immediately (Lister and Uchida, 2015).

1.11 Generation-IV (Gen-IV) supercritical water-cooled nuclear reactor project

Nuclear energy is certainly one of the most important solutions to the probable energy crisis in the future. In a nuclear power plant, the energy from a nuclear reaction is taken up by a medium and this energy is later used for production of electricity and other forms of suitable energy sources like molecular hydrogen production, coal liquefaction, *etc*. The venture of this energy production from a nuclear reaction started in 1951 with an experimental breeder reactor (Goldberg and Rosner, 2011). – (Note that a breeder reactor is one that produces more fissionable materials than it consumes. When a uranium-235 nucleus, which is the usual type of fuel, is split in a nuclear reactor, it produces neutrons. These neutrons can be absorbed by another nucleus of uranium causing subsequent splitting of that nucleus and this cycle continues until fissionable materials are consumed. Generally, the neutrons generated from nuclear reactors contain enough energy and they move fast, as a result of which, they cannot be absorbed efficiently by the fissile materials for sustaining nuclear reactions. So, reactor cores have a technology to slow down the energetic neutrons to let them take part in

nuclear reactions. In a breeder reactor, these speedy neutrons from nuclear reactions are directly made to be absorbed by some isotopes to convert them to other fissile materials. In this way, the breeder reactors produce a new type of excess amount of fissile materials). – This is an example of the first generation of nuclear reactors (in the mid-1950s and early 1960s) and, later, two other generations (II and III) of reactors for commercial electricity production were used. The gradual upgrading of generation is based on the improvement in fuel utilization efficiency, safety in functioning, *etc.* Very recently, a new generation of innovative reactors has been identified by the Generation IV (Gen IV) International Forum (GIF, 2002, 2014). The aim of this new generation is mainly to improve the operational efficiency, economics and sustainability of a reactor and to increase safety for the environment. GIF is an international collaborative platform of cumulative development of this next generation of power plants and it functions to coordinate ongoing research projects. GIF selected six possible Gen IV designs/concepts for further research and development (Locatelli et al., 2013), including the *gas-cooled fast reactor* (GFR), *lead-cooled fast reactor* (LFR), *molten salt reactor* (MSR), *sodium-cooled fast reactor* (SFR), *very-high-temperature reactor* (VHTR), and *supercritical-water-cooled reactor* (SCWR). Depending on their respective degree of technical maturity, the first Generation IV systems are expected to be deployed commercially around 2030-2040. Below, we will describe in some detail one of these proposed nuclear technologies, which is of interest to us in this study, namely, the Gen IV SCWR (Guzonas et al., 2018; Pioro, 2011; Cai et al., 2014; Yetisir et al., 2016). This design is considered as one of the most promising Gen IV reactors, due to its advantages of plant simplification and high thermal efficiency.

The use of supercritical water as a coolant in nuclear reactors is the logical evolution of the present water-cooled Gen II and Gen III reactors. As a most promising advanced nuclear reactor system, the economic advantages of the Gen IV SCWR are considerable due to plant simplification, increased thermal power-to-electricity conversion efficiency (greater than 45% vs. 33-35% for conventional nuclear power plants), and enhanced passive safety characteristics (Guzonas et al., 2018).

Gen IV SCWRs under consideration would operate with core inlet and outlet temperatures of ~350 °C and 625 °C, respectively, at a pressure of 25 MPa. A

quantitative understanding of the radiation chemistry of SCW under these conditions is thus required in the design and operation of these reactors. However, dealing with supercritical water is not only about dealing with water simply at very high temperatures and pressures. It will also require some additional considerations to take into account the various peculiar physicochemical of SCW, which we will describe briefly in the next section.

1.12 What are the peculiarities of supercritical water?

The relationship between temperature, pressure and phase of a substance is represented in a phase diagram. The temperature-pressure phase diagram for water is shown in Fig. 1.5. According to this diagram, the saturation curves represent the equilibrium between two phases of water. For example, the saturated vapor pressure curve in the diagram represents the equilibrium between water vapor and liquid water. As the temperature increases, the vapor pressure of water also increases and to keep the vapor into the liquid phase, a higher amount of pressure is needed. This type of relationship only exists up to a certain maximum point of temperature and pressure, called the critical point. For light water (H_2O), this point occurs at 373.95 °C and 22.06 MPa, respectively. Water beyond the critical point is called the “supercritical water” or SCW in its usual abbreviated form. In that case, the vapor and liquid phases become indistinguishable from each other, that is, liquid water is hot enough and gaseous water is under sufficient pressure that their densities are identical.

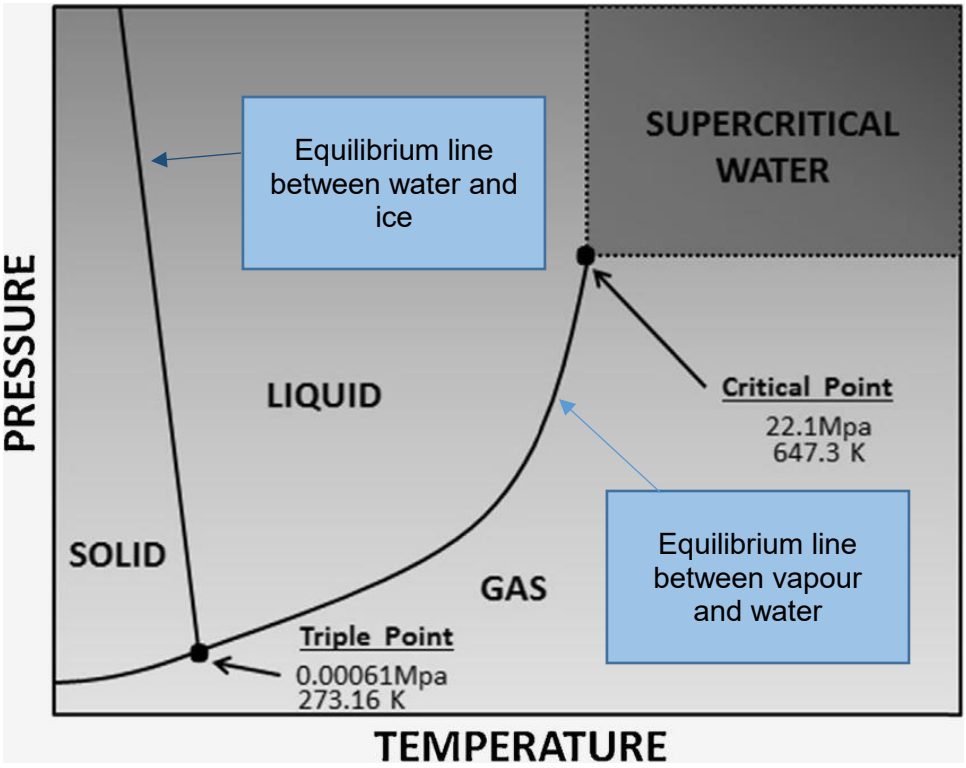

Figure 1.5 – Phase diagram as a function of the pressure and temperature of water (adapted from Canıaz and Erkey, 2014).

The critical point of water brings dramatic changes in a number of its thermo-physical properties. For instance, liquid water under normal conditions is nearly incompressible, has a low thermal expansion coefficient, has a high dielectric constant, and is an excellent solvent for electrolytes. Near the critical point, all these properties change into the exact opposite: water becomes compressible, expandable, a poor dielectric, a bad solvent for electrolytes, and prefers to mix with nonpolar gases and organic molecules (Akiya and Savage, 2002; Anisimov et al., 2004; Galkin and Lunin, 2005).

The viscosity of a medium is an important property that determines the ease of flow of a certain solute through it. For example, if we consider the case of a reaction between two species, the reaction can be either diffusion controlled (or diffusion limited) or activation controlled. For a diffusion-controlled reaction, the diffusion of the species towards one another is the rate-determining step of the reaction. In other words, as quickly as the reactants encounter each other, they react. In that case, the rate of the

reaction between the two species is dependent on the viscosity of the solution and the extent of mass transfer of the reacting species. In contrast, in an activation-controlled reaction, the rate is controlled by the ability of the reactants that have met each other to acquire enough energy from the surrounding solvent molecules to surmount the activation barrier and react.

Generally, an increase in temperature corresponds to a decrease in the solvent viscosity, which is due to a decrease in the cohesive intermolecular forces. A decrease in viscosity therefore increases the diffusion (or "mobility") of dissolved species. The diffusion coefficient (D) of spherical particles of radius R in a fluid of viscosity η at absolute temperature T is given by the Stokes-Einstein equation (Einstein, 1956):

$$D = \frac{k_B T}{6 \pi \eta R}, \tag{1.hh}$$

Where, k_B is Boltzmann's constant. This equation holds its validity up to the critical point with $D\eta/T$ = Constant, which may be used to predict solute diffusivity as a function of temperature.

Due to the polarity of its molecules, water has the ability of forming hydrogen bonds with each other and with other (polar) molecules. Under normal conditions, all water molecules are interconnected by an infinite, three-dimensional (tetrahedral) percolating network of hydrogen bonds. With increase in temperature, the hydrogen bonding becomes weaker or breaks. Although it has long been a debate about the extent of hydrogen bonding at elevated temperatures, several types of research and computer-aided simulation already established that there is a nonzero extent of hydrogen bonding at high temperatures even at supercritical temperatures. Under these conditions, water exists as small separate clusters, within which the molecules remain hydrogen bonded. With the decrease of the extent of hydrogen bonding, the size of these clusters also decreases. For example, at 500 °C and ~0.1 g/cm^3 density there are 10-14% of the hydrogen bonds that are retained relative to ambient temperatures. At 400 °C and 0.5 g/cm^3, this proportion increases to 30-45% (Bursulaya and Kim, 1999; Hoffmann and Conradi, 1997). The breaking of the system of hydrogen bonds also affects the dynamics of water molecules by reducing the barrier for rotational and translational

motions. The water molecules not involved in the hydrogen bond network thus become more mobile, leading to an increase in the self-diffusion coefficient of water (Lamb et al., 1981). The changes in hydrogen bonding is also associated with a corresponding change in the dielectric constant of water. For example, the dielectric constant of liquid water at 300 °C and 0.75 g/cm^3 density (29.55 MPa) is 21.9 and that of SCW at 500 °C and 0.3 g/cm^3 density (55.1 MPa) is 4.2 (Uematsu and Frank, 1980; NIST Chemistry WebBook, 2018).

The (static) dielectric constant is a measure of the ability of a solvent to be polarized by an electric field. It determines the extent to which a material will concentrate electric flux. A medium with a high dielectric constant will have a tendency to increase the flux density if all other parameters remain constant. This becomes clear from Coulomb's law, which describes the (attractive) force between two charged particles of opposite sign:

$$F = \frac{1}{4\pi\varepsilon_\circ\varepsilon_r}\frac{q_1 q_2}{r^2}\,. \qquad (1.ii)$$

Here, F is the force between the particles 1 and 2, q_1 and q_2 being their charges. The separation between the particles is r, ε_o is the permittivity of free space, and ε_r is the dielectric constant (also known as "relative permittivity"). According to this equation, with an increase in the dielectric constant, the attractive force between two oppositely charged particles is decreased, which will allow the two ions in the medium to be more separated and less likely to combine. In this context, we see that the dielectric constant is especially important in studying kinetics of reactions.

Ordinary liquid water has a higher dielectric constant than most liquids because of its polarity and the association of molecules due to hydrogen bonds. At ambient temperature, ε_r is ~78. However, ε_r declines rapidly at higher temperatures as the density (and correspondingly the extent of hydrogen bonding) diminishes. At 400 °C, *i.e.*, in the supercritical regime, water has a dielectric constant varying from 3 to 12.6 in the density range from 0.15 and 0.6 g/cm^3 (Karpov and Medvedev, 2016; Pitzer, 1983). The lower dielectric constant of SCW suggests that the solvent has a lower ability to screen charges. This means that the charges in a solution interact with the electric

dipoles of water less than with each other, increasing the overall interaction. In comparison to ordinary water, the interaction between anions and cations is much greater.

The ionic product, or dissociation constant (K_w) is another important property of water that varies considerably with changes in density (pressure) and temperature. Briefly, K_w quantifies the remarkable ability of water to self-dissociate into measurable ionic H^+, OH^- concentrations (pH = 7 under ambient conditions) (Perlt et al., 2017). The low dielectric constant of water in the supercritical regime significantly changes K_w and pH (Fig. 1.6) and SCW is only slightly dissociated compared to sub-critical water (Marshall and Franck, 1981; Verma 2003; Bandura and Lvov, 2006). The value of K_w for liquid water near the critical point is about three orders of magnitude higher than that at room temperature. Under these conditions, ionic mechanisms are favored and sub-critical water is an effective medium for acid- and base-catalyzed chemical reactions.

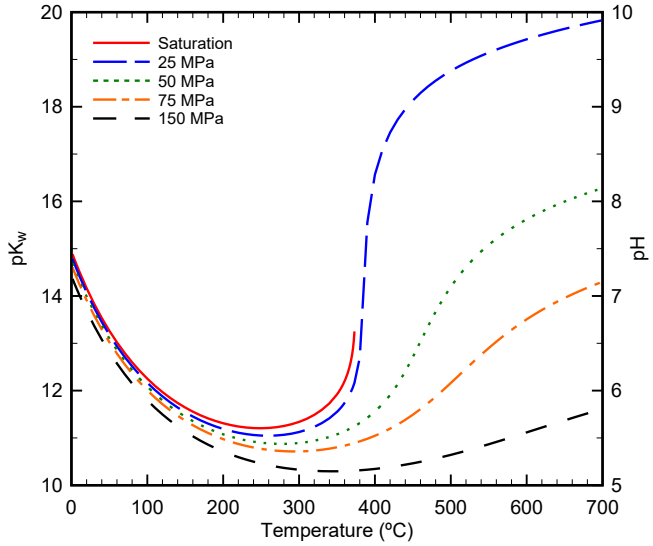

Figure 1.6 – Plot of $pK_w = -\log_{10}(K_w)$ and pH of neutral water against temperature. From Guzonas and Cook (2012), Courtesy Dr. D. Guzonas.

However, for SCW at gas-like densities (0.1 g/cm^3 or less) K_w falls drastically (tens of orders of magnitude lower than for ambient liquid water). Accordingly, free-radical chemistry is favored at these high-temperature, low-density conditions. The

competition between homolytic (free radical) and heterolytic (ionic) mechanisms changes in supercritical water as K_w changes was explored by Antal et al. (1987) and by Westacott et al. (2001). These authors proposed that when $K_w > 10^{-14}$ ionic mechanisms are favored, whereas when $K_w << 10^{-14}$ free radical chemistry dominates.

In addition to the properties described above, many other thermo-physical properties of SCW, including density, specific heat, thermal conductivity, *etc.*, also undergo drastic changes through the critical point (Fig. 1.7). For example, considering the change in water density (ρ) as a function of temperature, the density of water at 350 °C, 26 MPa is 0.630 g/cm^3. However, as soon as the critical point is exceeded, the density fell abruptly. At 400 °C, 26 MPa, it is 0.189 g/cm^3.

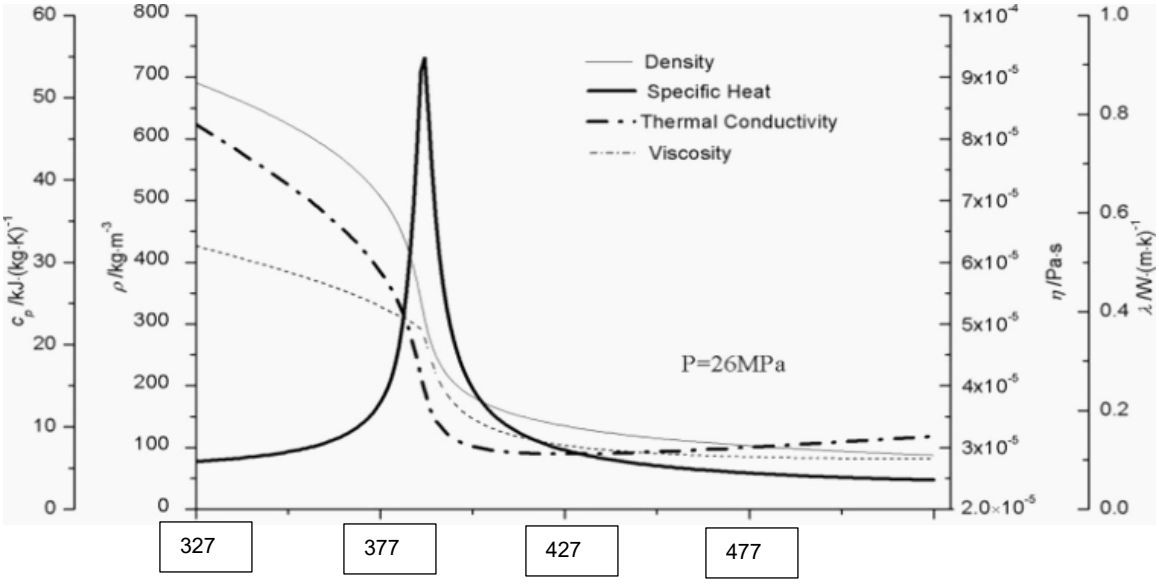

Figure 1.7 – Variation of the thermo-physical properties of water with the temperature at pressure of 26 MPa (adapted from Lei et al., 2013).

Supercritical water has other properties that are difficult to model. This is the case for the arrangement of water molecules, which is not homogeneous at a particular bulk density. Figure 1.8 represents molecular dynamics simulation data obtained recently by Metatla et al. (2016) for the distribution of water molecules at three different densities (0.17, 0.31, and 0.55 g/cm^3) at 400 °C. The results show that for all densities studied, the underlying molecularity of SCW is heterogeneous and

characterized by low- and high-density regions. In other words, supercritical water can be viewed as existing as small but liquid-like hydrogen-bonded clusters dispersed within a gas-like phase, where physical properties, such as gas-like or liquid-like behavior, vary in response to changing density and the normal distinction between gas and liquid has disappeared. For a comprehensive review on the subject, see Guzonas et al. (2018); see also Kallikragas et al. (2015) who employed molecular dynamics simulations to investigate the properties of aqueous systems relevant to the SCWR.

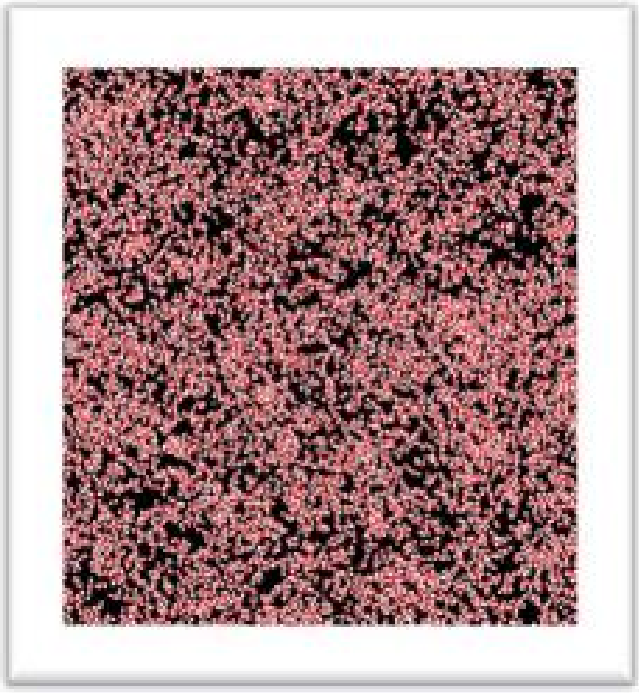

a)

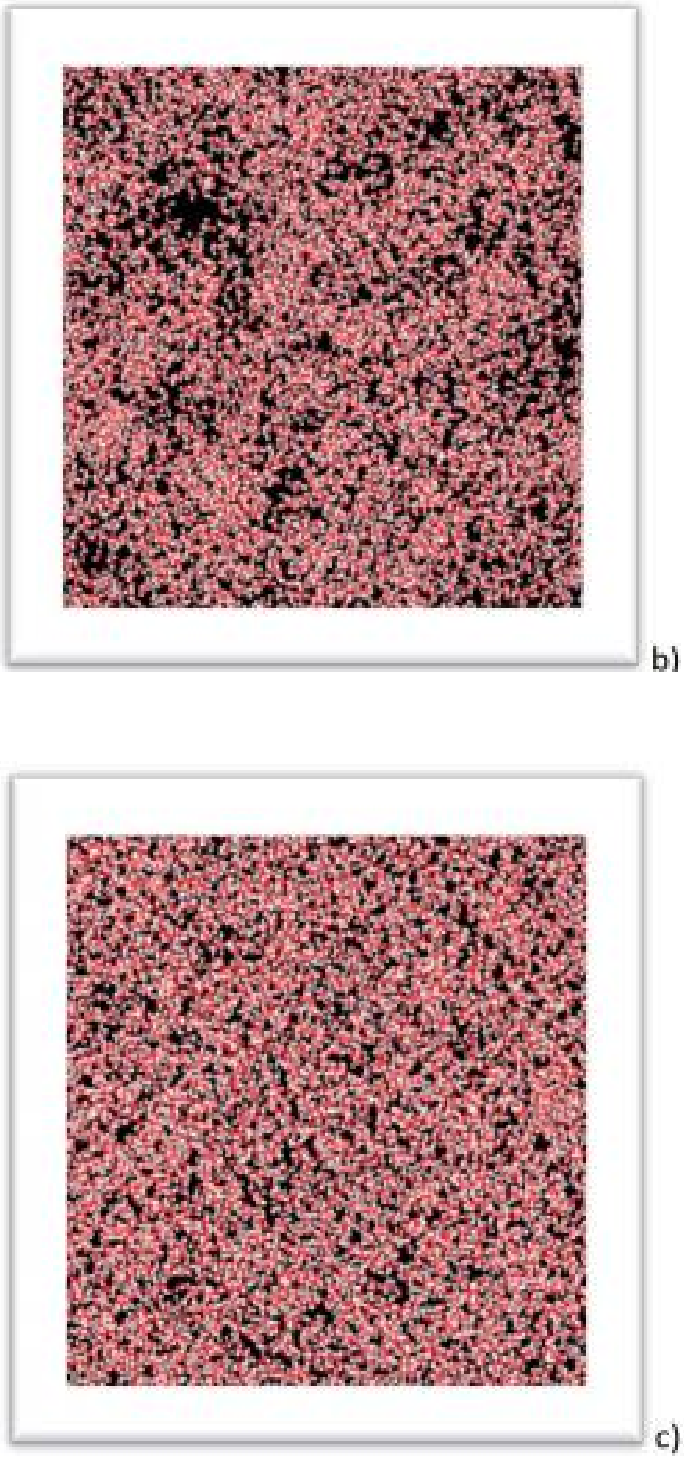

Figure 1.8 – Molecular dynamics simulations of the 3D distribution of water molecules for SCW at 400 °C and three different densities: (a) ρ = 0.17 g/cm^3, (b) ρ = 0.31 g/cm^3, and (c) ρ = 0.55 g/cm^3. The water's oxygen atoms are shown in red and the hydrogen in white. Adapted from Metatla et al. (2016).

1.13 Types of radiation in a nuclear power plant

If we examine the basic nuclear reactions in a nuclear power station, we see that the intervening reactions produce energetic neutrons and fission product fragments. Fission products can also be radioactive. These radioactive isotopes will emit α- or β-rays to transform ultimately into stable isotopes. Each emission of α- or β-rays will also be associated with the emission of γ-rays of energy in the range of 0.1-5 MeV (Tabata et al., 1991). On the other hand, there can be other forms of secondary pathways to produce other different types of radiations. For example, boron-10, generally used as a control rod in the system, may capture thermal or epithermal neutrons from the core and take part in boron-neutron capture reactions. Because of these $^{10}B(n,\alpha)^{7}Li$ nuclear reactions, the generation of high-LET recoil lithium-7 (^{7}Li) nuclei and α-particles can occur in the medium. Not all these types of radiation can have enough energy to initiate a spontaneous nuclear reaction, but their energy will be enough to ionize or excite a molecule of water to initiate spontaneous radiolysis phenomena.

1.14 Context of this work

From the mid of the last century, it has been a common scenario to extract the energy from nuclear reactions to produce electricity and other suitable forms of energy. The first nuclear reactors for this purpose were set-up in the 1950s and the technology gradually developed in later years (Goldberg and Rosner, 2011). In the development of a nuclear reactor, radiation chemistry occupies a prominent place. The radiation chemistry of water in the reactor core is of paramount importance in predicting the behavior of water under extreme conditions of very high temperatures and pressures and intense radiation fields. The overall corrosivity of materials due to the presence of a number of species generated by radiolysis has been the subject of numerous studies. In the near future, the radiation chemistry of supercritical water will have to be studied further, as the forthcoming installation of fourth-generation nuclear reactors is envisaged, one of the six possible models proposed being based on the use of SCW as the cooling liquid. Indeed, although much information of the radiation chemistry of sub-critical water is already available in the literature, only a small amount of data currently exists for supercritical water. In practice, it is very difficult to mimic the

situation in the laboratory as that in the reactor core. In addition, working under so extreme conditions of high temperatures and pressures is not trivial. That is why the simulation and modeling of these systems using computer programs becomes so much important. In our laboratory, we already have developed and implemented a program with which the complex phenomena of radiolysis can be simulated using Monte Carlo techniques (see Chap. 3).

In the present work, we have extended our original program to simulate the situation of high temperatures and pressures as that in a nuclear reactor core. Using this program, we calculated the yields of the various chemical species formed under these conditions from the radiolysis of water for both low- and high-LET radiations. It has already been known and described that the reactive species generated from water radiolysis, especially $^{\bullet}OH$, H_2O_2 and O_2, play a major role in the chemistry and corrosion inside the reactor core (Čuba et al., 2012.; Cook and Lister, 2014; Guzonas et al., 2018). Most interestingly, our calculations allowed us to observe, and this is largely the originality of this work, a sharp drop in pH in regions along the radiation trajectories. Even if this fall is local and temporary, the question is of course whether this acidity can affect or contribute to the corrosion of the construction materials of a nuclear reactor. In this regard, our work is an addition to the ongoing research on the radiation chemistry of the Gen-IV nuclear project.

2. OBJECTIVES

In the context of modern Gen IV SCWR development, it is necessary to obtain a better understanding of the chemistry that takes place inside a supercritical water-cooled reactor core. In fact, despite significant advances in recent years, our current state of knowledge of SCWR chemistry and materials is still limited to specify a chemistry control strategy, as the result of the large changes in physical and chemical properties of water through the critical point, coupled with the as yet poorly understood effects of water radiolysis (Guzonas et al., 2018). Of course, any breakthrough in this complex chemistry that underlies corrosions and other related problems of material degradation must go through a greater understanding of the mechanisms that cause them. In this work, our aim was to investigate a new possible mechanism of corrosion due to H^+ ions produced at early times in large concentrations during the radiolysis of SCW, and resulting in the *in situ* formation of very acidic regions ("acid spikes") along the trajectories of the radiation. To accomplish this goal, we have divided our work into the following three steps:

(1) Calculate the chemical yields of the various reactive species formed in the radiolysis of SCW at 400 °C as a function of water density in the range of ~0.15-0.6 g/cm^3.

(2) Focus on the *in situ* production of H^+ ions and quantify the resulting "acid-spike" response using specific radiation track models, characteristic of low- (300 MeV protons) and high- (2 MeV neutrons) LET radiation.

(3) Explain the role of this acidity as a possible mechanism to promote corrosion for common construction materials.

For the first two steps, we used the Monte Carlo track chemistry code developed in our laboratory. For the third step, we inferred and correlated the existing work in this field on literature because no experimental data was available. It is reasonable to propose that H^+ ions produced by radiolysis might have an impact on the mechanism of corrosion in SCWR.

3. METHODOLOGY

3.1. Monte Carlo track chemistry simulations

Monte Carlo methods (or Monte Carlo experiments) are a broad class of computational algorithms that rely on repeated random sampling to obtain numerical results. In these methods, a self-consistent and self-related information database is added with a statistical factor and this combination is used to predict some unknown parameters or results. Monte Carlo methods have been applied to an incredibly diverse range of physical processes and systems. Several important points need to be understood. First, we need to know what the desired results are and what will they be used for? Then we also need to know exactly how to define the inputs and, as well, how to model the underlying processes (Harrison, 2010).

This same approach is followed during the Monte Carlo simulation of the chemistry that takes place in the radiation track regions, where the complex events are reproduced from a self-related, step by step information database, and to which is added a statistical factor. The general objectives, in this case, are to predict the data for unknown results, to validate different hypotheses, to undertake a critical examination of proposed reaction mechanisms, and to estimate some other unknown parameters. The validity and accuracy of the calculations are then determined by comparison with data from an established system that has been examined previously using a wide variety of radiations and incident energies.

In general, we can say that a charged particle track is formed by all of the spatial products of ionization and excitation formed as the charged particle and all secondary particles (*e.g.*, secondary electrons produced via target ionization) set in motion slow down and stop in the "stopping medium". It has been described in earlier sections that all ionizing radiations from energetic electromagnetic radiations (*e.g.*, X- and γ-rays) to electrons, protons and heavy ions produce essentially the same types of products in the medium and the tracks consist of events (more or less) of similar types. The difference in the impact of these different types of radiation come mainly from the distribution of the interactions in time, energy, and space.

Historically, the investigation of the gradual slowing down and stopping of fast charged particles began with the discovery of the electron (Thomson, 1897) and the observation of its course in matter. While he was a new postdoctoral scientist at Rutherford's Laboratory at the University of Manchester, Bohr (1913) discovered that, there is a significant difference in the path of an electron and a α-particle. He came up with the concept of stopping power for a charged particle. This concept essentially lacked the details inside the trajectories due to the shortage of information at that time (Toburen, 2014). Later, it was understood that the energy deposition is a stochastic (*i.e.*, random) process that results in the formation of clusters of interactions of different sizes along with corresponding regions of no interactions along the track. This concept led to the idea of generation of track entities such as spurs, blobs, short tracks, *etc.* (Mozumder and Magee, 1966*a*,*b*), which ultimately led to the development of the first Monte Carlo track structure models beginning in the 1970s (Chatterjee et al., 1973; Chatterjee and Schaefer, 1976). It then became important to simulate the total track in an event-by-event manner. Heavy-ion track structure codes were first documented in a presentation by Paretzke (1974) at the 4th Symposium on Microdosimetry in Verbania-Pallanza, Italy. The models were then improved as more data on the subject became available and the power of the computers increased.

Turner and his coworkers at the Oak Ridge National Laboratory jointly with Magee and Chatterjee at Lawrence Berkeley Laboratory were the first to use Monte Carlo calculations to derive computer-plot representations of the chemical evolution of a few keV electron tracks in liquid water at times between ~10^{-12} and 10^{-7} s (Turner et al., 1983). Zaider and Brenner (1984) also used such an approach, and their calculated time-dependent yields of e^-_{aq} and $^{\bullet}OH$ radicals were somewhat similar to values measured or derived in pulse-radiolysis studies of pure water. Following these works, various codes employing Monte Carlo procedures were used with success to study the relationship between the initial track structure and the ensuing chemical processes that occur in the radiolysis of both water and water-containing solutes. Meesungnoen and Jay-Gerin (2011) have published a survey of literature pertaining to this subject, based on information available in 2009. Among the more recent works, one can mention here

those of Karamitros et al. (2011), Ramos-Méndez et al. (2018), and Boscolo et al. (2018).

In a program begun in the early 1990s, our group at the Université de Sherbrooke also developed and progressively refined, with very high levels of detail, several Monte Carlo codes that simulate the complex radiolysis of liquid water and aqueous solutions (Cobut, 1993; Cobut et al., 1998; Frongillo et al., 1998; Meesungnoen and Jay-Gerin, 2005; Meesungnoen, 2007; Plante, 2009; Tippayamontri et al., 2009; Meesungnoen et al., 2010; Meesat et al., 2012; Mirsaleh Kohan et al., 2013; Butarbutar et al., 2014*a*; Islam et al., 2017). These programs are still open and are continuously upgraded to include the latest information available. The most recent version, called IONLYS-IRT (Fig. 3.1), has been used in this work with the modifications necessary to take into account the type of ionizing radiation considered, and the large variations in temperatures and pressures studied, including the supercritical regime of water.

Briefly, the IONLYS step-by-step simulation program models all events of the physical and physicochemical stages of radiolysis. The IRT program covers the nonhomogeneous and homogeneous chemical stage and simulates the formation of measurable yields of chemical products. The detailed description and implementation of IONLYS-IRT has already been given (Meesungnoen and Jay-Gerin, 2005, and references therein) and will not be reproduced here, only a brief overview of the most essential features of the simulation methodology and reaction scheme, pertinent to the current calculations, is given in the sections below.

3.1.1. The random number generator

To perform the simulations, random numbers must be generated uniformly, distributed between 0 and 1. The question is how effectively a computer can efficiently generate random numbers? In reality, most random number generators that are used in Monte Carlo computer experiments are pseudo-random number generators, that is, they generate numbers repeatedly in a predictable (hence not truly “random”) fashion using a mathematical formula (Harrison, 2010). However, most algorithms used by the programs require random numbers. Since random numbers are called in several

different algorithms in our codes, there is quite a reduced probability that the same series of random numbers will intervene in the same algorithm. The pseudo-random number generator currently used in our programs is from Press et al. (1992). This generator has about ten lines of code and its period of "only" 2×10^9 is more than enough for our needs.

3.1.2. The IONLYS code

The IONLYS simulation code is used to cover the early "physical" and "physicochemical" stages of radiation action up to ~10^{-12} s. It is actually composed of two codes, one (named TRACPRO) for transporting the investigated incident charged particle (proton or any other heavy ion projectile) and another one (named TRACELE) for transporting all of the energetic electrons (collectively named "secondary electrons") that result from the passage of ionizing radiation in liquid water. The code models, event by event, all the basic physical interactions (energy deposition) and the subsequent establishment of thermal equilibrium in the system (conversion of the physical products created locally after completion of the physical stage into the various "initial" chemical species of the radiolysis).

The code begins by selecting a particular distance to the first interaction site for the incident particle. The calculation continues with the random choice of the type of interaction (ionization, excitation of electronic, vibrational and rotational levels of single water molecules, excitation of plasmon-type collective modes, and elastic scattering) that occurs. The probabilities or "cross-sections" for each of the different types of interaction of the particle are entered as input data in the code, based either on direct measurements or on theoretical estimates (Cobut, 1993; Cobut et al., 1998; Meesungnoen and Jay-Gerin, 2005). These collision cross sections are needed to follow the history of the incident particle. In particular, they provide the particle's "mean free path" used to determine the distance to the next interaction, the type of interaction at each event, energy loss, and the angle of emission of the scattered particle (for example, see: Nikjoo et al., 1997, 2012; Dingfelder et al., 2008).

If an inelastic collision is ionization, the particle's energy is reduced by the energy loss selected. The secondary electron produced is given a kinetic energy equal

to this energy loss minus the binding energy (or ionization energy) of the target electron. If a collision is elastic, an angle of scattering is selected and the flight distance for the next collision site is chosen. The computer simulation thus provides complete information on the spatial distribution of ionized and excited water, $H_2O^{\bullet+}$ and H_2O^*, and of all ejected energetic (or "dry") secondary electrons until they reach the subexcitation energy range (e^-_{sub}, energy < 7.3 eV; Michaud et al., 1991). This physical stage of radiation action is concluded in about 10^{-15} s.

It should be recalled here that our TRACPRO code uses protons as incident particles and is therefore well suited to the study of the fast-neutron radiolysis of water, since the ionizing particles involved in this case are proton and oxygen ion recoils (Tippayamontri et al., 2009). The choice of proton impact in the Sherbrooke code was initially adopted because protons offer, by far, the most comprehensive database of cross sections for bare ion collisions (not only on water but also on a number of different target atoms or molecules; for example, see: Rudd, 1990; Rudd et al., 1992; IAEA-TECDOC-799, 1995; Dingfelder et al., 2000; Toburen, 2004), and because also they constitute a valuable tool for studying LET effects on radiolytic yields (Cobut et al., 1998).

Another great advantage of the code is that, while it was devised for protons, it can also be used for heavier ion projectiles by assuming that the interaction cross sections scale as Z^2, where Z is the projectile charge number. In this scaling procedure, based on the lowest-order (or first Born) approximation of perturbation theories, the cross sections for bare ion impact are approximately Z^2 times the cross sections for proton impact at the same velocity. This simple Z^2 scaling rule, which holds at sufficiently high impact energies (say, above ~1 MeV/nucleon) where the interactions are not too strong, is particularly useful for providing cross sections for ionization and excitation by ion projectiles. This is even truer that there are only limited experimental data available involving ions heavier than proton or helium in collision with water molecules (Inokuti, 1971; Meesungnoen and Jay-Gerin, 2005).

The simulations performed with IONLYS consist in the generation of short high-energy proton (ion) track segments in water. The primary particle is simulated

until it has penetrated the chosen length of the track segment into the medium. Note that, due to its large mass, the proton (or the impacting heavy ion) is almost not deflected by collisions with the target electrons. In the present simulations, these deflections are simply neglected. The use of small path segments is particularly useful as the instantaneous LET of the incident particle is nearly constant over such segments and can be varied simply by changing its energy.

The IONLYS code also covers the physicochemical stage of the radiolysis, which consists of the processes that lead to the re-establishment of thermal equilibrium in the bulk medium with reactions and reorganization of initial products to give new chemical species such as stable molecules and water free radicals (Fig. 3.2). It lasts ~10^{-12} s. The various events that can take place during this stage have been described in detail in Sect. 1.5.2 (see also Fig. 1.3) and therefore will not be discussed again here. We add only a few comments below.

The excited water molecules can lose their extra energy either through dissociative or non-dissociative channels as shown in Fig. 1.3. Unfortunately, these decay channels remain largely unknown for *liquid* water. The branching ratios (or decay probabilities) associated with the different competing de-excitation reactions (1.l)-(1.o) are essentially treated as adjustable parameters (Cobut et al., 1998; Muroya et al., 2002; Meesungnoen and Jay-Gerin, 2005; Sanguanmith et al., 2011). It should be mentioned here, however, that the contribution of the water excited states to the free radical and molecular products in water radiolysis is of relatively minor importance in comparison with that of the ionization processes, so that the lack of information about their decomposition has only limited consequences.

Ogura and Hamill (1973) pointed out that the water cation ($H_2O^{\bullet +}$) may migrate (randomly) during its very short lifetime (~200 fs) by means of a sequence of resonant electron transfers from neighboring water molecules to the $H_2O^{\bullet +}$ hole. Our program includes this possibility of positive hole jumps, with an average of 21 jumps before the proton transfer reaction (1.g) occurs.

The time that a secondary electron takes to reach a subexcitation energy is <10^{-15} s. The thermalization of e^-_{sub} is treated by IONLYS using a distribution of

thermalization distances previously obtained by our group (Goulet and Jay-Gerin, 1988; Goulet et al., 1990, 1996; Cobut et al., 1998) from Monte Carlo track-structure calculations based on the experimental scattering cross sections of slow (1–18 eV) electrons in amorphous ice of Michaud and Sanche (1987) with corrections to account for the liquid phase. Given the initial position of the subexcitation electron, its position is simply displaced in a randomly selected, isotropic direction by the corresponding, energy-dependent mean thermalization distance. At this new position, the electron is regarded as thermalized and subsequently trapped and hydrated. Let us mention, however, that the IONLYS code does not take into account the possibility for very low energy (*e.g.*, "sub-vibrational") electrons in a highly polar medium such as liquid water – where it exists a large density of possible electron trapping sites – to become trapped instantly *prior to thermalization* (Mozumder, 1999). It is also worth recalling here that a certain proportion of subexcitation electrons actually never get thermalized, but instead undergo prompt recombination with their positive parent ion $H_2O^{\bullet+}$ or dissociative attachment (DEA) onto a surrounding H_2O molecule (Cobut et al., 1996; Platzman, 1962*b*; Ram et al., 2009) (Fig. 1.3). All details about the various parameters intervening in IONLYS to describe this competition between thermalization, geminate recombination, and DEA, as well as the values of the branching ratios used in the code for the different de-excitation channels of the excited water molecules, can be found in Sanguanmith et al. (2011).

3.1.3. The IRT code

The complex spatial distribution of species at the end of the physicochemical stage, which is provided as an output of the IONLYS program, is then directly used as a starting point for the chemical stage, which comprises a nonhomogeneous chemistry part followed by a part of homogeneous chemistry. In this stage, the reactive species diffuse randomly at rates determined by their diffusion coefficients, and react with one another (or, competitively, with any added solutes present at the time of irradiation) until all spur or track processes are complete and the species are homogeneously distributed in the solution (μs timescale). This stage is covered by the IRT program, which uses the "independent reaction times" method (Clifford et al., 1986; Pimblott et

al., 1991; Frongillo et al., 1998) to calculate reaction times without having to follow the trajectories of the diffusing species. This computer efficient stochastic simulation technique relies on the approximation that the distances between pairs of reactants evolve independently of each other, and therefore the reaction times of the various potentially reactive pairs are independent of the presence of other reactants in the system.

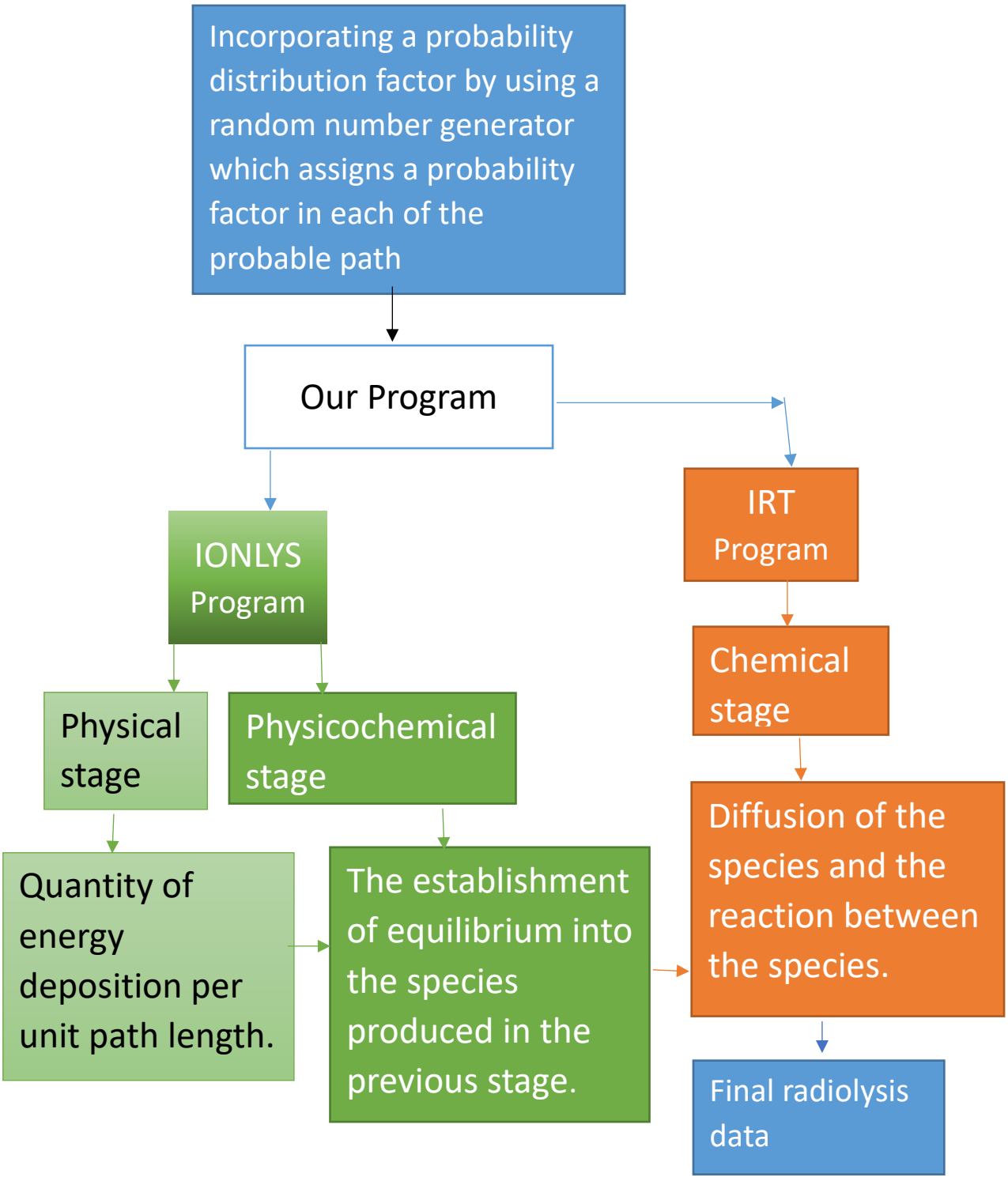

Figure 3.1 – Structure of our Monte Carlo track chemistry simulation code IONLYS-IRT.

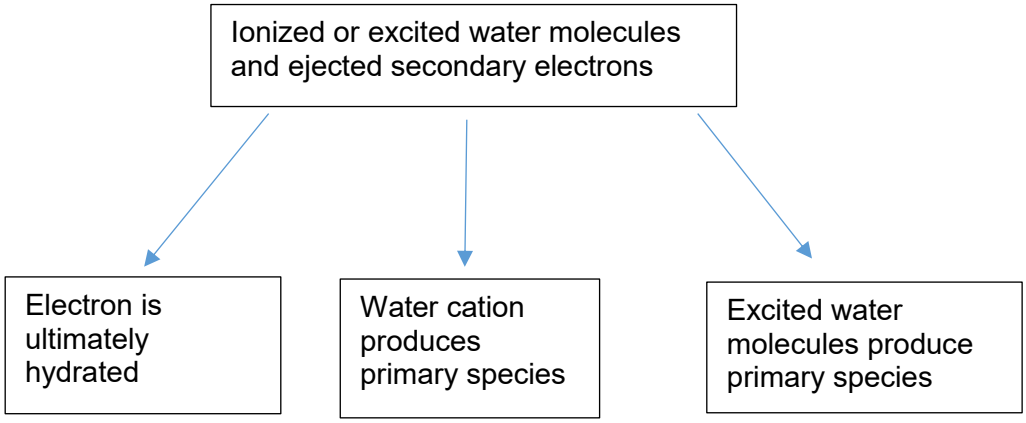

Figure 3.2 – Events occurring in the physicochemical stage covered by IONLYS.

Among the stochastic approaches, the most reliable and the closest to reality is certainly the full random flights or "step-by-step" (SBS) simulation, which does follow – contrary to the IRT approach – the reactant trajectories in detail. This method has been relatively little used so far because it can be exceedingly consuming in computing time when large radiation chemical systems (such as complete radiation tracks or even track segments especially at high LET, elevated temperatures or yet under high dose-rate conditions) are studied. However, this method is likely to develop considerably in the near future, given the constant improvement of computer performance in terms of capacity and speed of calculation (Plante and Devroye, 2017).

The IRT method was originally designed to allow much faster realisations than with the full Monte Carlo model, and can be summarized as follows. For every potentially reactive pair, a reaction time is stochastically sampled according to the time-dependent survival function (Green et al., 1990; Goulet and Jay-Gerin, 1992; Frongillo et al., 1998) that is appropriate for the type of reaction considered. This function depends on the initial (or zero-time) distance separating the species, their diffusion coefficients, their Coulomb interaction (for reactions between ionic species), their reaction radius, and the probability of reaction during one of their encounters. The first reaction time is obtained by taking the minimum of the resulting set of reaction times, and allowing the corresponding pair of species to react at that moment. This procedure

for modeling reaction is continued either until all reactions are completed or until a pre-defined cut-off time is reached.

To simply visualize the functioning of the IRT method, consider a solution with four species A, B, A, and C (Fig. 3.3). The program will first calculate the chances of reacting for each of the six possible reaction pairs. Now consider that the reaction between B and C is most likely to occur. Thus, these species will react to form D and E with their new spatial location. The IRT program will recalculate the chances of reacting for all new existing reaction pairs, and so on. This process continues until the end and allows to calculate the yields of all species at any particular time.

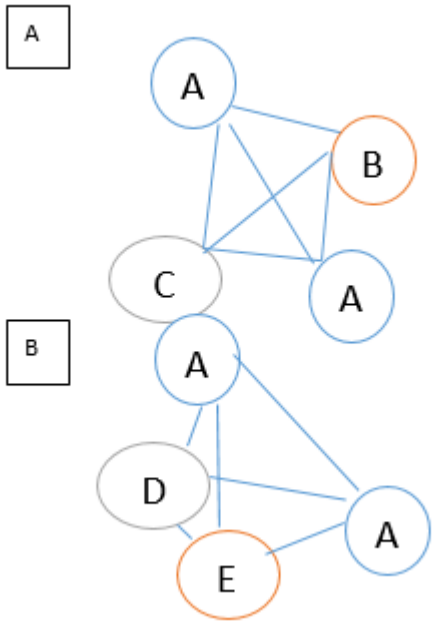

Figure 3.3 – Illustration of the basic principle of the IRT method. (A) Interaction between the initial species. (B) Interaction between species after the first reaction between B and C has occurred.

Most interestingly, the IRT program allows one to incorporate in a simple way pseudo first-order reactions of the radiolytic products with various scavengers that are homogeneously distributed in the solution, such as H^+, OH^-, and H_2O itself, or more generally any solutes for which the relevant reaction rates are known. Similarly, the truly first-order fragmentations of the species are easily simulated. In addition, the IRT method is very well suited for the description of reactions that are only partially

diffusion-controlled (most reactions that occur in irradiated water are not diffusion-controlled even at room temperature). An adequate description of the activation processes that are involved in those reactions is a prerequisite for the modelling of the effects of high temperature on water radiolysis, in which the species do not react instantaneously on encounter but experience, on the average, many encounters and separations before they actually react with each other (Hervé du Penhoat et al., 2000). The ability of the IRT method to give accurate time-dependent chemical yields under different irradiation conditions has been well validated by comparison with full random flights Monte Carlo simulations (Plante, 2009).

Beyond a few microseconds, all spurs or tracks have dissipated, and the reactions that occur in the bulk solution can usually be described with conventional homogeneous chemistry methods (Pastina and LaVerne, 2001). This is the so-called stage of "homogeneous chemistry". The radical and molecular products which emerge from the spurs/tracks are then available to react with solutes (treated as spatially homogeneous) present in low or moderate concentrations. Of course, the IRT program can also be used to simulate efficiently this second part of the chemical stage.

Table 3.1 gives the set of reactions that are likely to occur in the chemical stage of the radiolysis of liquid water. The corresponding reaction rate constants at room temperature are taken from the compilation of Elliot and Bartels (2009).

As mentioned previously (Sect. 1.8), fast neutrons impinging on liquid water at incident energies less than ~10 MeV generate primarily energetic recoil protons and to a smaller extent oxygen ion recoils. For the estimation of the radiation chemical yields due to 2 MeV neutrons – energy considered to be representative of the average initial energy of a fast neutron flux in a reactor (see: Elliot and Bartels, 2009) –, only the contribution of the *first three recoil protons* was considered in the calculations. Indeed, further recoil protons generated by the neutron as it is further moderated do not contribute significantly to radiolysis due to their low average energies (Butarbutar et al., 2014*a*,*b*; Tippayamontri et al., 2009; Swiatla-Wojcik and Buxton, 1998). Using Eq. (1.ee), the *initial* proton energies $E_{p_{i=1,2,3}}$ are 1.264, 0.465, and 0.171 MeV. The fast neutron yields were calculated using Eqs. (1.ff) and (1.gg) by summing the *G*-values

associated with each recoil proton considered (as determined by our Monte Carlo simulations; see *infra*), weighted by its fraction of total neutron energy deposited (Gordon et al., 1983; Elliot and Bartels, 2009; Tippayamontri et al., 2009; Butarbutar et al., 2014*a*,*b*).

We considered the fact that, given their limited ranges, all the recoil protons are completely stopped in the water. The chemistry measured under these conditions is thus an average over the proton energies from the initial proton energy to zero. To avoid complexity arising from the resulting variations in the energy of the moving protons, simulations were performed with the simplifying approximation that the energies of the three considered recoil protons remained constant when passing through the water medium. These constant *dose-average energy* values $\overline{E}_{p_{i=1,2,3}}$ were obtained according to a procedure described previously (Islam et al., 2017, 2018) using the SRIM software (Ziegler et al., 2015; see *infra*) and our own Monte Carlo track structure simulations (see Chap. 5). They were found to be ~0.6, 0.3, and 0.17 MeV, respectively. Interestingly, these values varied only slightly (at most ~5%) as a function of water density over the studied range of ~0.15-0.6 g/cm^3 and were therefore kept constant in all our chemical yield calculations regardless of the density.

All our calculations were performed by simulating short (typically, ~15-150 μm) proton track segments, over which the energy and LET of the recoil protons remain nearly constant. Such model calculations thus gave "track segment" yields (LaVerne, 2000, 2004) at a well-defined LET as a function of time. For the three recoil protons under consideration, whose dose-average energies are $\overline{E}_{p_{i=1,2,3}}$ ~ 0.6, 0.3, and 0.17 MeV, respectively, the corresponding mean LET values increase from ~5.5, 8.2, and 10.4 keV/μm to ~22, 33, and 42 keV/μm when the water density is increased from 0.15 to 0.6 g/cm^3. This LET range allows the proton's track to be modeled as a cylinder, characteristic of high-LET radiation (see *infra*). The number of individual proton "histories" (usually ~10-150, depending on the proton energy) was chosen to ensure only small statistical fluctuations in the computed averages of chemical yields, while meeting acceptable computer time limits.

Reaction	$k\ (M^{-1}\,s^{-1})$	Reaction	$k\ (M^{-1}\,s^{-1})$
$H^{\bullet} + H^{\bullet} \rightarrow H_2$	5.2×10^{9}	$e^{-}_{aq} + e^{-}_{aq} \rightarrow H_2 + 2\,OH^{-}$	7.3×10^{9}
$H^{\bullet} + {}^{\bullet}OH \rightarrow H_2O$	1.6×10^{10}	$e^{-}_{aq} + H^{+} \rightarrow H^{\bullet}$	2.1×10^{10}
$H^{\bullet} + H_2O_2 \rightarrow H_2O + {}^{\bullet}OH$	3.6×10^{7}	$e^{-}_{aq} + O_2^{\bullet-} \rightarrow H_2O_2 + 2\,OH^{-}$	1.3×10^{10}
$H^{\bullet} + e^{-}_{aq} \rightarrow H_2 + OH^{-}$	2.8×10^{10}	$e^{-}_{aq} + HO_2^{-} \rightarrow O^{\bullet-} + OH^{-}$	3.51×10^{9}
$H^{\bullet} + OH^{-} \rightarrow H_2O + e^{-}_{aq}$	2.4×10^{7}	$e^{-}_{aq} + O^{\bullet-} \rightarrow 2\,OH^{-}$	2.31×10^{10}
$H^{\bullet} + O_2 \rightarrow HO_2^{\bullet}$	1.3×10^{10}	$e^{-}_{aq} + H_2O \rightarrow H^{\bullet} + OH^{-}$	15.8
$H^{\bullet} + HO_2^{\bullet} \rightarrow H_2O_2$	1.1×10^{10}	$e^{-}_{aq} + O_2 \rightarrow O_2^{\bullet-}$	2.3×10^{10}
$H^{\bullet} + O_2^{\bullet-} \rightarrow HO_2^{-}$	1.1×10^{10}	$e^{-}_{aq} + HO_2^{\bullet} \rightarrow HO_2^{-}$	1.3×10^{10}
$H^{\bullet} + HO_2^{-} \rightarrow {}^{\bullet}OH + OH^{-}$	1.5×10^{9}	$e^{-}_{aq} + O(^3P) \rightarrow O^{\bullet-}$	2.0×10^{10}
$H^{\bullet} + O(^3P) \rightarrow {}^{\bullet}OH$	2.0×10^{10}	$e^{-}_{aq} + O_3 \rightarrow O_3^{\bullet-}$	3.6×10^{10}
$H^{\bullet} + O^{\bullet-} \rightarrow OH^{-}$	2.0×10^{10}	$H^{+} + O^{\bullet-} \rightarrow {}^{\bullet}OH$	5.0×10^{10}
$H^{\bullet} + O_3 \rightarrow O_2 + {}^{\bullet}OH$	3.7×10^{10}	$H^{+} + O_2^{\bullet-} \rightarrow HO_2^{\bullet}$	5.0×10^{10}
$H^{\bullet} + O_3^{\bullet-} \rightarrow OH^{-} + O_2$	1.0×10^{10}	$H^{+} + OH^{-} \rightarrow H_2O$	1.2×10^{11}
${}^{\bullet}OH + {}^{\bullet}OH \rightarrow H_2O_2$	6.3×10^{9}	$H^{+} + O_3^{\bullet-} \rightarrow {}^{\bullet}OH + O_2$	9.0×10^{10}
${}^{\bullet}OH + H_2O_2 \rightarrow HO_2^{\bullet} + H_2O$	2.9×10^{7}	$H^{+} + HO_2^{-} \rightarrow H_2O_2$	5.0×10^{10}
${}^{\bullet}OH + H_2 \rightarrow H^{\bullet} + H_2O$	4.0×10^{7}	$OH^{-} + O(^3P) \rightarrow HO_2^{-}$	4.2×10^{8}
${}^{\bullet}OH + e^{-}_{aq} \rightarrow OH^{-}$	3.6×10^{10}	$OH^{-} + HO_2^{\bullet} \rightarrow O_2^{\bullet-} + H_2O$	1.3×10^{10}
${}^{\bullet}OH + OH^{-} \rightarrow O^{\bullet-} + H_2O$	1.3×10^{10}	$O_2 + O^{\bullet-} \rightarrow O_3^{\bullet-}$	3.7×10^{9}
${}^{\bullet}OH + HO_2^{\bullet} \rightarrow O_2 + H_2O$	9.0×10^{9}	$O_2 + O(^3P) \rightarrow O_3$	4.0×10^{9}
${}^{\bullet}OH + O_2^{\bullet-} \rightarrow O_2 + OH^{-}$	1.1×10^{10}	$HO_2^{\bullet} + O_2^{\bullet-} \rightarrow HO_2^{-} + O_2$	9.7×10^{7}
${}^{\bullet}OH + HO_2^{-} \rightarrow HO_2^{\bullet} + OH^{-}$	8.3×10^{9}	$HO_2^{\bullet} + HO_2^{\bullet} \rightarrow H_2O_2 + O_2$	1.94×10^{8}
${}^{\bullet}OH + O(^3P) \rightarrow HO_2^{\bullet}$	2.02×10^{10}	$HO_2^{\bullet} + O(^3P) \rightarrow O_2 + {}^{\bullet}OH$	2.02×10^{10}
${}^{\bullet}OH + O^{\bullet-} \rightarrow HO_2^{-}$	1.0×10^{9}	$HO_2^{\bullet} + H_2O \rightarrow H^{+} + O_2^{\bullet-}$	1.4×10^{4}
${}^{\bullet}OH + O_3^{\bullet-} \rightarrow O_2^{\bullet-} + HO_2^{\bullet}$	8.5×10^{9}	$O_2^{\bullet-} + O^{\bullet-} \rightarrow O_2 + 2\,OH^{-}$	6.0×10^{8}
${}^{\bullet}OH + O_3 \rightarrow O_2 + HO_2^{\bullet}$	1.11×10^{8}	$O_2^{\bullet-} + H_2O \rightarrow HO_2^{\bullet} + OH^{-}$	0.155
$H_2O_2 + e^{-}_{aq} \rightarrow OH^{-} + {}^{\bullet}OH$	1.1×10^{10}	$O_2^{\bullet-} + O_3 \rightarrow O_3^{\bullet-} + O_2$	1.5×10^{9}
$H_2O_2 + OH^{-} \rightarrow HO_2^{-} + H_2O$	1.33×10^{10}	$HO_2^{-} + H_2O \rightarrow H_2O_2 + OH^{-}$	1.27×10^{6}
$H_2O_2 + O(^3P) \rightarrow HO_2^{\bullet} + {}^{\bullet}OH$	1.6×10^{9}	$HO_2^{-} + O^{\bullet-} \rightarrow O_2^{\bullet-} + OH^{-}$	8.02×10^{8}
$H_2O_2 + O^{\bullet-} \rightarrow HO_2^{\bullet} + OH^{-}$	5.55×10^{8}	$HO_2^{-} + O(^3P) \rightarrow O_2^{\bullet-} + {}^{\bullet}OH$	5.3×10^{9}
$H_2 + O(^3P) \rightarrow H^{\bullet} + {}^{\bullet}OH$	4.77×10^{3}	$O^{\bullet-} + O^{\bullet-} \rightarrow H_2O_2 + 2\,OH^{-}$	1.0×10^{8}
$H_2 + O^{\bullet-} \rightarrow H^{\bullet} + OH^{-}$	1.3×10^{8}	$O^{\bullet-} + O_3^{\bullet-} \rightarrow 2\,O_2^{\bullet-}$	7.0×10^{8}
$O(^3P) + O(^3P) \rightarrow O_2$	2.2×10^{10}	$O^{\bullet-} + H_2O \rightarrow {}^{\bullet}OH + OH^{-}$	1.3×10^{6}
$O(^3P) + H_2O \rightarrow 2\,{}^{\bullet}OH$	1.9×10^{3}	$O_3^{\bullet-} + H_2O \rightarrow O^{\bullet-} + O_2$	46.5

Table 3.1 – Main reaction scheme and corresponding rate constants (k) used in the IRT program of the radiolysis of pure liquid water at 25 °C.

3.1.4 Accounting for the radiolysis of supercritical water at 400 °C

For our simulations of the radiolysis of SCW at 400 °C by impacting protons of various initial energies, we used an extended version of the IONLYS-IRT code adapted to these irradiation conditions. Given the very limited number of experimental data available in this temperature range, several approximations and assumptions have been made in this version for the description of some key parameters involved in the physicochemical and chemical stages of radiolysis. These changes are summarized as follows.

(1) We assumed that, at 400 °C, the thermalization distance (r_{th}) of subexcitation-energy electrons e^-_{sub} (those with kinetic energies lower than ~7.3 eV, the first-electronic excitation threshold in liquid water) is only affected by changes in the water density (ρ) and we scaled it according to a $(1/\rho)^{1/3}$ law (Swiatla-Wojcik and Buxton, 1995), namely,

$$r_{th}\left(400\,^{\circ}\mathrm{C},\rho\right) = r_{th}\left(400\,^{\circ}\mathrm{C},\rho=0.6\ \mathrm{g/cm^3}\right)\left[\frac{0.6\ \mathrm{g/cm^3}}{\rho}\right]^{1/3}, \qquad (3.a)$$

with $r_{th}\left(400\,^{\circ}\mathrm{C},\rho=0.6\ \mathrm{g/cm^3}\right)\approx 3.2\ \mathrm{nm}$ (Muroya et al., 2012). This means that decreasing density further separates the water molecules but does not change their ability to interact with the energetic subexcitation electrons, resulting in an increase of r_{th}.

(2) We included in the simulations a prompt geminate electron-cation ($H_2O^{\bullet+}$) recombination (*i.e.*, prior to thermalization of the e^-_{sub}) that decreased in irradiated SCW at 400 °C as the water density decreased from ~0.6 to 0.15 g/cm^3 (Meesungnoen et al., 2013).

(3) We used the rate constants predicted recently by Liu et al. (2016, 2018) for a number of reactions involved in the radiolysis of SCW at 400 °C, based on the so-called cage effect model developed by these authors to account for the non-Arrhenius temperature dependence of many reactions in water. Given the lack of experimental data, this new database is important in providing us with recommendations for the best rate constant values to use at this time in modeling the radiolysis of SCW near and

above the critical point. In some cases, we also used the chemical kinetic data compiled by Elliot and Bartels (2009), simply extrapolated above their experimentally measured temperature ranges (mostly 20-350 °C), as well as the recent pulse radiolysis measurements of Muroya et al. (2017) for the rate constant of the radiation-induced reaction $H^{\bullet} + H_2O \rightarrow H_2 + {}^{\bullet}OH$, a key reaction in high-temperature water radiolysis. In the absence of any other information, we chose to neglect any dependence of the reaction rate constants on water density for the 400 °C isotherm of interest. In the 0.15-0.6 g/cm^3 range studied here, this approximation does not appear to have a large impact, considering the relatively slowly varying *k* values for the few reactions whose rates have been measured as a function of SCW density (Butarbutar et al., 2014*a*; Sanguanmith et al., 2016).

(4) From a microscopic perspective, we ignored the heterogeneous character of the molecular structure of SCW (Metatla et al., 2016) originating from the presence of density fluctuations (or water "clustering") associated with criticality. In this study, we assumed that the overall instantaneous picture of SCW at 400 °C could simply be viewed as a *continuum* medium with a mean density equal to the density of bulk water. This approximation was shown to be reasonable in determining the radiation chemistry of SCW at 400 °C at the water densities considered here, in particular the yields of e^-_{aq} measured directly at ~60 ps and 1 ns by pulse radiolysis experiments (Meesungnoen et al., 2010; Muroya et al., 2010, 2012; Sanguanmith et al., 2012, 2016) (see *infra*).

The density (pressure) dependence of the self-diffusion coefficient of compressed SCW at 400 °C was taken from the measurements of Lamb et al. (1981) in the region from 0.1 to 0.7 g/cm^3. For the diffusion coefficients of the species ${}^{\bullet}OH$, $H^{\bullet}$, H_2O_2, and H_2, which have been explicitly determined only at 25 °C but are essentially unknown at 400 °C, we have assumed that they scale proportionally to the self-diffusion of water above room temperature (Hervé du Penhoat et al., 2000; Meesungnoen et al., 2010). The diffusion coefficients of e^-_{aq}, H^+, and OH^- were extrapolated from the data reported by Elliot and Bartels (2009) over the 20-350 °C temperature range. For all species, we assumed that the dependence of *D* on density at 400 °C equalled that of the self-diffusion coefficient of compressed SCW at this temperature. The density

dependences of the viscosity, static dielectric constant, and molar concentration of SCW at 400 °C used in this work were taken from the NIST Chemistry WebBook (2018). The values for the ionic product of water (K_w) were obtained from Bandura and Lvov (2006).

Throughout this work, *G*-values are quoted in units of molecules formed or consumed per 100 eV of radiation energy absorbed. For conversion into SI units, 1 molecule/100 eV = 0.10364 μmol/J.

3.1.5 Models for pH calculation

In order to calculate the pH values prevailing in spur or track regions at 400 °C, we need to estimate the concentrations of H_3O^+ generated in these regions as a function of time. Two models are considered *depending on the quality (LET) of the radiation*.

For radiations of low energy transfer (such as ~300 MeV incident protons; LET ~ 0.3 keV/μm), we assume that the hydronium ions are produced evenly in an isolated *spherical* "spur" whose initial radius r_o (*i.e.*, prior to spur expansion at ~1 ps), is equal to the average electron thermalization distance (r_{th}) obtained from Eq. (3.a). The low-LET spur concentrations of radiolytically generated H_3O^+ can be derived from

$$\left[\mathrm{H_3O^+}\right]_{\text{radiolytic}}(t) = G\left(\mathrm{H_3O^+}\right)(t) \times \left(\frac{\textit{Mean energy loss per event}}{\frac{4}{3}\pi\, r(t)^3} \right), \tag{3.b}$$

where the mean energy loss in a single event (*i.e.*, the mean energy deposited in a spur) is taken to be ~47 eV (Cobut et al., 1998; Autsavapromporn, 2006; Mirsaleh Kohan et al., 2013) and

$$r(t)^2 = r_o^{\,2} + 6Dt \tag{3.c}$$

represents the change with time of r_o due to the (three dimensional) diffusive expansion of the spur. Here, *t* is time and *D* is the diffusion coefficient of H_3O^+ in water.

In the case of radiations of high linear energy transfer (such as the neutron/recoil protons under consideration in this study), we consider the track as being a *cylinder*, homogeneous along its axis, with a length L = 1 μm and initial radius r_c equal to the radius of the physical track "core" (Magee and Chatterjee, 1987; Mozumder, 1999). In this case, the high-LET track concentrations of radiolytically generated H_3O^+ can be obtained from

$$\left[\mathrm{H_3O^+}\right]_{\text{radiolytic}}(t) = G\left(\mathrm{H_3O^+}\right)(t) \times \left(\frac{\text{LET}}{\pi\, r(t)^2}\right), \tag{3.d}$$

where

$$r(t)^2 = r_c^2 + 4Dt \tag{3.e}$$

represents the change with time of r_c due to the (two dimensional) diffusive expansion of the track. Here, r_c was estimated directly from our simulations and was taken to be ~2 nm for all recoil protons and all considered densities.

Finally, the *total* concentration of H_3O^+ is the sum of $[H_3O^+]_{\text{radiolytic}}$ given by Eqs. (3.b-3.c) (isolated "spherical" spur) and (3.d-3.e) (axially homogeneous "cylindrical" track) and of the non-radiolytic, pre-irradiation concentration $[H_3O^+]_{\text{autoprotolysis}}$ that results from the autoprotolysis of water (Kanike et al., 2017; Islam et al., 2018; Bandura and Lvov, 2006):

$$\left[\mathrm{H_3O^+}\right]_{\text{total}}(t) = \left[\mathrm{H_3O^+}\right]_{\text{radiolytic}}(t) + \left[\mathrm{H_3O^+}\right]_{\text{autoprotolysis}}. \tag{3.f}$$

The pH in the corresponding spur/track regions is then simply given by the negative logarithm (to the base 10) of $[H_3O^+]_{\text{total}}$:

$$\mathrm{pH}(t) = -\log\left\{\left[\mathrm{H_3O^+}\right]_{\text{total}}(t)\right\}, \tag{3.g}$$

3.2 SRIM simulations

SRIM (for "Stopping and Range of Ions in Matter") is a most widely used software code for determining the stopping and range of ions in matter based on accurate experimental data and extending these values using unified theoretical

concepts. A recent textbook describes in detail the fundamental physics of the software (Ziegler et al., 2015). The first approach to such a determination was initiated with its precursor TRIM (for "Transport of Ions in Matter") in the early 1980's (Biersack and Eckstein, 1984; Zeigler and Reynolds, 1985; Ziegler et al., 2010, 2015). Since then, it has been continuously updated, with corrections made on the basis of new experimental data. The program is based on a Monte Carlo simulation method, using the "binary collision approximation" in its calculations with a random selection of the impact parameter of the next colliding ion.

The core concept of this simulation is the Bragg rule (Bragg and Kleeman, 1905; Thwaites, 1983), according to which "the stopping power of a compound may be estimated by a linear combination of the stopping powers of its individual elements". In this approach, it is assumed that each individual collision is a two-body problem, ignoring possible effects from nearby atoms in the target. In fact, any differences between bonding in elemental materials and in compounds will cause Bragg's simple additivity of stopping powers to become inaccurate. It is of course not our intention here to review the complex and extensive theoretical work on stopping in compounds. Let us just point out that much of this work derives its origin from a seminal paper of Sigmund (1982) who developed methods to account for detailed internal motion within a medium. This theory allowed for arbitrary electronic configurations in the target. In this context, SRIM's remarkable success was to estimate in a simple way bonding corrections to stopping that compounds introduce to the use of Bragg's rule to generate stopping power of compounds accurate to a few percent. In short, SRIM uses a method called the "Core and Bond" (CAB) approach (Both et al., 1983) that proposes approaching the problem by reducing each target atom to two parts: the *core electrons* which are unperturbed by bonding, and the *bonding electrons* depending on how the atom is bound into the compound. The core stopping simply follows Bragg's rule for the atoms of the compound, where we linearly add the stopping from each of the atoms in the compounds. The chemical bonds of the compounds then contain the necessary stopping correction.

SRIM uses CAB corrections for the stopping of ions in compounds containing the common elements: H, C, N, O, F, S, and Cl. These light atoms have the largest

bonding effect on stopping powers. Heavier atoms are assumed not to contribute anomalously to stopping because of their bonds. SRIM correctly predicts the stopping of H and He ions in compounds with an accuracy of better than 2% at the peak of the stopping curve, 125 keV/nucleon.

In practice, as input parameters, the program first asks for the type of ion and energy to use, and then the constituents of the target as well as their distribution in one or more layers of defined thickness. We have the option to use the "Compound Dictionary" which contains the chemical bonding information for about 150 common compounds, including water in either gaseous or solid state. When these compounds are selected, SRIM calculates the best stopping correction. As for the output, the program generates tables, plots, diagrams, and data files providing information on the final three-dimensional distribution of the ions in the target, ion range (penetration depth), straggling (variation of ranges of ions about their mean values, along the ion beam and perpendicular to it), backscattered ions and transmitted ions, ion implantation, *etc*. It will also calculate all kinetic phenomena associated with the ion's energy loss: target damage, sputtering (removal of near-surface atoms from the target), ionization, and energy transferred to recoil atoms (Ziegler et al., 2015).

In the current study, we used the SRIM software to calculate the trajectories of the first three proton recoils generated by the slowing-down of 2 MeV neutrons in SCW at 400 °C and various densities, as well as the energies and LET values of these recoils as a function of penetration depth.

4. ARTICLE

Formation de « pics d'acidité » dans la radiolyse de l'eau supercritique à 400 °C par des neutrons de 2 MeV. Une étude par simulation Monte Carlo

par

Md Mohsin Patwary, Sunuchakan Sanguanmith, Jintana Meesungnoen et

Jean-Paul Jay-Gerin*

Département de médecine nucléaire et de radiobiologie, Faculté de médecine et de santé de la santé, Université de Sherbrooke, 3001, 12ème avenue Nord, Sherbrooke (Québec) J1H 5N4, Canada

RÉSUMÉ

Une compréhension fiable des processus de radiolyse dans les réacteurs à eau supercritique (ESC) est nécessaire pour assurer un contrôle optimal de la chimie de l'eau. Des simulations Monte Carlo de la radiolyse de l'ESC à 400 °C par des neutrons mono-énergétiques de 2 MeV ont été effectuées en fonction de la densité de l'eau entre 0.15 et 0.6 g/cm^3. Il a été montré que la formation *in situ* de H_3O^+ par les protons de recul formés rendait les régions des trajectoires très acides (pH ~ 1). Cette acidité, même si elle est locale et transitoire (« pics d'acidité »), pose la question de savoir si elle peut favoriser / contribuer à la corrosion et à la dégradation des composants des réacteurs.

Mots clés : Eau supercritique (ESC); radiolyse; neutrons rapides; protons de recul; rendements (valeurs *G*); pH; « pic d'acidité »; simulations Monte Carlo de la chimie des trajectoires; réacteur à eau supercritique de Génération IV; corrosion.

*Auteur correspondant :
Jean-Paul Jay-Gerin (courriel : jean-paul.jay-gerin@USherbrooke.ca).

Journal canadien de chimie
Manuscrit n° cjc-2018-0505
Soumis : 27 novembre 2018
Corrections mineures demandées par les arbitres : 31 décembre 2018
Version révisée soumise : 5 janvier 2019, acceptée pour publication : 10 janvier 2019
Facteur d'impact : 1,084

4. ARTICLE

"Acid-spike" formation in the fast neutron radiolysis of supercritical water at 400 °C studied by Monte Carlo track chemistry simulations

by

Md Mohsin Patwary, Sunuchakan Sanguanmith, Jintana Meesungnoen, and Jean-Paul Jay-Gerin*

Département de médecine nucléaire et de radiobiologie, Faculté de médecine et de santé de la santé, Université de Sherbrooke, 3001, 12ème avenue Nord, Sherbrooke (Québec) J1H 5N4, Canada

ABSTRACT

A reliable understanding of radiolysis processes in supercritical water (SCW)-cooled reactors is required to ensure optimal water chemistry control. In this perspective, Monte Carlo track chemistry simulations of the radiolysis of pure, deaerated SCW at 400 °C by 2 MeV monoenergetic neutrons were carried out as a function of water density between 0.15-0.6 g/cm^3. The yields of hydronium ions (H_3O^+) formed at early time were obtained based on the *G*-values calculated for the first three generated recoil protons. Combining our calculated $G(H_3O^+)$ values with a cylindrical track model allowed us to estimate the concentrations of H_3O^+ and the corresponding pH values. An abrupt, transient, highly acidic pH response ("acid spikes") was observed at early times around the "native" fast neutron/recoil proton trajectories. This intra-track acidity was found to be strongest at times of less than a few tens to a hundred of picoseconds, depending on the value of the density considered (pH ~ 1). At longer times, the pH gradually increased for all densities, finally reaching a constant value corresponding to the non-radiolytic, pre-irradiation concentration of H_3O^+, due to the autoprotolysis of water. Interestingly, the lower the density of the water, the longer the time required to reach this constant value. Since many in-core processes in nuclear reactors critically depend on the pH, the present work raises the question whether such highly acidic pH fluctuations, though local and transitory, could promote/contribute to

corrosion and degradation of materials under proposed SCW-cooled reactor operating conditions.

Key words: Supercritical water (SCW); radiolysis; fast neutrons; recoil protons; H_3O^+ radiolytic yield (*G*-value); pH; acid spike; Monte Carlo track chemistry simulations; Generation IV SCW-cooled reactor; corrosion.

* Corresponding author:
Jean-Paul Jay-Gerin (*E-mail:* jean-paul.jay-gerin@USherbrooke.ca).

Canadian Journal of Chemistry
Submitted: November 27, 2018
Comments from referees received: December 31, 2018
Revised version submitted: January 5, 2019; accepted for publication: January 10, 2019
Impact factor: 1.084

1. Introduction

Supercritical water (SCW) (*i.e.*, water at temperatures and pressures above its thermodynamic critical point in the *P-V-T* diagram; for light water, H_2O: T_c = 373.95 °C, P_c = 22.06 MPa, and ρ_c = 0.322 g/cm^3) has been a subject of growing interest in recent decades. Besides its importance for fundamental scientific research, SCW has attracted attention for its important role in a variety of innovative technological and industrial applications.[1-5] Most of this attention is driven by the nature of SCW whose density can be varied continuously at constant temperature over a wide range from liquid-like to gas-like values with only small changes in applied pressure. This tunability of SCW densities with pressure provides access to a wide range of density-dependent water properties while avoiding the otherwise perturbing gas-to-liquid phase transition.

Among the most attractive applications in this area is the proposed next generation (Gen IV) SCW-cooled reactor (SCWR) concept to meet future global demand for electricity, hydrogen, and other products.[6-8] The future Gen IV SCWR is a promising advanced nuclear reactor system[5,9] with ~45% increased efficiency compared to ~28-32% for current conventional pressurized water reactors. The homogeneous supercritical phase also allows for more simple plant design and operation.

Before such technologies as the SCWR can be fully utilized, however, a thorough understanding of the SCW chemistry is required. In particular, one of the most significant challenges for water chemistry in SCWR designs is to predict, and if possible, mitigate the effects of water radiolysis on material performance and corrosion, as the reactors under consideration operate at core inlet and outlet temperatures of ~350 and 625 °C, respectively, at a pressure of 25 MPa.[5] Under such "extreme" irradiation conditions of high temperatures and pressures, the effect of an intense, mixed fast neutron/γ-radiation field passing through the reactor core results in the radiolytic formation of oxidizing species at high concentrations, such as $^{\bullet}OH$, H_2O_2, O_2 (produced

by decomposition of H_2O_2), and $O_2^{\bullet-}$ (or $HO_2^{\bullet}$, depending on the pH).[10,11] These species are highly reactive and can significantly increase the corrosion and degradation of structural materials both in the core and in the associated piping components of the reactor. Proper control of water chemistry, *e.g.*, adding a small concentration of excess H_2 to the reactor coolant, as with current pressurized high temperature water reactors, may be the key to maintaining the integrity of the reactors, although it is still unclear whether this strategy to suppress water radiolysis would also be effective under SCWR conditions.[5,11,12]

Direct measurements at very high temperatures and pressures, and especially beyond the critical point of water, are difficult to perform. Moreover, since Gen IV SCWRs are currently at the conceptual design stage, studies on water radiolysis in a SCWR have been laboratory-based rather than reactor-based. Consequently, experimental data on radiation chemistry and reaction kinetics of transients under the proposed SCWR operating conditions are very limited and significant gaps still exist.[5,13,14] Under these conditions, theoretical modeling and computer simulations are an important route of investigation for predicting the detailed radiation chemistry in a SCWR and the consequences for materials. Although a large body of data relevant to the radiolysis of water by γ-rays or high-energy (~1 MeV) electrons is readily available in the literature, the fast-neutron-induced water chemistry remains largely unknown for the proposed SCWR operating conditions.

Recently, Monte Carlo track chemistry simulations were used to calculate the yields (or *G* values) of hydronium ions (H_3O^+) at ambient as well as elevated temperatures, which formed in spurs/tracks of the low/high linear energy transfer (LET) radiolysis of pure, deaerated water during and shortly after irradiation.[15-17] Using simple, LET-dependent, spatio-temporal models of a spur or track, we found that the *in situ*, highly nonhomogeneous radiolytic formation of H_3O^+ temporarily renders the "native" spur/track regions more acidic than the surrounding medium. At 25 °C, an

abrupt transient acidic pH effect (which we termed an "acid spike") was observed to be greatest for times shorter than ~1 ns in an isolated "spherical" spur (characteristic of low-LET radiation, such as ^{60}Co γ/fast electron irradiation, LET ~ 0.3 keV/μm). In this time range, the pH remained almost constant at ~3.3. For an axially homogeneous "cylindrical" track (characteristic of high-LET radiation), the acid-spike response to ionizing radiation was much more intense than that for the spherical spur geometry. For example, for a 2.4-MeV incident helium ion (LET ~ 150 keV/μm), the pH was found to be about 0.5 on a time scale of ~100 ps. At longer times, the pH gradually increased for both low- and high-LET radiation types, ultimately reaching a constant value of seven (neutral pH at 25 °C) at ~1 μs for the spur model and ~0.1 ms for the track model.[15]

Interestingly, this early generation of a transient acid pH response around charged particle tracks was first highlighted in the late 1940's.[18,19] While several authors have shown evidence for this intra-track acidity experimentally,[20] these acid-spike effects have been largely ignored in water or in aqueous environments so far.[21] From a chemical point of view, this may be somewhat surprising in view of the potential implications of a local, albeit temporary increase in acidity on damage induction and corrosion in water-cooled reactors.

In this work, we extend our previous calculations to determine the yields of H_3O^+ resulting from the radiolysis of pure, deaerated SCW (H_2O) by mono-energetic 2 MeV incident neutrons at 400 °C as a function of water density (pressure) over the range of 0.15-0.6 g/cm^3 (~24-56 MPa). Our goal is to investigate whether these early acid-spike effects persist under SCW irradiation conditions, and then to determine their magnitude and time dependence. The 2 MeV energy of neutrons was considered to be representative of the average initial energy of a fast neutron flux in a reactor.[22] The chosen density range mimics the coolant conditions in the heat transport system of the SCWR. SCW acts like a "dense fluid" whose density can vary continuously with temperature/pressure from ~0.1-0.2 g/cm^3 (low-density or "gas-like" regime at the

reactor core outlet temperature) to higher values (~0.6-0.7 g/cm^3) similar to those of liquid water below the critical point (high-density or "liquid-like" regime near the reactor core inlet).[5]

2. Fast neutron interaction with water

"Fast" neutrons (*i.e.*, those with kinetic energies ranging from ~0.5-10 MeV) which concern us in this work, deposit their energy in the water through ion recoils; in H_2O, proton recoils absorb ~88% of the neutron energy while the remainder is absorbed by oxygen ions.[23] In this work, only the proton recoil component will be considered, as oxygen ion recoils are of minor importance for the fast neutron radiolysis of water due to their low average energies.[24,25] Moreover, these proton recoils have maximum ranges (*i.e.*, penetration depths) that are much smaller than the average distance between two successive neutron interactions. For example, the mean free path of a 2 MeV incident neutron in water at 25 °C is about 4 cm, while the maximum range of the proton recoil at this energy is ~75 μm.[24,26] Therefore, they can be considered as behaving *independently* of each other and, under normal irradiation conditions, their energy is deposited locally in isolated, dense tracks in the water, near the incident neutron collision sites (*i.e.*, the generation points of the recoils).

For the estimation of the radiation chemical yields due to 2 MeV neutrons, only the contributions of the *first three recoil protons* was considered in the present calculations, since further recoil protons generated by the neutron as it is further moderated do not contribute significantly to radiolysis due to their low average energies.[25,27,28] The *initial* proton energies (E_{p_i}, i = 1 to 3) are 1.264, 0.465, and 0.171 MeV.[25] The fast neutron yields were then calculated by summing the G values associated with each recoil proton considered (as determined by our Monte Carlo simulations; see *infra*), weighted by its fraction of total neutron energy deposited:[22,24,25]

$$G(\mathrm{X}) = \frac{\sum_{i=1}^{3} G(\mathrm{X})_{p_i} E_{p_i}}{E_T}, \quad (1)$$

where $G(\mathrm{X})_{p_i}$ is the yield of species X associated with the recoil proton p_i and

$$E_T = \sum_{i=1}^{3} E_{p_i} \quad (2)$$

is the sum of all recoil proton energies.

3. Monte Carlo track chemistry simulations

The entire sequence of events generated in the radiolysis of SCW at 400 °C by incident protons of various initial energies was modeled using an extended version[24,25,29] of our Monte Carlo track chemistry simulation code called IONLYS-IRT.[30] In short, the IONLYS step-by-step program is used to cover all the events of the early physical and physicochemical stages of radiation action up to ~1 ps in the track development in a 3-D geometrical environment. The complex, highly nonhomogeneous spatial distribution of the reactants formed at the end of the physicochemical stage [e_{aq}^- (hydrated electron), H^+ (or H_3O^+), OH^-, $H^\bullet$, H_2, $^\bullet OH$, H_2O_2, $O_2^{\bullet-}$ (or $HO_2^\bullet$), $^\bullet O^\bullet$, $O^{\bullet-}$, *etc*.][20,30,31] is then used directly as the starting point for the subsequent nonhomogeneous chemical stage. This third stage, in which the various radiolytic species diffuse randomly (at rates determined by their diffusion coefficients) and react with each other (or competitively with any dissolved solutes present in sufficient concentrations) until all spur/track processes are complete, is covered by our IRT program.[32] This program uses the "independent reaction times" (IRT) method,[32,33] a computationally efficient stochastic simulation technique that is used to simulate reaction times without having to follow the trajectories of the diffusing species. Its implementation has been reported previously[32] and its ability to provide accurate time-dependent chemical yields under different irradiation conditions has been well validated by comparison with complete random flights Monte Carlo simulations, which follow the reactant trajectories in

detail.[34] In addition, this IRT program can be used to efficiently describe the reactions that occur in the bulk solution during the homogeneous chemical stage, *i.e.*, in the time domain typically beyond some μs after the first ionization event.[35]

The current version of IONLYS-IRT has made various updates and modifications in the description of certain key parameters involved in the physicochemical and chemical stages of radiolysis. These changes are summarized as follows:

(i) We assumed that at 400 °C the thermalization distance (r_{th}) of "subexcitation-energy electrons" (e^-_{sub}) (those with kinetic energies lower than ~7.3 eV, the first-electronic excitation threshold in liquid water) is only affected by changes in the water density (ρ) and we scaled it according to a $(1/\rho)^{1/3}$ law,[36] namely,

$$(3) \qquad r_{th}\left(400\,^{\circ}\mathrm{C}, \rho\right) = r_{th}\left(400\,^{\circ}\mathrm{C}, 0.6\ \mathrm{g/cm^3}\right)\left[\frac{0.6\ \mathrm{g/cm^3}}{\rho}\right]^{1/3},$$

with $r_{th}\left(400\,^{\circ}\mathrm{C}, 0.6\ \mathrm{g/cm^3}\right) \approx 3.2\ \mathrm{nm}$.[37] This means that decreasing density further separates the water molecules but does not change their ability to interact with the energetic e^-_{sub}, resulting in an increase of r_{th}. The density dependence of r_{th} used in this work is shown in Fig. 1.

(ii) We included in the simulations a prompt geminate electron-cation ($H_2O^{\bullet+}$) recombination (*i.e.*, prior to thermalization of the e^-_{sub}) that decreased in irradiated SCW at 400 °C as the water density decreased from ~0.6 to 0.15 g/cm^3.[38]

(iii) We used the rate constants recently predicted by Liu *et al.*,[39,40] based on their so-called cage effect model which accounts for the non-Arrhenius temperature dependence of many reactions in water, for a number of reactions involved in the radiolysis of SCW at 400 °C. Given the lack of experimental data, this new database is important in providing us with recommendations for the best rate constant values to use at this time in modeling the radiolysis of SCW near and above the critical point. In some cases, we also used the chemical kinetic data compiled by Elliot and Bartels,[22]

simply extrapolated above their experimentally measured temperature ranges (mostly 20-350 °C), as well as the recent pulse radiolysis measurements by Muroya *et al.*[41] for the rate constant of the radiation-induced reaction:

(4) $H^{\bullet} + H_2O \rightarrow H_2 + {}^{\bullet}OH$,

a key reaction in high-temperature water radiolysis. In the absence of any other information, we chose to neglect any dependence of the reaction rate constants on water density for the 400 °C isotherm of interest. In the 0.15-0.6 g/cm^3 range studied here, this approximation does not appear to have a large impact, considering the relatively slowly varying k values for the few reactions whose rates have been measured as a function of SCW density.[42-44]

(iv) We have taken into account that due to their limited ranges all the recoil protons are completely stopped in the water. The chemistry measured under these conditions is an average over the proton energies from the initial proton energy to zero. To avoid complexity arising from the resulting variations in the energy of the moving protons, simulations were performed with the simplifying approximation that the energies of the three considered recoil protons remained constant when passing through the water medium. These constant track *average* energy values $\bar{E}_{p_i}$ (i = 1 to 3) were obtained according to a procedure described previously by Islam et al.[17] using the SRIM software[45] and our own Monte Carlo track structure simulations. They were found to be ~0.6, 0.3, and 0.17 MeV, respectively. Interestingly, these values varied only slightly (at most ~5%) as a function of water density over the studied range of 0.15-0.6 g/cm^3 and were therefore kept constant in all our chemical yield calculations.

The density dependences of the viscosity, static dielectric constant, and molar concentration of SCW at 400 °C used in this work were taken from the NIST Chemistry WebBook.[46] The values for the ionic product of water (K_w) were obtained from

Bandura and Lvov.[47] From a microscopic perspective, we ignored the heterogeneous character of the molecular structure of SCW[48] which is due to the presence of density fluctuations (or water "clustering") associated with criticality. In this study, we assumed that the overall instantaneous picture of SCW at 400 °C could simply be viewed as a *continuum* medium with a mean density equal to the density of bulk water (ρ).

All our calculations were performed by simulating short (typically, ~15-150 μm) proton track segments, over which the energy and LET of the recoil protons are well defined and remain nearly constant. Such model calculations thus gave "track segment" yields for a well-defined LET as a function of time. For the three recoil protons under consideration, whose track average energies are ~0.6, 0.3, and 0.17 MeV, respectively, the corresponding mean LET values increase from ~5.5, 8.2, and 10.4 keV/μm to ~22, 33, and 42 keV/μm when the SCW density is increased from 0.15 to 0.6 g/cm^3. With this LET range, the proton's track can be modeled as a cylinder, characteristic of high-LET radiation[15,17] (see *infra*). The number of individual proton "histories" (usually ~10-150, depending on the proton energy) was chosen to ensure only small statistical fluctuations in the computed averages of chemical yields, while meeting acceptable computer time limits.

Throughout this paper, *G*-values are quoted in units of molecules formed or consumed per 100 eV of radiation energy absorbed. For conversion into SI units, 1 molecule/100 eV = 0.10364 μmol/J.

4. Results and discussion

Figure 2 shows the variations of $G(H_3O^+)$ and $G(OH^-)$ calculated from our simulations of the radiolysis of pure, deaerated SCW (H_2O) at 400 °C by 2 MeV incident neutrons as a function of time from ~1 ps to 10 μs, for different water densities

in the range of 0.15-0.6 g/cm^3. Obviously, the hydroxide ion OH^-, which is formed largely by the reaction:

(5) $$e^-_{aq} + {}^\bullet OH \rightarrow OH^- \ ,$$

during the track stage of the radiolysis, contributes to an alkaline track and consequently counteracts the acid-spike effect discussed in this work. However, as can be seen from Fig. 2, $G(OH^-)$ remains much smaller than $G(H_3O^+)$ over the time range of interest, independent of the considered density. As a result, its effect modifies the quantitative features of the pH only slightly and can be ignored to a good approximation. To our knowledge, there are no experimental data in the literature at 400 °C with which to compare these temporal variations of $G(H_3O^+)$ or $G(OH^-)$ shown in Fig. 2.

The *in situ* formation of H_3O^+ by the generated recoil protons renders the "native" track regions acidic. A qualitative physical image, based on the spatial distribution of the various initial products formed across an ionizing track,[17-19] can be offered to explain the origin of this local and transitory acidity. Interestingly, there is indeed a *charge separation* that develops quickly between the more concentrated positive-ion (mainly H_3O^+ and $^\bullet OH$) core of the track and the negative ions (mainly OH^- and $H^\bullet$) in the surrounding medium, which are somewhat removed from the track. This charge separation is due to the faster motion and long penetration (or thermalization) range of the ejected secondary electrons,[37] which, once hydrated, are captured by the slowly moving $^\bullet OH$ and H_3O^+ to form OH^- and $H^\bullet$. As a result, it is easy to see that this charge separation and its associated local acidity will last until the *diffusion* of $^\bullet OH$ and H_3O^+ has brought these species to the remote positions then occupied by the e^-_{aq}.

As discussed previously,[15] the observed decrease of $G(H_3O^+)$ is predominantly due to H_3O^+ reacting with e^-_{aq} and with OH^-, according to:

(6) $$H_3O^+ + e^-_{aq} \rightarrow H^\bullet + H_2O$$

and

(7) $H_3O^+ + OH^- \rightarrow 2\,H_2O$.

Other reactions, such as $H_3O^+ + O^{\bullet -} \rightarrow {}^{\bullet}OH + H_2O$ and $H_3O^+ + HO_2^- \rightarrow H_2O_2 + H_2O$, also contribute to the decay of $G(H_3O^+)$, but only very weakly. This can be seen clearly in Figs. 3*a* and 3*b*, in which we show the time dependence of the cumulative yield variations $\Delta G(H_3O^+)$ for each of the reactions that contribute to the decay of $G(H_3O^+)$, calculated from our Monte Carlo simulations at 400 °C, for ρ = 0.15 and 0.6 g/cm^3, respectively, in the interval ~1 ps-10 μs.

The effect of density (pressure) on the yield of H_3O^+ shown in Fig. 2 can be understood as follows. As we lower the density in SCW, there are fewer water molecules to present a "barrier" or, in other words, a solvent *cage effect*.[49] This results in the increased cage escape of the various species originating from water dissociation, including H_3O^+, since the proximity condition that would allow them to combine or recombine is not favored. In contrast, these density effects work in the opposite direction in the high-density liquid-like region, where a large barrier of solvent is present. In this case, the caged radiolytic products are forced to remain as colliding neighbors within the proton track where they are formed, thus increasing the likelihood of combination/recombination reactions[38] and hence leading to a fast decrease of $G(H_3O^+)$. This is in agreement with what we see in Fig. 2 (see also Fig. 3).

To calculate the pH values prevailing in the fast neutron/recoil proton track regions, we estimated the radiolytically generated concentrations of H_3O^+ in these regions as a function of time using a cylindrical track model, characteristic of high-LET radiation.[15] For each of the three considered recoil protons, we assumed the proton's track as an axially homogeneous cylinder, with a length L = 1 μm and initial radius r_c equal to the radius of the physical track "core" (corresponding to the tiny radial region within the first few nanometers around the impacting proton path, at ~10^{-13} s).[15,17,50,51]

In this case, for the generated recoil proton p_i (i = 1 to 3), the track concentration of radiolytically generated H_3O^+ can be derived from[15,30]

$$(8) \qquad \left[H_3O^+\right]_{p_i,\text{radiolytic}}(t) = G\left(H_3O^+\right)_{p_i}(t)\left[\frac{(\text{LET})_{p_i}}{\pi\, r(t)^2}\right],$$

where

$$(9) \qquad r(t)^2 = r_c^2 + 4D\left(H_3O^+\right)t$$

is the change with time of r_c due to the 2-D diffusive expansion of the track. Here, t is time, D is the diffusion coefficient for H_3O^+ in water, and r_c was estimated directly from our simulations. We assumed r_c = 2 nm for all recoil protons and all considered densities. For $D(H_3O^+)$, which is essentially unknown at 400 °C, we first extrapolated the data reported by Elliot and Bartels[22] over the 20-350 °C temperature range, and then assumed that its dependence on density equaled that of the self-diffusion coefficient of compressed SCW at 400 °C.[52] The variation of $D(H_3O^+)$ in SCW at 400 °C as a function of density used in this work is shown in Fig. 4.

Finally, the total concentration of H_3O^+ is the sum of $[H_3O^+]_{\text{radiolytic}}$, which simply results from the average of $\left[H_3O^+\right]_{p_i,\text{radiolytic}}$ for the three generated recoil protons, and the non-radiolytic, pre-irradiation concentration $\left[H_3O^+\right]_{\text{autoprotolysis}}$ that results from the autoprotolysis of water:[16,17,47]

$$(10) \qquad \left[H_3O^+\right]_{\text{total}}(t) = \left[H_3O^+\right]_{\text{radiolytic}}(t) + \left[H_3O^+\right]_{\text{autoprotolysis}}.$$

The pH in the corresponding track regions is then given by the negative logarithm (to the base 10) of $\left[H_3O^+\right]_{\text{total}}$:

$$(11) \qquad \text{pH}(t) = -\log\left\{\left[H_3O^+\right]_{\text{total}}(t)\right\}.$$

The temporal evolution of the pH values calculated from eqs. (8)-(11) for 2-MeV irradiating neutrons in pure, deaerated SCW (H_2O) at 400 °C is shown in Fig. 5 for different water densities ranging from 0.15-0.6 g/cm^3. As shown, for all densities considered, there is an abrupt, temporary and *highly acidic* pH effect at the beginning of the chemical stage. This "acid-spike" effect is *strongest* at times of less than a few tens to a hundred of picoseconds, depending on the value of the density considered. In this time range, the pH remains nearly constant, around *unity*. Over ~100 ps, the pH gradually increases over time. Ultimately, it reaches a constant value (pH of the body of the solution) equal to $-\log\left(\left[H_3O^+\right]_{\text{autoprotolysis}}\right)$, which depends on the density.[47] As can be seen from Fig. 5, the lower the density of the water, the longer the time required to reach this constant value, ranging from ~0.1 μs at 0.6 g/cm^3 (pH ~ 5.6) to more than 100 μs at 0.15 g/cm^3 (pH ~ 8.6).

Most interestingly, regardless of the SCW density considered, we see from Fig. 5 that the early acid pH conditions surrounding the "native" fast neutron/recoil proton trajectories persist for a period of more than six orders of magnitude. Rather surprisingly, the generation of such an early acid response around charged particle tracks has largely gone unnoticed in water or in aqueous environments subject to high-LET radiation, either at ambient or at elevated temperatures. Since many in-core processes in nuclear reactors, and in particular in proposed SCWRs, critically depend on the pH, a key water chemistry parameter,[5] the present work raises the question whether such abrupt, highly acidic pH variations, which extend spatially about tens of nanometers, could promote/contribute to material corrosion and damage. Since corrosion is a surface phenomenon, this can easily be envisioned, for example, when fast neutron/recoil proton tracks are formed in the immediate vicinity of a metal/water interface. The presence of H_3O^+ in contact with structural materials may readily induce spontaneous electrochemical reactions, which may release positive metal ions at the metal surface, thus creating a corrosive environment.[5,53,54] The continuous release of

these ions from a certain location may actually cause a "stress corrosion cracking" (SCC) site after years.[55] Perhaps more importantly, once the crack is developed, radiolysis in the crack and the resulting "acid spikes" could greatly speed up the SCC process.

In this regard, this work should stimulate novel predictive modeling of corrosion driven by these local, density-dependent acid-spike effects, which can then be tested with new measurements under SCWR conditions.

5. Summary and conclusion

In this work, Monte Carlo track chemistry simulations were used to calculate the yields of H_3O^+ formed early on in the radiolysis of pure, deaerated SCW by 2 MeV incident neutrons at 400 °C for different water densities in the range of 0.15-0.6 g/cm^3, chosen to mimic the coolant conditions in the heat transport system of proposed SCWRs. The fast neutron $G(H_3O^+)$ values were obtained by assuming that the most significant contribution to radiolysis comes from the first three recoil protons generated by the passage of the irradiating neutron. The concentrations of H_3O^+ and the corresponding pH values for these three recoil protons were then obtained from our calculated $G(H_3O^+)$ values using an axially homogeneous cylindrical track model. An abrupt, transient, highly acidic pH response was observed at early times around the "native" fast neutron/recoil proton trajectories. The magnitude and duration of this *in situ* "acid-spike" effect were found to be sensitive functions of the water density. At 400 °C and at times less than ~10 ps, the pH for the highest ("liquid-like") and lowest ("gas-like") densities considered, was around 0.8 and 1.3, respectively. At longer times, the pH gradually increased for all densities, and finally reached a constant value corresponding to the non-radiolytic, pre-irradiation concentration of H_3O^+, due to the autoprotolysis of water at ~0.1-100 μs following irradiation.

In conclusion, the question arises whether the strong intra-track acidity described here, while local and transitory, can trigger chemically aggressive conditions on metal surfaces, promoting the corrosion and degradation of materials in water-cooled nuclear reactors as well as in proposed SCWRs. As far as we know, the generation of such acidic pH spikes in water subject to the action of high-LET radiation, at both ambient and elevated temperatures including under SCW conditions, has never been mentioned before.

Acknowledgements

Md M.P. is the recipient of a scholarship from the Faculty of Medicine and Health Sciences of the Université de Sherbrooke. Thanks are due to Dr. David Guzonas and Dr. Craig R. Stuart (Canadian Nuclear Laboratories, Chalk River, Ontario) for stimulating correspondence and for their continued encouragement. J.-P.J.-G. is grateful to the Natural Sciences and Engineering Research Council of Canada (NSERC) for its financial support (Grant No. RGPIN-2015-06100).

References

(1) Galkin, A. A.; Lunin, V. V. *Russ. Chem. Rev.* **2005**, *74*, 21.

(2) Akiya, N.; Savage, P. E. *Chem. Rev.* **2002**, *102*, 2725.

(3) Tester, J. W.; Holgate, H. R.; Armellini, F. J.; Webley, P. A.; Killilea, W. R.; Hong, G. T.; Barner, H. E. In *Emerging Technologies in Hazardous Waste Management III*; Tedder, D. W., Pohland, F. G., Eds.; ACS Symposium Ser. No. 518; American Chemical Society: Washington, D.C., 1993, Ch. 3, pp. 35-76.

(4) *Supercritical Water: A Green Solvent: Properties and Uses*; Marcus, Y., Ed.; Wiley: Hoboken, NJ, 2012.

(5) Guzonas, D.; Novotny, R.; Penttilä, S.; Toivonen, A.; Zheng, W. *Materials and Water Chemistry for Supercritical Water-cooled Reactors*; Woodhead Publishing (Elsevier): Duxford, UK, 2018.

(6) Oka, Y.; Koshizuka, S. *Prog. Nucl. Energy* **1998**, *32*, 163.

(7) Schulenberg, T.; Leung, L. K. H.; Oka, Y. *Prog. Nucl. Energy* **2014**, *77*, 282.

(8) Duffey, R. *CNL Nucl. Rev.* **2016**, *5*, 181.

(9) *A Technology Roadmap for Generation IV Nuclear Energy Systems*. Report GIF-002-00; U.S. Department of Energy (DOE) Nuclear Energy Research Advisory Committee and the Generation IV International Forum: Washington, D.C., 2002.

(10) Guzonas, D.; Brosseau, F.; Tremaine, P.; Meesungnoen, J.; Jay-Gerin, J.-P. *Nucl. Technol.* **2012**, *179*, 205.

(11) Wang, M. Y.; Yeh, T.-K.; Liu, H.-M.; Lee, M. *Nucl. Sci. Eng.* **2013**, *174*, 179.

(12) Bartels, D. M.; Jonah, C.; Edwards, E.; Janik, D.; Haygarth, K.; Sims, H.; Marin, T.; Takahashi, K.; Janik, I.; Kanjara, K. *Proceedings of the 8th International Radiolysis, Electrochemistry and Materials Performance Workshop*, Quebec City, QC, October 8, 2010.

(13) Guzonas, D.; Stuart, C. R.; Jay-Gerin, J.-P.; Meesungnoen, J. *Testing Requirements for SCWR Radiolysis*. Report AECL No. 153-127160-REPT-001; Atomic Energy of Canada Ltd.: Mississauga, ON, 2010.

(14) Guzonas, D.; Cook, W. G. *Corros. Sci.* **2012**, *65*, 48.

(15) Kanike, V.; Meesungnoen, J.; Jay-Gerin, J.-P. *RSC Adv.* **2015**, *5*, 43361.

(16) Kanike, V.; Meesungnoen, J.; Sanguanmith, S.; Guzonas, D.; Stuart, C. R.; Jay-Gerin, J.-P. *CNL Nucl. Rev.* **2017**, *6*, 31.

(17) Islam, M. M.; Kanike, K.; Meesungnoen, J.; Lertnaisat, P.; Katsumura, Y.; Jay-Gerin, J.-P. *Chem. Phys. Lett.* **2018**, *693*, 210.

(18) Lea, D. E. *Actions of Radiations on Living Cells*; Cambridge University Press: Cambridge, UK, 1946, Ch. 2.

(19) Morrison, P. In *Symposium on Radiobiology: The Basic Aspects of Radiation Effects on Living Systems (June 14-18, 1950)*; Nickson, J. J., Ed.; Wiley: New York, NY, 1952, pp. 1-12.

(20) Spinks, J. W. T.; Woods, R. J. *An Introduction to Radiation Chemistry*, 3rd ed.; Wiley: New York, NY, 1990.

(21) Byakov, V. M.; Stepanov, S. V. *Phys.-Usp.* **2006**, *49*, 469.

(22) Elliot, A. J.; Bartels, D. M. *The Reaction Set, Rate Constants and g-Values for the Simulation of the Radiolysis of Light Water over the Range 20° to 350 °C Based on Information Available in 2008*; Report AECL No. 153-127160-450-001; Atomic Energy of Canada Ltd.: Chalk River, ON, 2009.

(23) Edwards, E. J.; Wilson, P. P. H.; Anderson, M. H.; Mezyk, S. P.; Pimblott, S. M.; Bartels, D. M. *Rev. Sci. Instrum.* **2007**, *78*, 124101.

(24) Tippayamontri, T.; Sanguanmith, S.; Meesungnoen, J.; Sunaryo, G. R.; Jay-Gerin, J.-P. *Recent Res. Devel. Physical Chem.* **2009**, *10*, 143.

(25) Butarbutar, S. L.; Meesungnoen, J.; Guzonas, D.; Stuart, C. R.; Jay-Gerin, J.-P. *Radiat. Res.* **2014**, *182*, 695.

(26) Watt, D. E. *Quantities for Dosimetry of Ionizing Radiations in Liquid Water*; Taylor & Francis: London, UK, 1996.

(27) Gordon, S.; Schmidt, K. H.; Honekamp, J. R. *Radiat. Phys. Chem.* **1983**, *21*, 247.

(28) Swiatla-Wojcik, D.; Buxton, G. V. *J. Chem. Soc. Faraday Trans.* **1998**, *94*, 2135.

(29) Sanguanmith, S.; Meesungnoen, J.; Guzonas, D.; Stuart, C. R.; Jay-Gerin, J.-P. *J. Nucl. Eng. Radiat. Sci.* **2016**, *2*, 021014.

(30) Meesungnoen, J.; Jay-Gerin, J.-P. In *Charged Particle and Photon Interactions with Matter: Recent Advances, Applications, and Interfaces*; Hatano, Y., Katsumura, Y., Mozumder, A., Eds.; Taylor & Francis: Boca Raton, FL, 2011; pp. 355-400.

(31) Ferradini, C.; Jay-Gerin, J.-P. *Can. J. Chem.* **1999**, *77*, 1542.

(32) Frongillo, Y.; Goulet, T.; Fraser, M.-J.; Cobut, V.; Patau, J. P.; Jay-Gerin, J.-P. *Radiat. Phys. Chem.* **1998**, *51*, 245.

(33) Pimblott, S. M.; Pilling, M. J.; Green, N. J. B. *Radiat. Phys. Chem.* **1991**, *37*, 377.

(34) Plante, I. Ph.D. Thesis, Université de Sherbrooke, Sherbrooke, QC, 2009.

(35) Sanguanmith, S.; Meesungnoen, J.; Jay-Gerin, J.-P. *Phys. Chem. Chem. Phys.* **2012**, *14*, 11277.

(36) Swiatla-Wojcik, D.; Buxton, G. V. *J. Phys. Chem.* **1995**, *99*, 11464.

(37) Muroya, Y.; Sanguanmith, S.; Meesungnoen, J.; Lin, M.; Yan, Y.; Katsumura, Y.; Jay-Gerin, J.-P. *Phys. Chem. Chem. Phys.* **2012**, *14*, 14325.

(38) Meesungnoen, J.; Sanguanmith, S.; Jay-Gerin, J.-P. *Phys. Chem. Chem. Phys.* **2013**, *15*, 16450.

(39) Liu, G.; Du, T.; Toth, L.; Beninger, J.; Ghandi, K. *CNL Nucl. Rev.* **2016**, *5*, 345.

(40) Liu, G.; Landry, C.; Ghandi, K. *Can. J. Chem.* **2018**, *96*, 267.

(41) Muroya, Y.; Yamashita, S.; Lertnaisat, P.; Sanguanmith, S.; Meesungnoen, J.; Jay-Gerin, J.-P.; Katsumura, Y. *Phys. Chem. Chem. Phys.* **2017**, *19*, 30834.

(42) Alcorn, C. D.; Brodovitch, J.-C.; Percival, P. W.; Smith, M.; Ghandi, K. *Chem. Phys.* **2014**, *435*, 29.

(43) Lin, M.; Katsumura, Y. In *Charged Particle and Photon Interactions with Matter: Recent Advances, Applications, and Interfaces*; Hatano, Y., Katsumura, Y., Mozumder, A., Eds.; Taylor & Francis: Boca Raton, FL, 2011; pp. 401-424.

(44) Cline, J.; Takahashi, K.; Marin, T. W.; Jonah, C. D.; Bartels, D. M. *J. Phys. Chem. A* **2002**, *106*, 12260.

(45) Ziegler, J. F.; Bierdack, J. P.; Ziegler, M. D. *SRIM - The Stopping and Range of Ions in Matter*; SRIM Co.: Chester, MD, 2015.

(46) *NIST Chemistry WebBook, NIST Standard Reference Database No. 69*; Linstrom, P. J., Mallard, W. G., Eds.; National Institute of Standards and Technology: Gaithersburg, MD. Available at: http://www.webbook.nist.gov.

(47) Bandura, A. V.; Lvov, S. N. *J. Phys. Chem. Ref. Data* **2006**, *35*, 15.

(48) Metatla, N.; Lafond, F.; Jay-Gerin, J.-P.; Soldera, A. *RSC Adv.* **2016**, *6*, 30484.

(49) Franck, J.; Rabinowitsch, E. *Trans. Faraday Soc.* **1934**, *30*, 120.

(50) Magee, J. L.; Chatterjee, A. In *Kinetics of Nonhomogeneous Processes*; Freeman, G. R., Ed.; Wiley: New York, NY, 1987, pp. 171-214.

(51) Mozumder, A. *Fundamentals of Radiation Chemistry*; Academic Press: San Diego, CA, 1999.

(52) Lamb, W. J.; Hoffman, G. A.; Jonas, J. *J. Chem. Phys.* **1981**, *74*, 6875.

(53) Kim, H.; Mitton, D. B.; Latanision, R. M. *J. Electrochem. Soc.* **2010**, *157*, C194.

(54) *Corrosion Issues in Light Water Reactors: Stress Corrosion Cracking*; Féron, D., Olive, J.-M., Eds.; Woodhead Publishing Limited: Cambridge, UK, 2007.

(55) Peng, Q.; Li, G.; Shoji, T. *J. Nucl. Sci. Technol.* **2003**, *40*, 397.

Figure captions

Figure 1: Variation of the thermalization distance r_{th} (in Å) of subexcitation electrons in pure, deaerated SCW at 400 °C as a function of water density in the range of ~0.1-0.7 g/cm^3 used in this work.

Figure 2: Temporal evolution of the yields (in molecule per 100 eV) of radiolytically produced H_3O^+ (solid lines) and OH^- (dashed lines) ions obtained from our Monte Carlo simulations of the radiolysis of pure, deaerated SCW by 2 MeV incident neutrons in the interval of ~1 ps to 10 μs, for six different water densities: 0.15 (black), 0.2 (orange), 0.3 (olive), 0.4 (blue), 0.5 (green), and 0.6 (red) g/cm^3 at 400 °C. Calculations are based on the radiation effects in 0.6, 0.3, and 0.17 MeV recoil proton tracks (see text).

Figure 3: Time dependence of the extents $\Delta G(H_3O^+)$ (in molecule per 100 eV) of the different reactions that are involved in the decay of H_3O^+, obtained from our Monte Carlo simulations of the radiolysis of pure, deaerated SCW by 2 MeV incident neutrons in the interval of ~1 ps to 10 μs, for $\rho = 0.15$ (panel *a*) and $\rho = 0.6$ (panel *b*) g/cm^3 at 400 °C.

Figure 4: Variation of the diffusion coefficient (in m^2/s) for the hydronium ion, $D(H_3O^+)$, in SCW at 400 °C as a function of water density in the range of ~0.1-0.7 g/cm^3 used in this work (see text).

Figure 5: Temporal evolution of the pH prevailing in the track regions of 2 MeV irradiating neutrons calculated for pure, deaerated SCW at 400 °C in the interval of ~1 ps to 10 μs for the same six water densities as in Fig. 2 (see text). For the sake of comparison, the dashed lines show, for $\rho = 0.15$ (black) and 0.6 (red) g/cm^3, the variation of pH with time in an isolated spherical "spur" (characteristic of low-LET radiation) (see Kanike et al.[15,16])

as calculated for irradiating 300 MeV protons (which mimic ^{60}Co γ/fast electron irradiation; LET ~ 0.3 keV/μm) using an initial spur radius (taken here as equal to r_{th}; see Fig. 1) of 42.2 and 32 Å for the two water densities considered.

FIG. 1

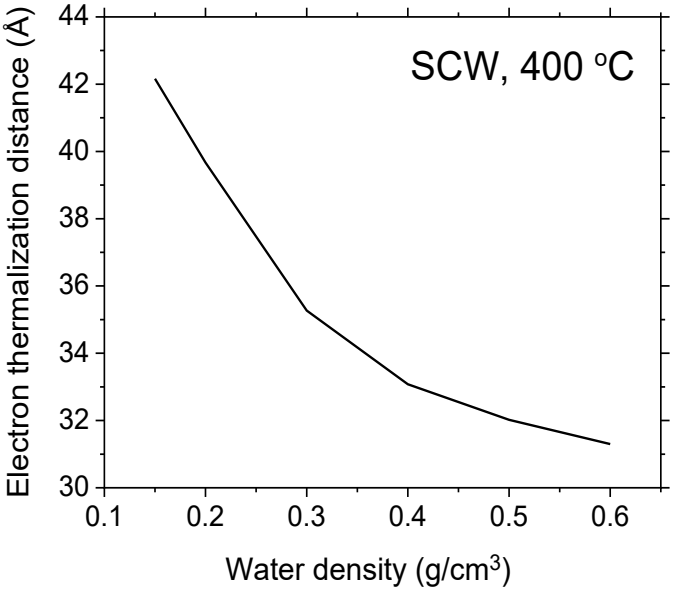
SCW, 400 °C
Electron thermalization distance (Å)
Water density (g/cm3)
44
42
40
38
36
34
32
30
0.1
0.2
0.3
0.4
0.5
0.6

FIG. 2

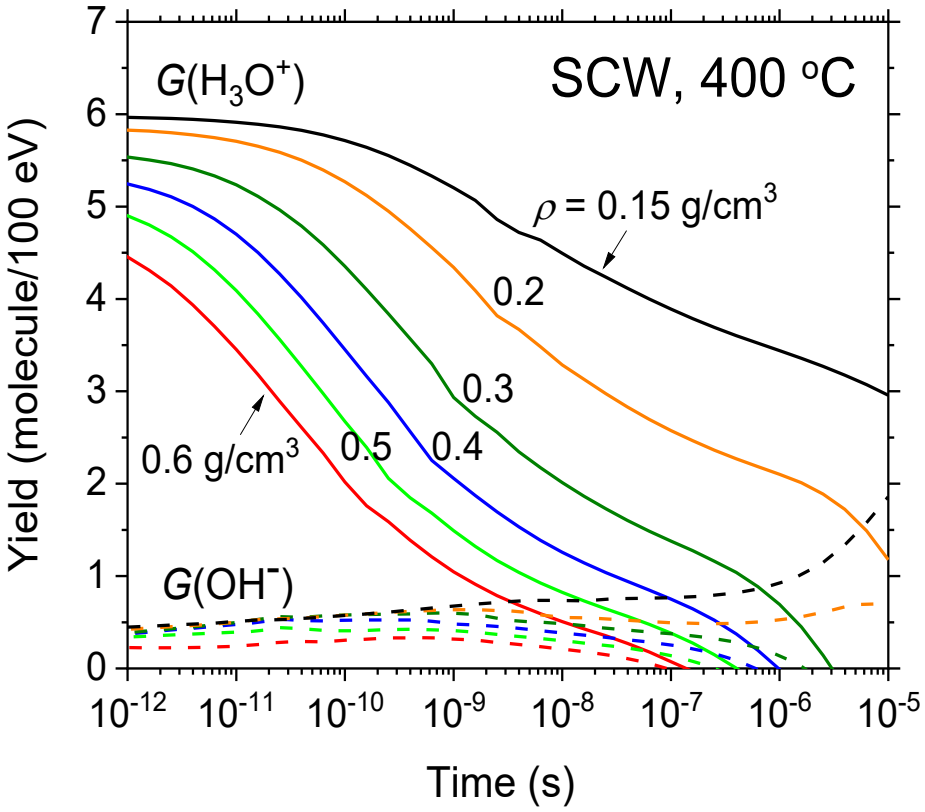
G(H3O+)
SCW, 400 oC
ρ = 0.15 g/cm3
0.2
0.3
0.4
0.5
0.6 g/cm3
G(OH-)
Yield (molecule/100 eV)
Time (s)
0
1
2
3
4
5
6
7
10-12
10-11
10-10
10-9
10-8
10-7
10-6
10-5

FIG. 3

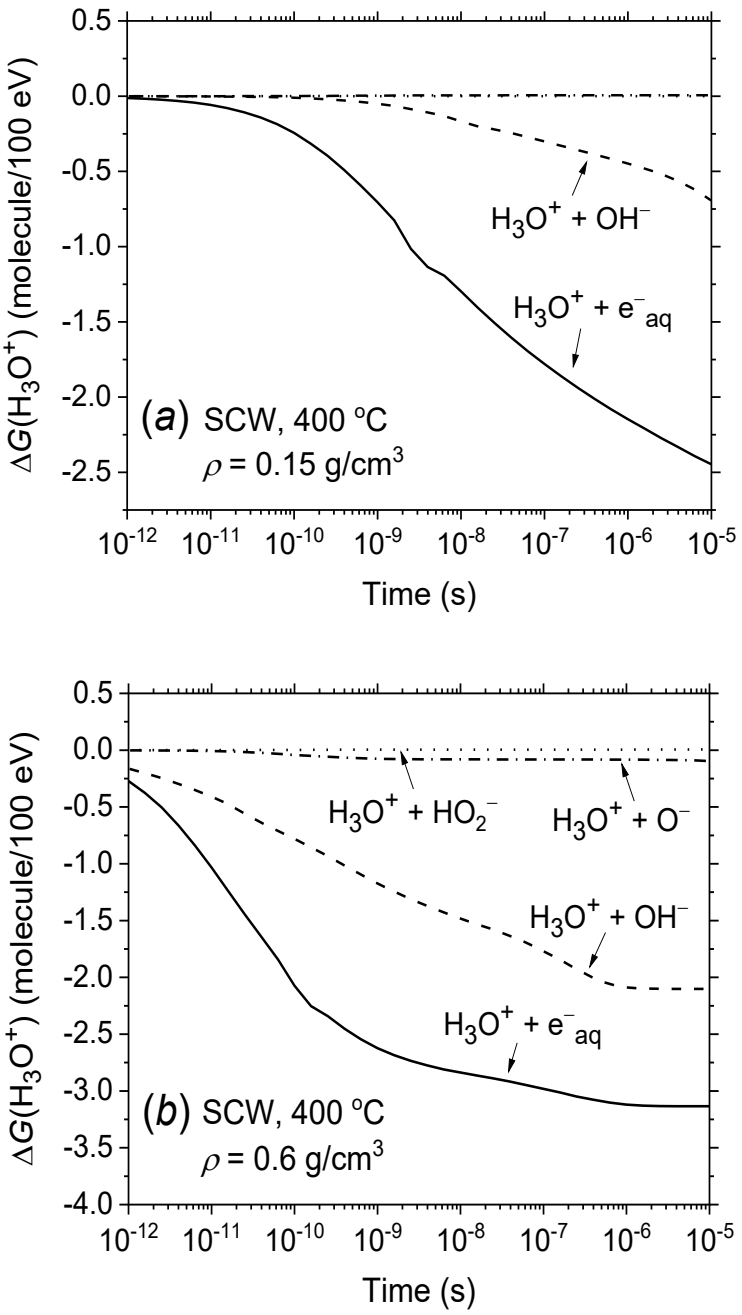
0.5
0.0
-0.5
-1.0
-1.5
-2.0
-2.5
ΔG(H3O+) (molecule/100 eV)
H3O+ + OH−
H3O+ + e−aq
(a) SCW, 400 °C
ρ = 0.15 g/cm3
10-12 10-11 10-10 10-9 10-8 10-7 10-6 10-5
Time (s)
0.5
0.0
-0.5
-1.0
-1.5
-2.0
-2.5
-3.0
-3.5
-4.0
ΔG(H3O+) (molecule/100 eV)
H3O+ + HO2−
H3O+ + O−
H3O+ + OH−
H3O+ + e−aq
(b) SCW, 400 °C
ρ = 0.6 g/cm3
10-12 10-11 10-10 10-9 10-8 10-7 10-6 10-5
Time (s)

FIG. 4

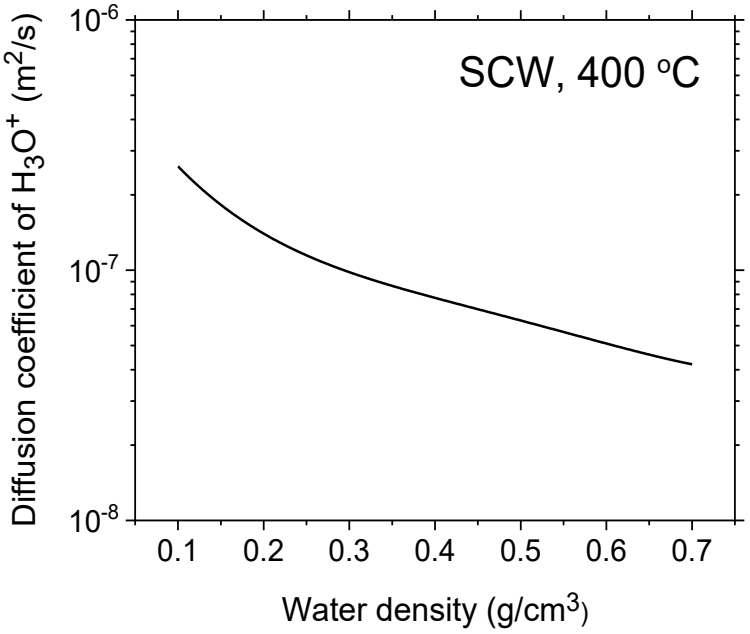
SCW, 400 °C
Diffusion coefficient of H_3O^+ (m^2/s)
10^{-6}
10^{-7}
10^{-8}
0.1
0.2
0.3
0.4
0.5
0.6
0.7
Water density (g/cm^3)

FIG. 5

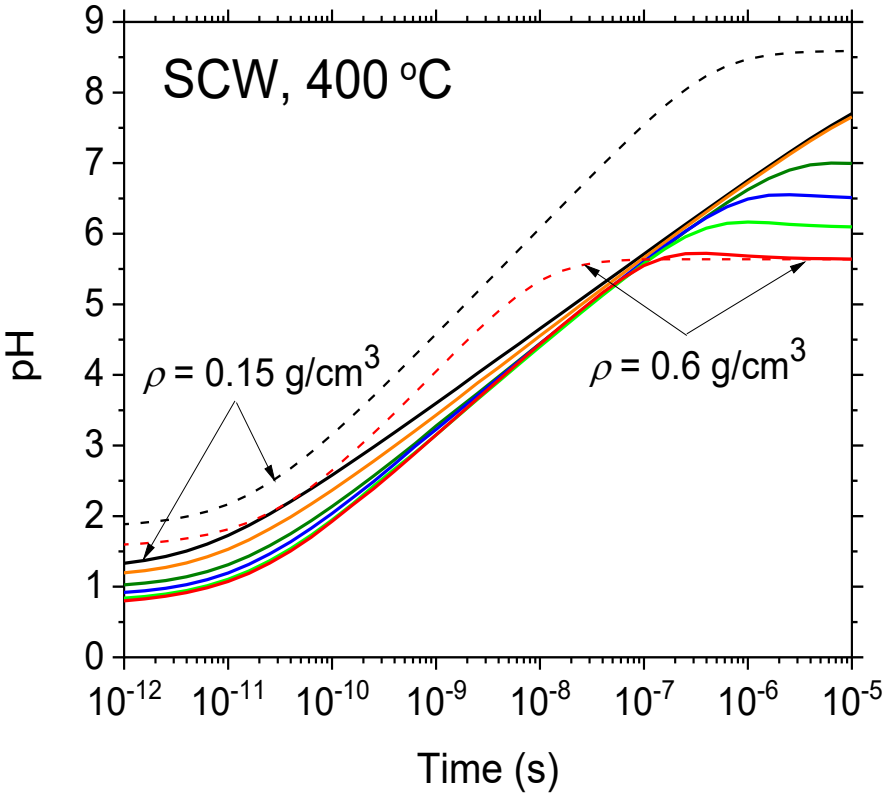
SCW, 400 °C
pH
Time (s)
ρ = 0.15 g/cm3
ρ = 0.6 g/cm3
0
1
2
3
4
5
6
7
8
9
10-12
10-11
10-10
10-9
10-8
10-7
10-6
10-5

5. DISCUSSION

5.1 Comparability of our program

The Monte Carlo simulation program used in this work for the radiolysis of SCW (at 400 °C) is an extension of the program originally developed for liquid water at 25 °C and later at elevated temperatures up to 350 °C by our group at the Université de Sherbrooke. All available information on the reactivities and diffusion coefficients of the various species produced by radiolysis and on the physicochemical properties (density, viscosity, static dielectric constant, *etc.*) of water in its supercritical regime was incorporated into the calculations in order to account as precisely as possible for these particular thermodynamic conditions (see *supra*). The program was then validated by comparing the results of the calculations with existing experimental data (Meesungnoen et al., 2010, 2013; Butarbutar et al., 2014*a*; Sanguanmith et al., 2016).

As an example, Figure 5.1 shows the variation of LET with the energy of incident protons for different water densities at 400 °C, obtained by both our Monte Carlo track structure program and the SRIM ("Stopping Range of Ions in Matter") software. As we can see, our Monte Carlo simulations agree very well with the SRIM simulation results. Although a temperature of 400 °C is not achievable with SRIM, the density can be varied up to any level and density finally appears as the most important parameter to represent the distribution of water molecules along simulated ion trajectories. This figure indicates that the extended version of our program can successfully simulate energy-loss events and the effects of SCW density in the early physical stage of radiolysis.

Currently, only very limited experimental data are available on the radiation chemistry and reaction kinetics of transients under supercritical conditions. In fact, the only experimental data that allowed us to validate our Monte Carlo track chemistry program as a whole are the yields of e^-_{aq} in the low-LET radiolysis of SCW (D_2O) at 400 °C as a function of the density of water, measured directly by picosecond electron pulse radiolysis or deduced from scavenger experiments (Muroya et al., 2012). A good agreement was indeed found between the calculated $G(e^-_{aq})$ values and the experimental

data at ~60 ps and 1 ns, provided that a prompt geminate electron-cation ($H_2O^{\bullet+}$) recombination decreasing as the density decreases is incorporated into the simulations (Meesungnoen et al., 2013; Sanguanmith et al., 2016).

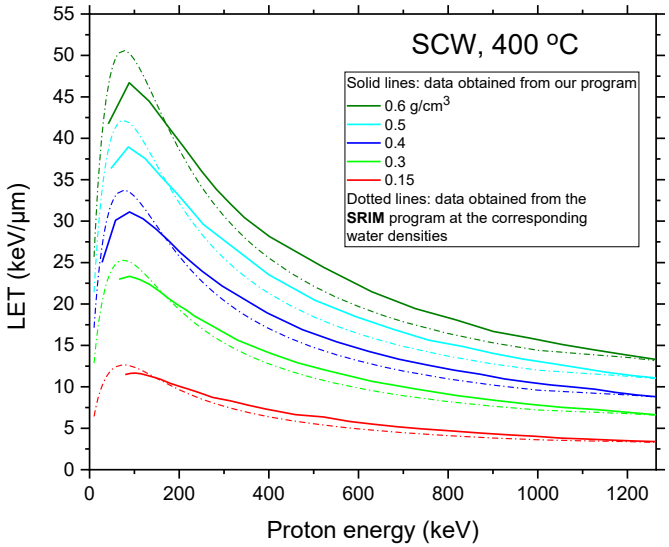

Figure 5.1 – Plot of LET against proton energy for an incident proton beam passing through SCW of different densities ranging from 0.15 to 0.6 g/cm^3, at 400 °C (solid lines). The results are compared with those obtained with the SRIM program (dashed lines).

In the first simulations of the radiolysis of SCW at 400 °C carried out by our group, the (average) "electron thermalization distance" (r_{th}) was kept constant – regardless the value of the density – at ~3 nm, a value determined at 350 °C from an analysis of the spur decay kinetics of e^-_{aq} at elevated temperatures (Muroya et al., 2012). In this work, we modified the last version of our program to include an increase in r_{th} when the density of the water decreases. More specifically, we assumed that at 400 °C the thermalization distance of "subexcitation-energy electrons" (e^-_{sub}) is only affected by changes in the water density (ρ) and we scaled it according to a $(1/\rho)^{1/3}$ law (Swiatla-Wojcik and Buxton, 1995), namely,

$$r_{th}\left(400\,^{\circ}\mathrm{C}, \rho\right) = r_{th}\left(400\,^{\circ}\mathrm{C}, 0.6\ \mathrm{g/cm^3}\right)\left[\frac{0.6\ \mathrm{g/cm^3}}{\rho}\right]^{1/3}, \qquad (5.a)$$

with $r_{th}\left(400\,^{\circ}\mathrm{C}, 0.6\ \mathrm{g/cm^3}\right) \approx 3.2\ \mathrm{nm}$. This means that decreasing density further

separates the water molecules but does not change their ability to interact with the energetic e^-_{sub}, resulting in an increase of r_{th} (Fig. 5.2).

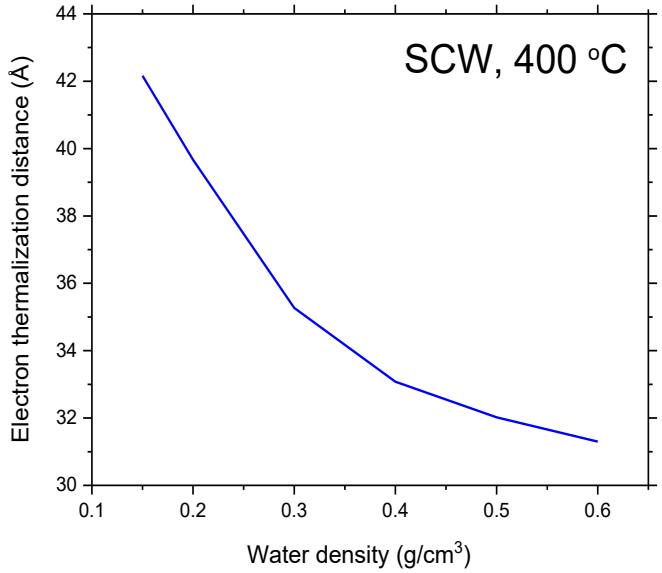

Figure 5.2 – Variation of the electron thermalization distance r_{th} (in Å) with the density of water ρ (in g/cm^3) used in this work.

It is difficult to estimate to what extent the density of water at the temperature of interest here can affect the electron thermalization distances. In their early work on the subject, Meesungnoen et al. (2013) showed that "r_{th} did not seem to play any major role" in explaining the experimentally observed density-dependent yields of hydrated electrons in irradiated SCW at 400 °C at short times (Muroya et al., 2010, 2012). Here we confirm these results, Fig. 5.3 showing that our simulated e^-_{aq} yields – by keeping r_{th} constant with water density or using a law in $(1/\rho)^{1/3}$ – are almost insensitive to the choice of r_{th} as a function of density.

5.2 Absorbed dose-average LET and energy in high-temperature water radiolysis: A new computational approach

The concept of "absorbed dose-average" LET becomes more important when the ion beam radiation has a limited range. In this case, the change in ion energy and LET is non-negligible as a function of penetration depth in the absorber. As a result, the concept of average constant energy for the whole track length (*i.e.*, "track-average"

energy or LET) becomes less accurate. Under these circumstances, the use of the *absorbed dose-average LET* (alternatively, "energy average") is more appropriate as it takes into account the distribution of energy deposited by the ionizing particle in the medium it traverses.

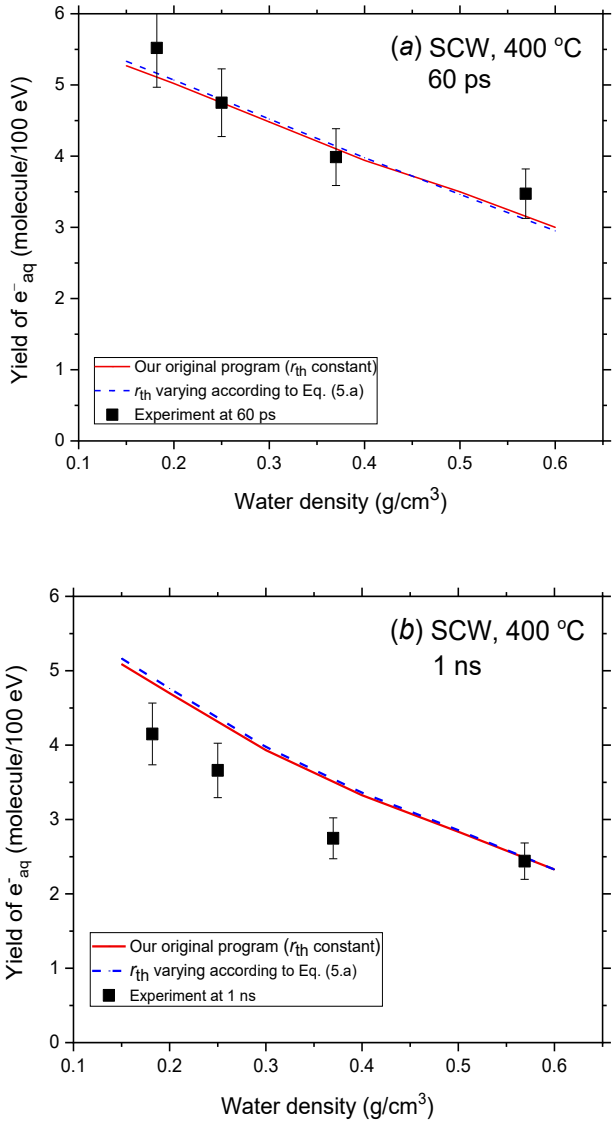

Figure 5.3 – Density dependence of the yields of e^-_{aq} in SCW at 400 °C, measured directly by ps-pulse radiolysis experiments (in D_2O) at ~60 ps (Panel *a*) and 1 ns (Panel *b*) after the ionizing event (■, estimated uncertainty of ±10%) (Muroya et al., 2010, 2012). The solid (red) and dashed (blue) lines show our Monte Carlo simulated results obtained with 300 MeV irradiating protons when r_{th} is kept constant (~3 nm) for all water densities and when r_{th} varies in $(1/\rho)^{1/3}$ according to Eq. (5.a) (Fig. 5.2).

Since this quantity more realistically represents the high "local" energy deposition densities that can occur in a track, even for low-LET radiation, it can therefore assume values higher than those corresponding to the track-averaged LET (ICRU Report 16, 1970; Watt, 1996). In the present work, we focussed on the absorbed dose-average LET, since all recoil protons generated in the fast neutron slowing-down process are stopped completely in the water, causing important variations in their energy and LET along their trajectories. In this regard, we have basically adopted the same strategy as that used previously by Butarbutar et al. (2014*a*). Instead of employing the initial values of the various proton parameters, we used their whole track absorbed dose-average values, as given in the compilation of ionizing radiation dosimetry data of Watt (1996). Watt's compilation is indeed an excellent reference for determining the dose-average energy for a variety of ions at different energies. However, this reference is limited to ambient temperature and does not take into account changes in temperature and density. We consider here SCW at 400 °C as a function of water density in the range of ~0.15-0.6 g/cm^3 irradiated by low-energy (1.264, 0.465, and 0.171 MeV) recoil protons. Therefore, we needed to calculate the dose-average energy under these specific conditions using a new computational approach. This was done with IONLYS, our Monte Carlo track structure program, according to the following procedure.

We first calculated the energy deposited by an incident proton of a given initial energy E_o in a *thin* (typically, 1 or 2 μm) layer of the absorbing material (SCW at 400 °C with density ρ). From the energy deposited ΔE_1 we deduced a value of the LET. Then, a new layer of material was added and we again calculated the energy deposited in this second layer using the energy $E_1 = E_o - \Delta E_1$ as the new initial energy of the proton. A new value of the LET was deduced from the deposited energy ΔE_2. The same procedure was continued until the total desired total absorber thickness was reached. The whole track dose-average LET could then be easily obtained from the average of all LET values associated with each layer thickness considered. Table 5.1 illustrates our computational approach using IONLYS in the case of an incident 0.465 MeV recoil proton in water at 400 °C and 0.6 g/cm^3 density.

Once the dose-average LET was known, the corresponding "dose-average" energy of the irradiating protons could readily be obtained with the aid of Fig. 5.1, which shows a plot of the LET against proton energy at the temperature and water densities of interest. Our Monte Carlo track chemistry simulations were thus performed under the simplifying approximation that the energies of the three intervening recoil protons remained *constant* when passing through the SCW medium. These constant average energy values ($\overline{E}_{p_{i=1,2,3}}$) were found to be ~0.6, 0.3, and 0.17 MeV, respectively. As mentioned above, these values varied only slightly as a function of water density and were therefore kept constant in all our chemical yield calculations.

Table 5.1 – Energy deposition profile of a 0.465 MeV recoil proton beam incident in supercritical water at 400 °C and density 0.6 g/cm^3 as calculated using our IONLYS simulation program (see text).

Energy of the incident beam (keV)	Distance travelled (μm)	LET (keV/μm)	Energy deposited (keV)
465	2	25.701	51.403
413.597	2 (4)	27.541	55.082
358.515	1 (5)	30.040	30.040
328.475	1 (6)	33.249	33.249
295.226	1 (7)	35.471	35.471
259.755	1 (8)	38.011	38.011
221.744	1 (9)	40.922	40.922
180.822	1 (10)	44.304	44.304
136.518	1 (11)	45.461	45.461
91.057	1 (12)	40.238	40.238
50.819	1 (13)	20.414	20.414

To confirm the validity of this computational approach, we also calculated the absorbed dose-average LET for an incident 1.264 MeV recoil proton in ordinary liquid water at 25 °C. The corresponding dose-average energy is 0.565 MeV, a value quite comparable to that of 0.495 MeV found in the compilation of Watt (1996).

As described in Chap. 2, our focus in this work is to calculate the chemical yields of the various radiolysis products formed in the radiolysis of SCW at 400 °C, with a special emphasis on the *in situ* production of H^+ ions and the resulting "acid-spike" response, using different types of radiation. In this regard, we chose 300 MeV protons and 2 MeV neutrons as the irradiating particles characteristic of low- and high-LET radiations, respectively. Results for 2 MeV incident neutrons are presented in Chap. 4; as mentioned above, these results have been accepted for publication in the *Canadian Journal of Chemistry* (January 10, 2019). We show below our results for 300 MeV irradiating protons. A publication on the subject is currently under preparation. Finally, a brief, combined discussion of these two sets of results will conclude all of this work.

5.3 Generation of ultrafast transient "acid spikes" in SCW at 400 °C irradiated with 300 MeV protons

Our computed yields of e^-_{aq}, $H^\bullet$, $^\bullet OH$, and H_2O_2 in pure, deaerated SCW (H_2O) irradiated by 300 MeV incident protons at 400 °C are shown in Fig. 5.4 as a function of time at two fixed water densities, ρ = 0.15 and 0.6 g/cm^3. To our knowledge, there is unfortunately no experimental information in the literature with which to compare these results. Recall here that the yield of a species at a given time represents the balance between production and consumption of that species by all chemical reactions at that particular time.

Inspection of Fig. 5.4 indicates that the marked increase of $G(^\bullet OH)$ – and the corresponding decrease of $G(H^\bullet)$ – observed at times longer than ~10^{-7}-10^{-6} s (depending on the density) results from the *oxidation of water by the $H^\bullet$ atom* in the homogeneous chemical stage (Swiatla-Wojcik and Buxton, 2005, 2010; Bartels, 2009; Elliot and Bartels, 2009; Sanguanmith et al., 2013; Alcorn et al., 2014; Butarbutar et al., 2014*a*; Muroya et al., 2017):

$$H^{\bullet} + H_2O \rightarrow H_2 + {}^{\bullet}OH\,, \qquad k(400\ ^{\circ}C) = 6.3 \times 10^{4}\ M^{-1}\ s^{-1}. \tag{5.b}$$

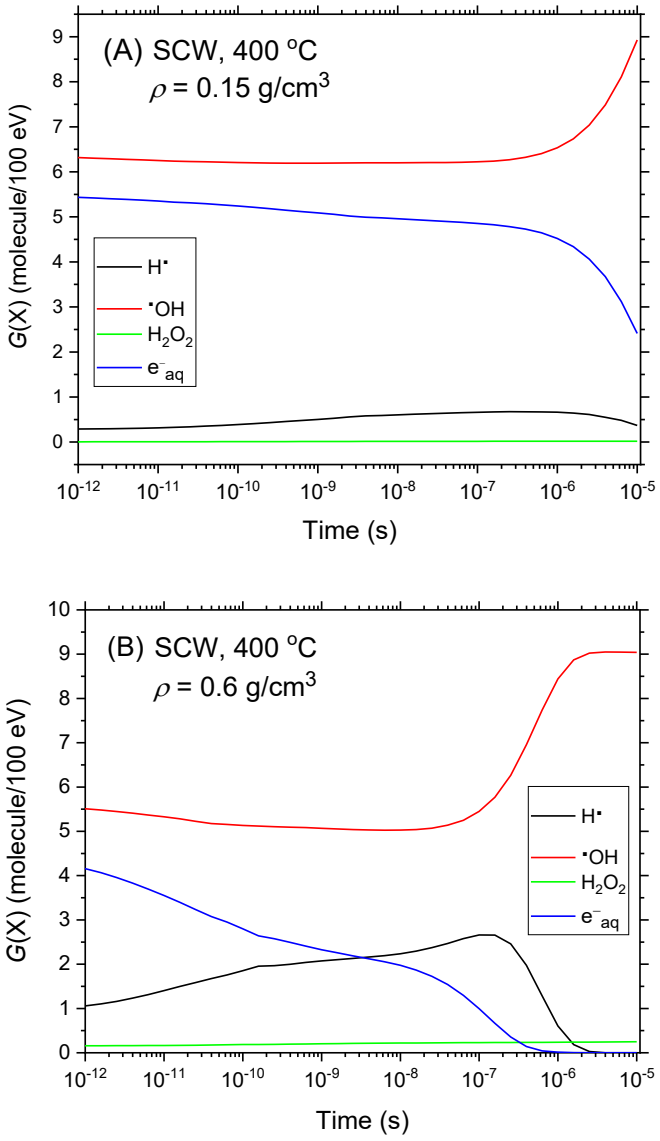

Figure 5.4 – Time evolution of the yields of e^-_{aq}, $H^{\bullet}$, $^{\bullet}OH$, and H_2O_2 (in molecule per 100 eV) calculated from our Monte Carlo simulations of the radiolysis of pure, deaerated water by 300 MeV incident protons at 400 °C for the lowest (0.15 g/cm^3, Panel A) and highest (0.6 g/cm^3, Panel B) water densities considered, in the interval of ~1 ps to 10 μs. The LET values for these two densities were ~0.07 and 0.20 keV/μm, respectively.

Interestingly, reaction (5.b) received much attention in the last decade in view of its potential importance in the radiolysis of water at elevated temperatures. In particular, this reaction was proposed to quantitatively explain the large, anomalous increase of the

"escape" yield of H_2 observed experimentally in the low-LET radiolysis of water above ~200 °C (Sunaryo et al., 1995; Swiatla-Wojcik and Buxton, 2005; Sanguanmith et al., 2011). Despite the recent experiments of Alcorn et al. (2014) and Muroya et al. (2017), this reaction nevertheless still suffers from some controversy as to the value of its rate constant, especially in supercritical water. Because of this uncertainty, it is difficult to conclude as to its exact contribution to the formation of either $^{\bullet}OH$ radicals or molecular hydrogen.

Figure 5.5 shows the time evolution of $G(H_3O^+)$ and $G(OH^-)$ as obtained from our simulations of the radiolysis of pure, deaerated SCW (H_2O) by 300 MeV incident protons at 400 °C, over the interval of ~1 ps to 10 μs, for different water densities in the range of 0.15-0.6 g/cm^3. As pointed out before, the hydroxide ion OH^-, formed largely by the reaction (Liu et al., 2018):

$$e^-_{aq} + {}^{\bullet}OH \rightarrow OH^- , \quad k(400\ ^{\circ}C) = 1.7 \times 10^{11}\ M^{-1}\ s^{-1} \qquad (5.c)$$

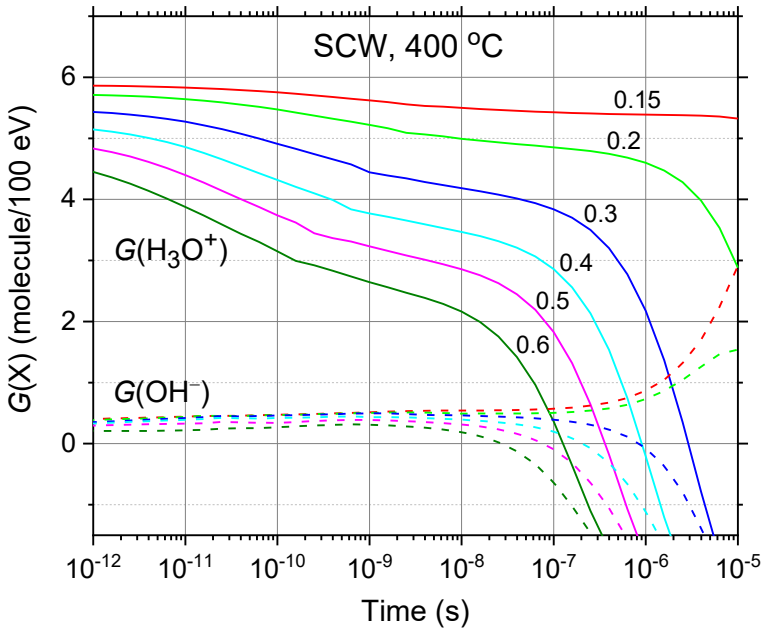

Figure 5.5 – Temporal evolution of the yields of radiolytically produced H_3O^+ (solid lines) and OH^- (dashed lines) ions obtained from our Monte Carlo simulations of the radiolysis of pure, deaerated SCW at 400 °C by 300 MeV incident protons, for six different water densities: 0.15 (red), 0.2 (green), 0.3 (blue), 0.4 (cyan), 0.5 (magenta), and 0.6 (olive), in the interval of ~1 ps to 10 μs.

contributes to an *alkaline* spur and consequently counteracts the acid-spike effect discussed here. However, as we can see from Fig. 5.5, $G(OH^-)$ remains much smaller than $G(H_3O^+)$ over the time range of interest, independent of the considered density. As a result, its effect modifies the quantitative features of the pH only slightly and can be ignored to a good approximation.

The observed decrease of $G(H_3O^+)$ is predominantly due to H_3O^+ reacting with OH^- and with the hydrated electron, according to:

$$H_3O^+ + OH^- \rightarrow 2H_2O \qquad (5.d)$$

$$H_3O^+ + e^-_{aq} \rightarrow H^\bullet + H_2O. \qquad (5.e)$$

Other reactions, such as $H_3O^+ + O^{\bullet-} \rightarrow {}^\bullet OH + H_2O$ and $H_3O^+ + HO_2^- \rightarrow H_2O_2 + H_2O$, also contribute to the decay of $G(H_3O^+)$, but only very weakly.

The effect of density (pressure) on the yield of H_3O^+ has already been discussed in detail in Chap. 4 in terms of solvent *cage effect*, which, depending on the density, may or may not favor the combination/recombination reactions of the caged radiolytic products. This discussion will not be repeated here. Rather, we found it interesting to illustrate this effect by presenting below the evolution of the time dependence of the cumulative yield variations $\Delta G(H_3O^+)$ for the two reactions (5.d) and (5.e) that contribute to the decay of $G(H_3O^+)$ for the sequence of the densities ρ = 0.15, 0.2, 0.3, 0.4, 0.5, and 0.6 g/cm^3 (Fig. 5.6A-F).

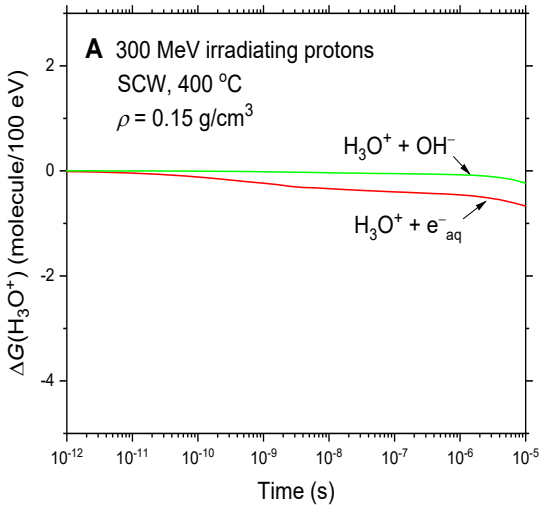

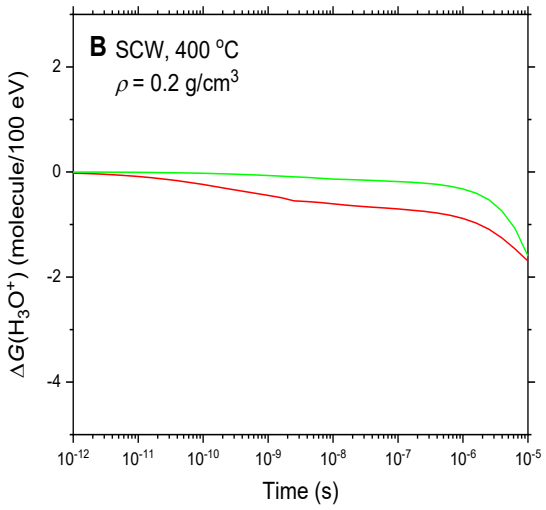
B SCW, 400 °C
ρ = 0.2 g/cm3
ΔG(H3O+) (molecule/100 eV)
2
0
-2
-4
10-12
10-11
10-10
10-9
10-8
10-7
10-6
10-5
Time (s)

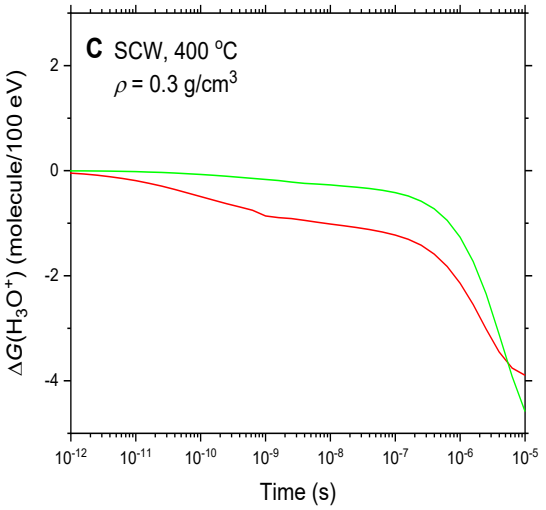
C SCW, 400 °C
ρ = 0.3 g/cm3
ΔG(H3O+) (molecule/100 eV)
2
0
-2
-4
10-12
10-11
10-10
10-9
10-8
10-7
10-6
10-5
Time (s)

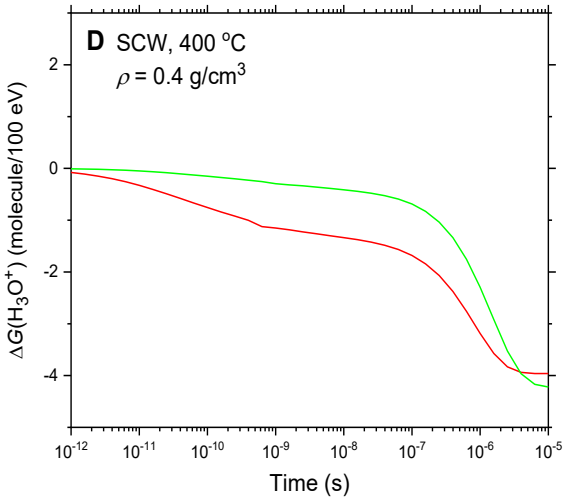
D SCW, 400 °C
ρ = 0.4 g/cm3
ΔG(H3O+) (molecule/100 eV)
2
0
-2
-4
10-12
10-11
10-10
10-9
10-8
10-7
10-6
10-5
Time (s)

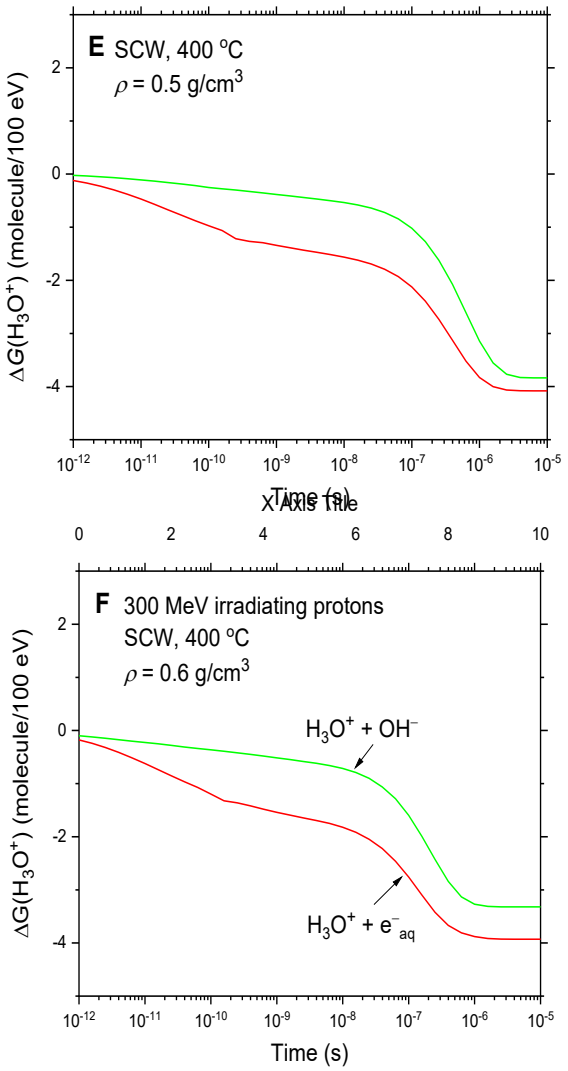

Figure 5.6 – Time dependence of the extents $\Delta G(H_3O^+)$ (in molecule per 100 eV) of the two main reactions (5.d) (green lines) and (5.e) (red lines) that are involved in the decay of H_3O^+, calculated from our Monte Carlo simulations of the radiolysis of pure, deaerated water by 300-MeV incident protons at 400 °C for ρ = 0.15 (A), 0.2 (B), 0.3 (C), 0.4 (D), 0.5 (E), and 0.6 (F) g/cm^3, in the interval of ~1 ps to 10 µs.

As we can see in Fig. 5.6, the (H_3O^+ + OH^-) and (e^-_{aq} + H_3O^+) reactions become progressively more important at the higher, liquid-like water densities. Due to the large solvent barrier, caged radiolytic products are forced to remain as colliding neighbors in the proton track where they formed, resulting in a rapid decrease in $G(H_3O^+)$.

As H_3O^+ ions generate acidity, it is important to determine their relative positions in the track. Figure 5.7 shows typical 2-D representations of the track

segments of a 300-MeV irradiating proton in SCW at 400 °C calculated with our IONLYS Monte Carlo program for the lowest (0.15 g/cm^3) and highest (0.6 g/cm^3) water densities considered.

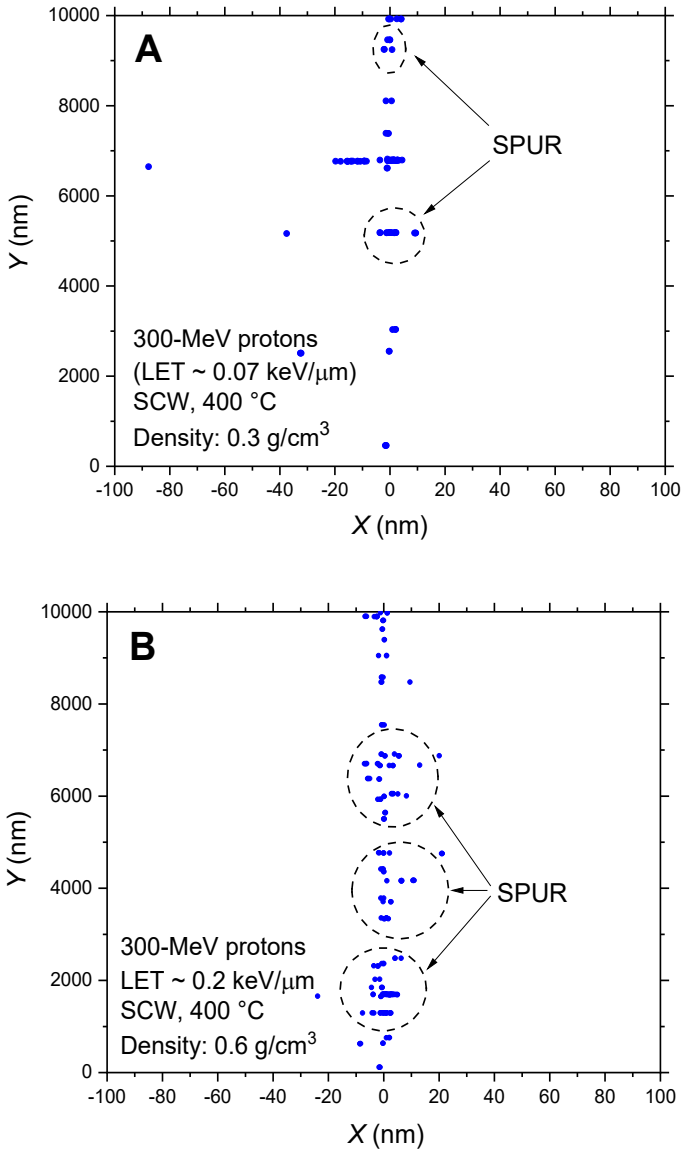

Figure 5.7 – Simulated track histories (at ~10^{-13} s, projected onto the *XY* plane of the figure) of a 300-MeV proton incident on SCW at 400 °C for ρ = 0.15 (A) and 0.6 (B) g/cm^3. The two irradiating protons are generated at the origin and start travelling along the *Y*-axis. Dots represent the energy deposited at points where an interaction occurred.

In both cases, the track is distinguishable into separate "spurs" (nearly spherical in shape) and each spur develops independently with time (the so-called "spur expansion"), that is, without interference from the neighboring spurs (see Sect. 1.4.1). In other words, the track can be approximated as made up of a string of spurs. This is a typical "low-LET" situation, and for it the *isolated spur model* is appropriate (Magee and Chatterjee, 1987). Under these conditions, the pH must be calculated individually for each spur.

As described in Chap. 3, for the case of the isolated "spherical" spur model, the *total* concentration of H_3O^+ is the sum of $[H_3O^+]_{radiolytic}$ given by Eqs. (3.b-3.c) and of the non-radiolytic, pre-irradiation concentration $[H_3O^+]_{autoprotolysis}$ that results from the autoprotolysis of water (Table 5.2):

$$\left[\mathrm{H_3O^+}\right]_{total}(t) = \left[\mathrm{H_3O^+}\right]_{radiolytic}(t) + \left[\mathrm{H_3O^+}\right]_{autoprotolysis}. \tag{3.f}$$

The pH in the corresponding spur regions is then simply given by the negative logarithm (to the base 10) of $[H_3O^+]_{total}$:

$$\mathrm{pH}(t) = -\log\left\{\left[\mathrm{H_3O^+}\right]_{total}(t)\right\}, \tag{3.g}$$

Table 5.2 – Variation of the dissociation constant of water, K_w, with density at 400 °C (Bandura and Lvov, 2006).

Density ρ (g/cm^3)	Dissociation constant K_w (mol^2/L^2)	$[H^+]$ (mol/L) from the autoprotolysis of water
0.15	6.48806×10^{-18}	2.54717×10^{-9}
0.3	1.33247×10^{-14}	1.15433×10^{-7}
0.4	1.12707×10^{-13}	3.35719×10^{-7}
0.5	6.79857×10^{-13}	8.24534×10^{-7}
0.6	5.31767×10^{-12}	2.30601×10^{-6}

The time evolution of the pH values calculated for 300 MeV irradiating protons in pure, deaerated SCW at 400 °C using the spherical spur geometry is shown in Fig. 5.8. As shown, for all water densities considered in the range of 0.15-0.6 g/cm^3, there is an abrupt, temporary and highly acidic pH effect at early times, immediately after the initial energy release. Its magnitude and duration depend on the density. At times less than 10 ps, the pH for the highest ("liquid-like") and lowest ("gas-like") densities considered, was around 1.8 and 2.2, respectively. Interestingly, these pH values are slightly higher than those (0.8 and 1.3, respectively) found when SCW at 400 °C is irradiated with 2 MeV neutrons (Chap. 4). At longer times, the pH gradually increases for all densities, finally reaching a constant value corresponding to the non-radiolytic, pre-irradiation concentration of H_3O^+, due to the autoprotolysis of water. As we can see from the figure, the lower the density of the water, the longer the time required to reach this constant value.

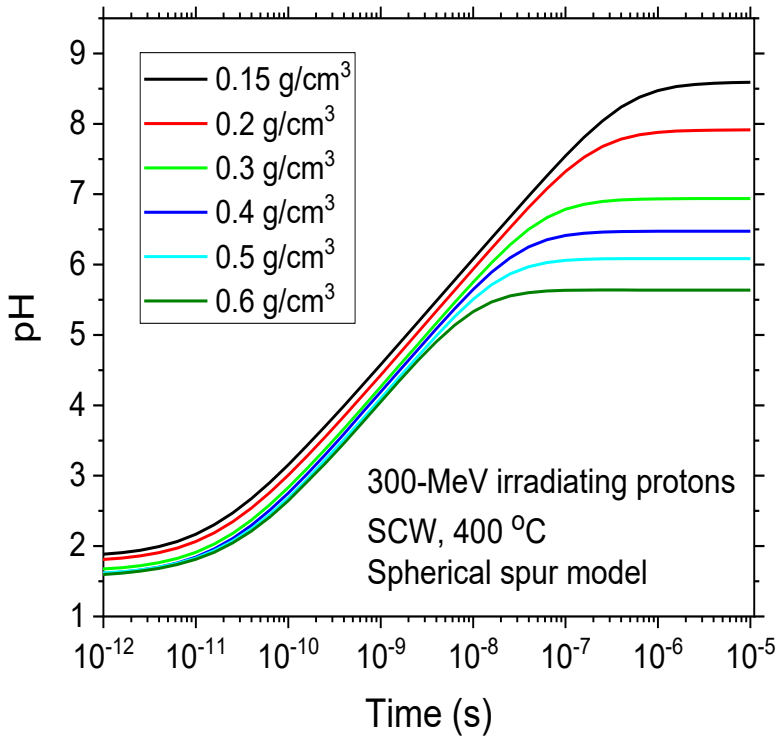

Figure 5.8 – Variation of pH with time in a spur calculated for pure, deaerated SCW at 400 °C and different water densities between 0.15 and 0.6 g/cm^3 and in the interval of ~1 ps to 10 μs, for irradiating 300-MeV protons using the isolated spherical spur model, characteristic of low-LET radiation.

5.4. Implication of our work

The section is dedicated to explaining the possible implications of the radiolytically generated species *in the context of nuclear reactors*. Two points will be discussed:

1. The yield of important radiolytic species.
2. The yield of protons.

5.4.1. Yield of important radiolytic species in the context of a nuclear reactor

Once the nuclear reactors were ready to operate, they involved at the same time understanding how to control them and how to increase their working age because of the high investment costs associated with construction and maintenance. In addition, reactor safety is of great importance for the mass security of the areas where they are installed. According to our simulations, radiolysis of supercritical water produces a number of different reactive species. The $^{\bullet}OH$ radical is the most powerful oxidative species that frequently participates in the abstraction and reduction reactions of electrons leading to the release of ions in the system. Moreover, H_2O_2 is closely related to the corrosion of in-reactor materials as well as in containers with spent nuclear fuel.

It is also important to know the impact of radiolytically generated $H^{\bullet}$ atoms in close vicinity of metal surfaces and the relative stability of metals in such environment (LaVerne, 2005; Choudhry et al., 2016). It is known that hydrogen can be absorbed by metals via diffusion through preferred specific pathways that have low energy barriers for $H^{\bullet}$ atom migration. These hydrogen atoms then combine within the metallic crystal and cause modifications of the vacancy-vacancy interactions, which result in the formation of internal cavities and other defects accompanied by a degradation of the physical and chemical properties of the materials (Ganchenkova et al., 2014). This is also a major concern in determining the “critical hydrogen concentration” to add in the coolant in order to mitigate the radiolysis of water in the reactor core. In one of their recent papers, Lousada et al. (2016) showed that γ-radiation induces hydrogen absorption by copper in water.

H_2O_2 is well known for its very high oxidizing capacity. According to Satoh et al. (2004), the radiolytically generated hydrogen peroxide has a greater importance for the "electrochemical corrosion potential" (ECP) than the oxygen itself (for a certain concentration range of dissolved O_2). This ECP is considered as the corrosivity index of a medium. The effect of hydrogen peroxide on "stress corrosion crack" (SCC) growth rate of sensitized 304 stainless steel in high-temperature water was investigated and it was found that H_2O_2 accelerated crack growth irrespective of dissolved oxygen content level within the test range (20–400 ppb dissolved O_2) (Anzai et al., 1994).

The effect of γ radiation on the corrosion of carbon steel and stainless steel in contact with high-temperature water has been studied since the seventies, and it was shown that although irradiation does not seem to have a marked effect on the corrosion of stainless steel, it accelerates the corrosion of carbon steel about 3–4 times (Ershov et al., 1985).

To prevent the formation of oxidizing species in the reactor coolant, molecular hydrogen is added. Excess H_2 prevents the buildup of a steady-state concentration of H_2O_2 (formed mainly by the reaction $^{\bullet}OH + {}^{\bullet}OH \rightarrow H_2O_2$) and its decomposition product O_2. The following reaction of hydroxyl radicals with excess H_2:

$$H_2 + {}^{\bullet}OH \rightarrow H_2O + H^{\bullet} . \qquad (5.f)$$

serves to convert the oxidizing $^{\bullet}OH$ radicals to the reducing $H^{\bullet}$ atom, and ensures that reducing conditions are maintained within the coolant, which is important for the prevention of stress corrosion cracking (Spinks and Woods, 1990; Sims et al., 2013; Was et al., 2007). The backward reaction: $H^{\bullet} + H_2O \rightarrow H_2 + {}^{\bullet}OH$ is relatively slow at current reactor operating temperatures (~250-300 °C). However, under SCW conditions, this back reaction may become significant (Liu et al., 2018; Muroya et al., 2017). Recently proposed models have shown that the addition of any reasonable amount of H_2 can only reduce, *but not suppress*, the radiolytic production of H_2O_2 (Guzonas et al., 2018). Additional work is needed at this time to better understand SCW chemistry in order to specify possible water chemistry control strategies for a SCW reactor.

5.4.2 Yield of protons in the context of a nuclear reactor

Water radiolysis produces H_3O^+ ions along the track at very early time (~200 fs) (see Fig. 1.3):

$$H_2O^{\bullet+} + H_2O \rightarrow H_3O^+ + {}^{\bullet}OH. \qquad (5.g)$$

Since these ions do not have any other radiolytic products with which to react at this time (Morrison, 1952), an acidic environment is created. Experimental evidence for an acidic track has been described in the literature (Spinks and Woods, 1990; Byakov and Stepanov, 2006), but no quantification or direct measurement of the extent of this acidity was performed. This is not really surprising, as the protons generated gradually participate in different types of reactions with different species formed and are consumed quickly. The measurement of acidity at a very early stage is not possible due to the lack of appropriate instrumentation. Pulse radiolysis or spectroscopic methods, in this case, give a pH value of the bulk solution but say nothing of what happens in the localized tracks.

Two experiments *indicative of an acid spur* have been reported (Spinks and Woods, 1990). The first evidence has been obtained by irradiating solutions of 1,1-diethoxyethane buffered to pH 7 and showing that hydrolysis, *i.e.*,

$$CH_3CH(OC_2H_5)_2 + H_2O \xrightarrow{H^+} CH_3CHO + 2C_2H_5OH\,, \qquad (5.h)$$

occurs although it normally requires a pH of about 1.4 to be observed. This means that for at least some time, there are certain regions in the solution where the pH was around 1. The second experiment is the observation of absorption attributed to $Cl_2^{\bullet-}$ when concentrated neutral solutions of inorganic chloride are irradiated. The formation of $Cl_2^{\bullet-}$ normally requires an acidic medium. Note, however, that there is an alternative explanation for this observation, based on the intervention of a positive entity that would not necessarily be H_3O^+ (possibly $H_2O^{\bullet+}$) (Matsuyama and Namiki, 1965). In any case, two simulation studies from our laboratory (Kanike et al., 2015; Islam et al., 2018) have quantified the extent of acidity that develops along a low- and high-LET radiation track. To the best of our knowledge, this was the first approaches to quantify the transient acidity generated along radiation tracks.

It is most remarkable that our present Monte Carlo simulations indicating the existence of a strong "acid-spike" effect along radiation tracks fully agrees with the qualitative physical picture of Fig. 5.9 developed first by Lea (1946) and later by Morrison (1952) some 70 years ago (at a time when the hydrated electron had not yet been discovered).

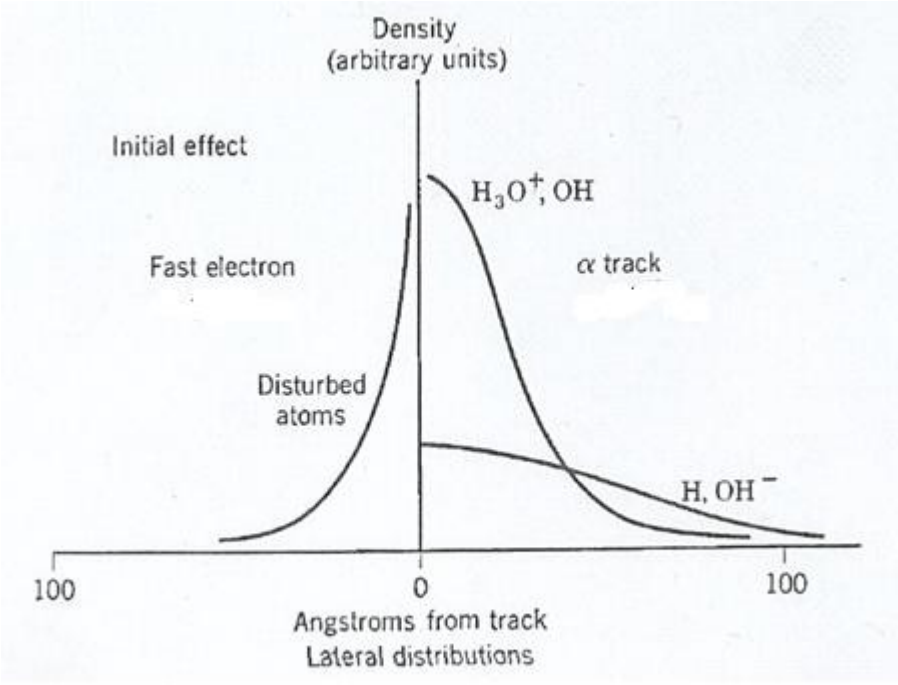

Figure 5.9 – Lateral distribution of the initial products across an ionizing track in liquid water. Left side: distribution immediately after passage of a fast electron. Right side: distribution of diffusing positive and negative ions after a α-particle has traversed water. The charge separation is due to the faster motion of the secondary electrons, which are captured some distance from the track. Adopted from Morrison (1952).

Figure 5.9 shows the lateral distribution of the different radiolytic species as a function of the distance from the track of a heavy α-particle at two different times. At early time ($<10^{-14}$ s), the initial species like free electrons from ionization, as well as excited and ionized water molecules, are produced. Due to their high mobility, "dry" secondary

electrons quickly move quite away from the track, whereas other species like H_3O^+ and $^{\bullet}OH$ (whose mobilities are comparatively very low) stay close to the main track. As we can see, there is a clear *charge separation* between the more concentrated positive-ion (mainly H_3O^+ and OH) core of the track and the negative ions (mainly OH^- and $H^{\bullet}$) in the surrounding medium somewhat distant from the track. Due to this initial charge separation, H_3O^+ escapes its two major scavengers (e^-_{aq} and OH^-) and therefore renders the track more acid than the surrounding medium. As a function of time, it is easy to see that this local acidity will last until the diffusion of H_3O^+ and $^{\bullet}OH$ has brought these two species to the remote positions then occupied by the hydrated electrons.

The working age of a nuclear power plant is limited by the extent of corrosion of the reactor materials. A great deal of research is carried out worldwide to study the mechanisms of corrosion and the possible ways to mitigate the problem. Nevertheless, certain unavoidable factors cannot be excluded, whatever the condition chosen. As examples, a material at a higher temperature exhibits a different character in terms of electrochemical potential, the building materials have natural defects such as crevices in formation, and also the case where different materials (placed at different points in the electrochemical series) need to be connected. It is also inevitable that the atoms of a material crystal are frequently displaced from their original position by exposure to radiation. These displacements in the atomic positions produce roughness on the surface and make the materials more susceptible to attacks from different elements of the environment (Andresen et al., 1991). The environment in the reactor core is extremely aggressive due to the presence of radiolytically generated reactive species, which are responsible for several types of corrosion in the construction materials. A crevice in the wall or near the joints may assist in the geometric progression of corrosion of the materials (Fontana, 2008). In crevice corrosion, the scarcity of oxygen or suitable oxidizing agent into the crevices makes the region inside the crevice anodic in nature with respect to outside of the crevice. This situation accelerates the release of metal ions inside the crevice. As the total number of positive metal ions increases inside the crevice, more ions that are negative rush to the crevice and make the environment even more corrosive. The connections of different materials positioned at different levels in the electrochemical series may cause galvanic corrosions. The stainless steel that was

used before in nuclear power plants was associated with inter-granular corrosion due to the presence of carbon. Of all these types of corrosion, "*stress corrosion cracking*" (SCC) is certainly the most important and perhaps the most common from the point of view of a nuclear reactor. SCC usually takes years to develop and then it spreads destructively.

Stress corrosion cracking is a complex phenomenon driven by the synergistic interaction of mechanical, electrochemical, and metallurgical factors. Both BWR ("boiling water reactor") and PWR ("pressurized water reactor") components can suffer from SCC, which may have trans-granular (through the grains) or inter-granular (along with the grain boundaries) (a grain boundary is an interface between two grains, or crystallites, in a polycrystalline material) morphology. The three necessary pre-conditions of stress corrosion cracking are:

- A susceptible material;
- A tensile stress component;
- An aqueous environment.

In practice, stress on material always exists under the high operating temperature conditions of a nuclear power plant. It is logical that a slight increase in the impurities in this situation might drastically change the picture of the overall corrosion. An acidic environment is destructive in the same way. In our calculations, we showed that a marked decrease in the pH along the radiation track occurs and persists up to the microsecond-nanosecond time range, depending the water density. Even if such a time scale is rather short to initiate some interaction in the material directly, we believe that this local acidity can be a synergistic factor in the initiation and propagation of the SCC. Perhaps even more importantly, once a crack is developed, radiolysis in the crack and the resulting "acid spikes" could dramatically accelerate the SCC process.

If we look at the electrochemical series, which represents the relative ease of an element to be oxidized or reduced, the ease is calculated from the value of the reduction potential given. As shown in Table 5.3, going from top to bottom, the downward trend is increased. For example, Li^+ is less prone to be reduced than K^+. The reverse order is also true; Li has the highest tendency to be oxidized.

Surprisingly, almost all the materials used in a nuclear power plant are positioned above H^+. Therefore, in a medium containing an excess of H^+, the following material will be prone to be corroded. This is why pH is one of the most important parameters that needs to be strictly controlled in a nuclear power plant.

Table 5.3 – Electrochemical series.

Reaction	Product	Electrochemical reduction potential (V)
$Cu^{2+}+ 2e^-$	Cu	+0.15
$2H^+ + 2e^-$	H_2	0
$Pb^{2+} + 2e^-$	Pb	-0.13
$Ni^{2+} + 2e^-$	Ni	-0.26
$Fe^{2+} + 2e^-$	Fe	-0.45
$Zn^{2+} + 2e^-$	Zn	-0.76

A detailed mechanism of corrosion in the materials that are usually observed in a nuclear power plant is shown in Fig. 5.10. A balance is maintained between anodic and cathodic current, and this current is generated from the oxidation and reduction in the anode and cathode, respectively. The cathodic reaction is the reduction reaction of oxygen or proton on the surface of materials. Oxygen takes up electrons to produce an oxide ion. This oxide ion combines with metallic ions and stays adherent to the surface. This is called an *oxide film* and it actually protects the materials from further corrosion. However, the abrupt flow of water in the core of a nuclear reactor often destroys the film letting the oxide layer erode from the surface and leaving behind an unprotected corroded surface. This surface of metals later may take part in another different form of corrosion. If H^+ is present in contact with the surface of metals, they also can take part in the reduction reaction. On the other hand, the anodic reaction is caused by the electron release reaction of the metals. When the metal atoms lose electrons, they become metal ions and move away from the surface. The corrosion behavior of nickel-base alloys 625 and C-276 is investigated across the critical temperature of water at a constant pressure in aqueous solutions. In pH 2, Ni and Fe are selectively dissolved, and

Cr and Mo form stable oxides. In pH 1, Cr, Ni, and Fe are dissolved from the substrate and Mo forms a stable oxide (Kim et al., 2010). This experiment describes the pH-dependent corrosion pattern of an alloy. However, the problem remains, because the acidity maintained here is a bulk acidity and yet, it is not confirmed that the radiolytically transient event of the "acid spike" is sufficient to cause damage to the materials of construction. In this regard, Lousada et al. (2016) irradiated a piece of copper kept in water with γ-rays. The authors then analyzed this piece and found that it absorbed H_2, which is more than ten times higher than the system without irradiation, as confirmed by "temperature-programmed desorption" (TPD) measurements. They also noticed nanostructure deposits, nano-grooves development after analyzing the structure. This confirms that irradiation is able to bring additional events to the system and that transient events due to water radiolysis are able to affect the system of their production. Let us give an approach to explain the phenomena, in this case, in the light of electrochemical interactions. The oxidation potentials of $^{\bullet}OH$, Cu, and H^+ are 2.7, 0.36, and zero V, respectively. Electrochemical reactions between the elements are likely to corrode Cu, to reduce molecular hydrogen. However, this phenomenon still does not explain the absorption of H_2 by Cu and the deposition of microgrooves in the piece of copper.

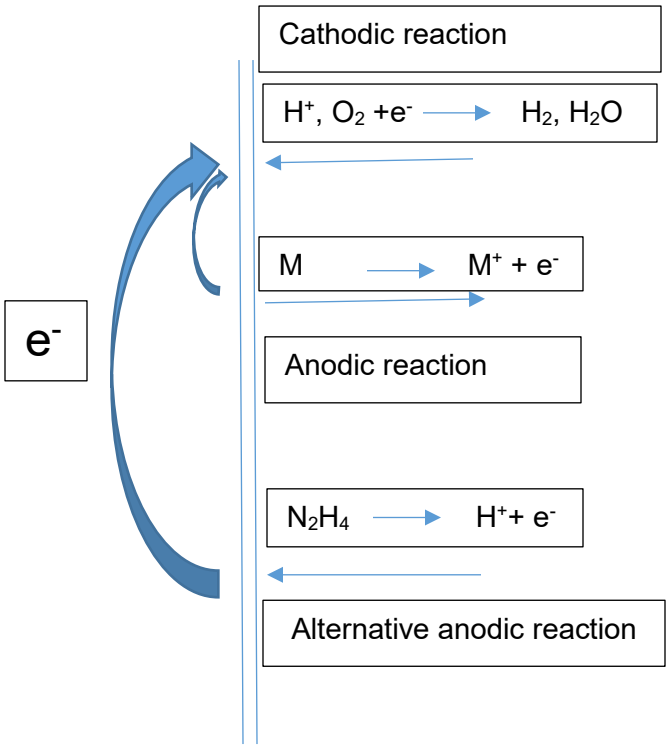

Figure 5.10 – Net balance of electrochemical reactions on a metal surface. Adapted from Uchida et al. (2008).

To remove this type of corrosion from species that are oxidizing in nature, hydrazine is now used which would preferably give the electron to maintain equilibrium with the cathodic current.

This is due to the important contribution of pH to corrosion that leads it to be one of the strictly controlled parameters in the nuclear power plant.

Pourbaix diagrams can be used to predict the effect of pH and electrochemical potential on the possible stable (equilibrium) phases of an aqueous electrochemical system. This diagram uses the basic thermodynamic relationship between the Gibbs free energy and electrochemical potential where Gibbs free energy concept validates the thermodynamic facts of a probable reaction and ECP says about the electrochemical probability of the reaction (Satio et al., 2006; Kriksunov and Macdonald, 1995, 1997). This study of Pourbaix diagrams has been extended to a number of systems, including water iron, water chromium, and water-nickel systems at temperatures up to 400 °C (Cook and Olive, 2012*a*,*b*). These diagrams say that with the decrease of pH, the tendency of the release of metal atoms in the form of ions increases. However, it should be noted that Pourbaix diagrams, at a high temperature, may have some sort of limitations because they do not account for the local morphology of oxide layers and their inability to account for the local variations of pH in crevices and pits. Lately, Mitton et al. (2000) and Guzonas et al. (2010, 2018) showed that the overall material release is higher in case of lower pH of the medium. In the work of Daub et al. (2011), the effect of γ-radiation on the kinetics of carbon steel corrosion has been investigated by characterizing the oxide films formed on steel coupons at 150 °C in aqueous solutions and at two pH values. According to this study, it is stated that the variations in system temperature and pH may affect rates of oxide film growth and dissolution.

All the discussions described in the previous section imply corrosions in bulk situation and do not say anything about what happens in crevices and pits although corrosions in crevices and pits ultimately influence overall corrosion. However, local

variations of pH in crevices are of other technical importance because it will help understand the mechanism of overall corrosion.

5.5 How is corrosion damaging for nuclear reactors?

Corrosion in nuclear reactors may prove to be very critical. The history of Fukushima can be a reference in this case (Willacy, 2013). A devastating earthquake followed by a tsunami let the destruction of the nuclear power plant facility. Significant impact on the ecosystem of the region was inflicted by this accident. After the accident, it was also important to keep the release of radioactivity from the reactor core to the environment under control. Thereby, the authorities implemented a plan that they would spray water over the reactor core. Later, it also became important to preserve the wastewater to a containment reservoir so that the water does not pollute the environment. After some years, in 2013 there had been a report that a vast quantity of water spilled out of the reservoir and mixed with the water at the nearby seashore. This actually allowed a wide spread contamination of the ecosystem of the region. In addition, the authorities had to abandon fishing in that seashore. Later, the reason why the water was leaked within this short timescale was determined. It was found that accelerated corrosion of materials due to wastewater in the tank was responsible for water leakage. The water was already contaminated with radioactive waste. In addition, the radiolysis of the water continuously produced different aggressive reactive species, such as $^{\bullet}OH$, H_2O_2, O_2, H^+, *etc*. This actually made the water more corrosive than normal water. The materials of construction being already in a state of tension because of the extreme conditions of high temperatures and pressures, this reactive environment should make them even more susceptible to corrosion.

6. CONCLUSION

The development of Gen-IV SCW reactors requires a comprehensive research and proper integration of all possible data accumulated on these reactors during their design. Radiation chemistry, which is an integral part of any nuclear reactor design, is essential to understanding the mechanisms that could ensure the safety of the reactor. In this study, a Monte Carlo approach was used to simulate the complex physical chemistry/chemical physics phenomena that take place inside a radiation track. The simulation program was developed entirely in our laboratory and in this work, several modifications were made to take into account the specificities of supercritical water. The temperature was fixed at 400 °C and the program was run at different water densities in the range of 0.15-0.6 g/cm^3 to mimic the coolant conditions in the heat transport system of SCW reactors. As with other simulations, the results were compared with the data experimentally available in the literature for validation.

We calculated the yields of the different reactive species formed in the radiolysis of SCW for both low- (300 MeV protons) and high- (2 MeV neutrons) LET irradiations. Most importantly, we quantified the radiolytically generated H^+ and OH^- ions along the radiation tracks. We showed that there was an abrupt, transient, marked decrease (~ 1) in the local pH for some time (~μs). In addition, this "acid spike" response was more pronounced and more durable when the density of water was lower.

To understand the possible impact of this acidity, we tried to correlate the *corrosion* mechanisms of metals with the *acidic* (low pH) *radiation tracks*. Electrochemical considerations suggested that there could be a probability of electrochemical interaction between these two entities. Some of the experimentally available data indirectly suggested this as well. If this is indeed the case, radiolysis that generates local acidity in the tracks, although transitory, could prove to be one of the important factors to consider when designing the reactor.

7. ACKNOWLEDGEMENTS

My dream of doing research came true when I was admitted as a M.Sc. student in the Department of Nuclear Medicine and Radiobiology, Faculty of Medicine and Health Sciences, Université de Sherbrooke, followed by a two-year scholarship from the "Centre de Recherche Médicale de l'Université de Sherbrooke (CRMUS)". At first, I felt honored and my dream came reality. I would like to thank the authorities for all these good things.

I would like to express my deep heart gratitude to Prof. Jean-Paul Jay-Gerin, my supervisor, for the opportunity he gave me to join his group. Beyond the research, he contributed greatly to my personal development. After two years with him, I am completely a new man with a new vision of life. Besides, Jean-Paul masters the science and knows how to make a student mastering a topic. I think a few words of acknowledgement is not enough for that.

I appreciated the help and support of Dr. Jintana Meesungnoen, Sunuchakan Sanguanmith, Esteban Sepulveda, Tait Du and most importantly, Muhammad Mainul Islam, my colleague, friend and a brother. Shayla Mumu apu, Gulam Musawir khan vhai were like my family and they helped me feel home here in Sherbrooke. Also, I would like to thank Professor Richard Wagner and Hakim Belmouaddine, who opened a new dimension to my research career.

Special thanks go to Prof. Yosuke Katsumura for his helpful correspondence, discussions, and necessary intellectual support to accomplish this research. I would like to thank Prof. James F. Ziegler for his kind help to use SRIM programs. I am also very much grateful to Prof. Richard Wagner and Prof. Armand Soldera for their kind approval to review my thesis and be the jury members.

Professor Martin Lepage is probably one of the greatest persons I ever met. He helped me both academically and non-academically. My gratitude to him is inexpressible in words. Mr. Yacine Tabet and Mrs. Jennifer Chambers deserve a big appreciation for their continuous support. They are so kind that they feel the problems of the students as their own.

Finally, I would like to thank my parents who always supported me to pursue my dream. It would not have been possible to go forward for me without their support and guidelines. My parents are magicians and great scientists, who could stimulate my dream and could think out of the box, despite of their limitations. I would like to offer them my appreciation for the love and support they have given me through all my life.

8. REFERENCES

Aaltonen, P., and Hanninen, H., 1997. Water chemistry and behavior of materials in PWRs and BWRs. Report IAEA-TECDOC-965, pp. 205–222. International Atomic Energy Agency, Vienna, Austria.

Akiya, N., and Savage, P.E., 2002. Roles of water for chemical reactions in high-temperature water. *Chem. Rev.* 102: 2725–2750.

Alcorn, C.D., Brodovitch, J.-C., Percival, P.W., Smith, M., and Ghandi, K., 2014. Kinetics of the reaction between $H^{\bullet}$ and superheated water probed with muonium. *Chem. Phys.* 435: 29–39.

Amichai, O., and Treinin, A., 1969. Chemical reactivity of $O(^3P)$ atoms in aqueous solution. *Chem. Phys. Lett.* 3: 611–613.

Anderson, D.W., 1984. *Absorption of Ionizing Radiation*. University Park Press, Baltimore, MD.

Anderson, A.R., and Hart, E.J., 1961. Molecular product and free radical yields in the decomposition of water by protons, deuterons, and helium ions. *Radiat. Res.* 14: 689–704.

Andresen, P.L., Ford, F.P., Murphy, S.M., and Perks, J.M., 1991. State of knowledge of radiation effects on environmental cracking in light water reactor core materials. *Proceedings of the Fourth International Symposium on Environmental Degradation of Materials in Nuclear Power Systems – Water Reactors, Jekyll Island, Georgia, August 1989*. National Association of Corrosion Engineers (NACE), pp. 1–83 through 1–121.

Anisimov, M.A., Sengers, J.V., and Levelt Sengers, J.M.H., 2004. Near-critical behavior of aqueous systems. In: *Aqueous Systems at Elevated Temperatures and Pressures: Physical Chemistry in Water, Steam and Hydrothermal Solutions* (Palmer, D.A., Fernández-Prini, R., and Harvey, A.H., Eds.), chap. 2, pp. 29–72. Elsevier, Amsterdam.

Antal, M.J., Jr., Brittain, A., DeAlmeida, C., Ramayya, S., and Roy, J.C., 1987. Heterolysis and homolysis in supercritical water. In: *Supercritical Fluids* (Squires,

T.G., and Paulaitis, M.E., Eds.). ACS Symposium Series, vol. 329, chap. 7, pp. 77–86. American Chemical Society, Washington, D.C.

Anzai, H., Nakata, K., Kuniya, J., and Hattori, S., 1994. The effect of hydrogen peroxide on the stress corrosion cracking of 304 stainless steel in high temperature water. *Corros. Sci.* 36: 1201–1207.

Autsavapromporn, N., 2006. The effects of pH and radiation quality (LET) on the radiolysis of liquid water and aqueous solutions: A study by using Monte Carlo simulations. M.Sc. thesis, Burapha University, Bangsaen, Chonburi, Thailand.

Balasubramanian, B., Pogozelski, W.K., and Tullius, T.D., 1998. DNA strand breaking by the hydroxyl radical is governed by the accessible surface areas of the hydrogen atoms of the DNA backbone. *Proc. Natl. Acad. Sci. U.S.A.* 95: 9738–9743.

Baldock, C., 2009. Historical overview of the development of gel dosimetry: Another personal perspective. *J. Phys.: Conf. Ser.* 164: 012002.

Bandura, A.V., and Lvov, S.N., 2006. The ionization constant of water over wide ranges of temperature and density. *J. Phys. Chem. Ref. Data* 35: 15–30.

Bartels, D.M., 2009. Comment on the possible role of the reaction $H^{\bullet} + H_2O \rightarrow H_2 + {}^{\bullet}OH$ in the radiolysis of water at high temperatures. *Radiat. Phys. Chem.* 78: 191–194.

Bethe, H., 1930. Zur Theorie des Durchgangs schneller Korpuskularstrahlen durch Materie. *Ann. Physik* 397: 325–400.

Bethe, H.A., and Ashkin, J., 1953. Passage of radiations through matter. In: *Experimental Nuclear Physics* (Segrè, E., Ed.), vol. 1, pp. 166–357. Wiley, New York.

Biedenkapp, D., Hartshorn, L.G., and Bair, E.J., 1970. The $O(^1D) + H_2O$ reaction. *Chem. Phys. Lett.* 5: 379–380.

Biersack, J.P., and Eckstein, W., 1984. Sputtering studies with the Monte Carlo program TRIM.SP. *Appl. Phys. A* 34: 73–94.

Bichsel, H., and Hiraoka, T., 1992. Energy loss of 70 MeV protons in elements. *Nucl. Instrum. Methods Phys. Res. B* 66: 345–351.

Blum, J., and Fridovich, I., 1985. Inactivation of glutathione peroxidase by superoxide radical. *Arch. Biochem. Biophys.* 240: 500–508.

Bohr, N., 1913. On the theory of the decrease of velocity of moving electrified particles on passing through matter. *Phil. Mag.* 25: 10–31.

Boscolo, D., Krämer, M., Durante, M., Fuss, M.C., and Scifoni, E., 2018. TRAX-CHEM: A pre-chemical and chemical stage extension of the particle track structure code TRAX in water targets. *Chem. Phys. Lett.* 698: 11–18.

Both, G., Krotz, R., Lohmer, K., and Neuwirth, W., 1983. Density dependence of stopping cross sections measured in liquid ethane. *Phys. Rev. A* 28: 3212–3216.

Boulanouar, O., Fromm, M., Mavon, C., Cloutier, P., and Sanche, L., 2013. Dissociative electron attachment to DNA-diamine thin films: Impact of the DNA close environment on the OH^- and O^- decay channels. *J. Chem. Phys.* 139: 055101.

Bragg, W.H., and Kleeman, R., 1905. On the α particles of radium, and their loss of range in passing through various atoms and molecules. *Phil. Mag.* 10: 318–340.

Brocklehurst, B., 1977. Ion-pair clusters and excited-state yields in radiolysis. *Nature* 265: 613–614.

Burns, W.G., and Sims, H.E., 1981. Effect of radiation type in water radiolysis. *J. Chem. Soc., Faraday Trans. 1* 77: 2803–2813.

Bursulaya, B.D., and Kim, H.J., 1999. Molecular dynamics simulation study of water near critical conditions. II. Dynamics and spectroscopy. *J. Chem. Phys.* 110: 9656–9665.

Burton, M., 1969. Radiation chemistry: A god fatherly look at its history and its relation to liquids. *Chem. Eng. News* 47: 86–96.

Butarbutar, S.L., Meesungnoen, J., Guzonas, D., Stuart, C.R., and Jay-Gerin, J.-P., 2014*a*. Modeling the radiolysis of supercritical water by fast neutrons: Density dependence of the yields of primary species at 400 °C. *Radiat. Res.* 182: 695–704.

Butarbutar, S.L., Sanguanmith, S., Meesungnoen, J., Sunaryo, G.R., and Jay-Gerin, J.-P., 2014*b*. Calculation of the yields for the primary species formed from the radiolysis of liquid water by fast neutrons at temperatures between 25-350 °C. *Radiat. Res.* 181: 659–665.

Byakov, V.M., and Stepanov, S.V., 2006. The mechanism for the primary biological effects of ionizing radiation. Phys. Usp. 49: 469–487.

Cadet, J., Wagner, J.R., Shafirovich, V., and Geacintov, N.E., 2014. One-electron oxidation reactions of purine and pyrimidine bases in cellular DNA. *Int. J. Radiat. Biol.* 90: 423–432.

Cai, J., Renault, C., and Gou, J., 2014. Supercritical water-cooled reactors. In: *Science and Technology of Nuclear Installations*, vol. 2014, article ID 548672, pp. 1–2. Hindawi Publishing Corp., London, UK.

Canıaz, R.O., and Erkey, C., 2014. Process intensification for heavy oil upgrading using supercritical water. *Chem. Eng. Res. Des.* 92: 1845–1863.

Cattant, F., Crusset, D., and Féron, D., 2008. Corrosion issues in nuclear industry today. *Materialstoday* 11: 32–37.

Chatterjee, A., and Schaefer, H.J., 1976. Microdosimetric structure of heavy ion tracks in tissue. *Radiat. Environ. Biophys.* 13: 215–227.

Chatterjee, A., Maccabee, H.D., and Tobias, C.A., 1973. Radial cutoff LET and radial cutoff dose calculations for heavy charged particles in water. *Radiat. Res.* 54: 479–494.

Choudhry, K.I., Kallikragas, D.T., and Svishchev, I.M., 2016. On the thermochemical hydrogen release rate and activity transport in a supercritical water-cooled reactor. *Mater. Corros.* 67: 804–809.

Clifford, P., Green, N.J.B., Oldfield, M.J., Pilling, M.J., and Pimblott, S.M., 1986. Stochastic models of multi-species kinetics in radiation-induced spurs. *J. Chem. Soc., Faraday Trans. 1* 82: 2673–2689.

Cobut, V., 1993. Simulation Monte Carlo du transport d'électrons non relativistes dans l'eau liquide pure et de l'évolution du milieu irradié: rendements des espèces créées de 10^{-15} à 10^{-7} s. Ph.D. thesis, Université de Sherbrooke, Sherbrooke, Québec, Canada,

Cobut, V., Jay-Gerin, J.-P., Frongillo, Y., and Patau, J.P., 1996. On the dissociative electron attachment as a potential source of molecular hydrogen in irradiated liquid water. *Radiat. Phys. Chem.* 47: 247–250.

Cobut, V., Frongillo, Y., Patau, J.P., Goulet, T., Fraser, M.-J., and Jay-Gerin, J.-P., 1998. Monte Carlo simulation of fast electron and proton tracks in liquid water–I. Physical and physicochemical aspects. *Radiat. Phys. Chem.* 51: 229–243.

Cohen, P., 1980. *Water Coolant Technology of Power Reactors*. American Nuclear Society, La Grange Park, IL.

Cook, W.G., and Olive, R.P., 2012*a*. Pourbaix diagrams for the iron-water system extended to high-subcritical and low-supercritical conditions. *Corros. Sci.* 58: 284–290.

Cook, W.G., and Olive, R.P., 2012*b*. Pourbaix diagrams for chromium, aluminum and titanium extended to high-subcritical and low-supercritical conditions. *Corros. Sci.* 58: 291–298.

Cook, W.G., and Lister, D.H., 2014. Chemistry in CANDU process systems. In: *The Essential CANDU* (Garland, W., Ed.), chap. 15. University Network of Excellence in Nuclear Engineering (UNENE), CANDU Owners Group, McMaster University, Hamilton, Ontario, Canada.

Čuba, V., Múčka, V., and Pospíšil, M., 2012. Radiation induced corrosion of nuclear fuel and materials. In: *Advances in Nuclear Fuel* (Revankar, S.T., Ed.), chap. 2, pp. 27–52. IntechOpen, London, UK.

Curie, P., and M^{me} Curie, S., 1898*a*. Sur une substance nouvelle radio-active, contenue dans la pechblende. *C. R. Acad. Sci. Paris* 127: 175–178.

Curie, P., M^{me} Curie, P., and Bémont, G., 1898*b*. Sur une nouvelle substance fortement radio-active, contenue dans la pechblende. *C. R. Acad. Sci. Paris* 127: 1215–1217.

Danzker, M., Kessaris, N.D., and Laughlin, J.S., 1959. Absorbed dose and linear energy transfer in radiation experiments. *Radiology* 72: 51–61.

Daub, K., Zhang, X., Noël, J.J., and Wren, J.C., 2011. Gamma-radiation-induced corrosion of carbon steel in neutral and mildly basic water at 150 °C. *Corros. Sci.* 53: 11–16.

Davies, M.J., 2005. The oxidative environment and protein damage. *Biochim. Biophys. Acta* 1703: 93–109.

Debierne, A., 1914. Recherches sur les gaz produits par les substances radioactives. Décomposition de l'eau, *Ann. Phys.* 2: 97–127.

Denifl, S., Ptasińska, S., Probst, M., et al., 2004. Electron attachment to the gas-phase DNA bases cytosine and thymine, *J. Phys. Chem. A* 108: 6562–6569.

Dexter, D.T., and Jenner, P., 2013. Parkinson disease: From pathology to molecular

disease mechanisms. *Free Radic. Biol. Med.* 62: 132–144.

Dingfelder, M., Inokuti, M., and Paretzke, H.G., 2000. Inelastic-collision cross sections of liquid water for interactions of energetic protons. *Radiat. Phys. Chem.* 59: 255–275.

Dingfelder, M., Ritchie, R.H., Turner, J.E., Friedland, W., Paretzke, H.G., and Hamm, R.N., 2008. Comparisons of calculations with PARTRAC and NOREC: Transport of electrons in liquid water. *Radiat. Res.* 169: 584–594.

Einstein, A., 1956. *Investigations on the Theory of the Brownian Movement*. Dover Publications, New York.

El-Ghossain, M.O., 2017. Calculations of stopping power, and range of electrons interaction with different material and human body parts. *Int. J. Sci. Technol. Res.* 6: 114–118.

El-Missiry, M.A., Fayed, T.A., El-Sawy, M.R., and El-Sayed, A.A., 2007. Ameliorative effect of melatonin against gamma-irradiation-induced oxidative stress and tissue injury. *Ecotoxicol. Environ. Saf.* 66: 278–286.

Elliot, A.J., and Bartels, D.M., 2009. The reaction set, rate constants and *g*-values for the simulation of the radiolysis of light water over the range 20 ° to 350 °C based on information available in 2008. AECL Report No. 153-127160-450-001. Atomic Energy of Canada Limited, Mississauga, Ontario, Canada.

Emfietzoglou, D., Papamichael, G., and Moscovitch, M., 2001. Charged particle interactions in water: Cross-sections and simulations. *Radiat. Phys. Chem.* 61: 597–98.

Ershov, B.G., Milaev, A.I., Petrosyan, V.G., Kartashov, N.I., Glasunov, P.Ya., and Tevlin, S.A., 1985. The effect of radiation on corrosion of steel in high-temperature water. *Radiat. Phys. Chem.* 26: 587–590.

Esmaili, S., Bass, A.D., Cloutier, P., Sanche, L., Huels, M.A., 2018. Glycine formation in CO_2:CH_4:NH_3 ices induced by 0-70 eV electrons. *J. Chem. Phys.* 148: 164702.

Fedor, J., Cicman, P., Coupier, B., et al., 2006. Fragmentation of transient water anions following low-energy electron capture by H_2O/D_2O. *J. Phys. B: At., Mol. Opt. Phys.* 39: 3935–3944.

Ferradini, C., 1979. Actions chimiques des radiations ionisantes. *J. Chim. Phys.* 76:

636–644.

Ferradini, C., and Jay-Gerin, J.-P., 1999. La radiolyse de l'eau et des solutions aqueuses : historique et actualité. *Can. J. Chem.* 77: 1542–1575.

Fontana, M.G., 2008. *Corrosion Engineering*. 3rd edn. McGraw-Hill India.

Fricke, H., and Hart, E.J., 1966. Chemical dosimetry. In: *Radiation Dosimetry* (Attix, F.H., and Roesch, W.C., Eds.). 2nd edn, vol. II, pp. 167–239. Academic Press, New York.

Fricke, H., and Morse, S., 1927. The chemical action of Roentgen rays on dilute ferrosulphate solutions as a measure of dose. *Am. J. Roentgenol. Rad. Therapy* 18: 430–432.

Fricke, H., and Morse, S., 1929. The action of X-rays on ferrous sulphate solutions. *Phil. Mag., 7th Ser*. Vol. 7: 129–141.

Fricke, H., 1935. The chemical properties of X-ray-activated molecules with special reference to the water molecule. *Cold Spring Harbor Symp.* 3: 55–63.

Fritz, K.S., and Petersen, D.R., 2011. Exploring the biology of lipid peroxidation-derived protein carbonylation. *Chem. Res. Toxicol.* 24: 1411–1419.

Frongillo, Y., Goulet, T., Fraser, M.-J., Cobut, V., Patau, J.P., and Jay-Gerin, J.-P., 1998. Monte carlo simulation of fast electron and proton tracks in liquid water–II. Nonhomogeneous chemistry. *Radiat. Phys. Chem.* 51: 245–254.

Galkin, A.A., and Lunin, V.V., 2005. Subcritical and supercritical water: A universal medium for chemical reactions. *Russian Chem. Rev.* 74: 21–35.

Ganchenkova, M.G., Yagodzinskyy, Y.N., Borodin, V.A., and Hänninen, H., 2014. Effects of hydrogen and impurities on void nucleation in copper: Simulation point of view. *Phil. Mag.* 94: 3522–3548.

Ghandi, K., and Percival, P.W., 2003. Prediction of rate constants for reactions of the hydroxyl radical in water at high temperatures and pressures. *J. Phys. Chem. A* 107: 3005–3008.

GIF, 2002. A technology roadmap for Generation IV nuclear energy systems. GIF-002-00.

GIF, 2014. Technology roadmap update for Generation IV nuclear energy systems. Publication prepared by the Nuclear Energy Agency of the Organisation for

Economic Co-operation and Development (OECD) on behalf of the Generation IV International Forum (GIF). https://www.gen-4.org/gif/jcms/c_9260/public.

Girotti, A.W., 1998. Lipid hydroperoxide generation, turnover, and effector action in biological systems. *J. Lipid Res.* 39: 1529–1542.

Goldberg, S.M., and Rosner, R., 2011. *Nuclear Reactors: Generation to Generation*. American Academy of Arts and Sciences, Cambridge, MA.

Gordon, S., Schmidt, K.H., and Honekamp, J.R., 1983. An analysis of the hydrogen bubble concerns in the three-mile island unit-2 reactor vessel. *Radiat. Phys. Chem.* 21: 247–258.

Goulet, T., and Jay-Gerin, J.-P., 1988. Thermalization distances and times for subexcitation electrons in solid water. *J. Phys. Chem.* 92: 6871–6874.

Goulet, T., and Jay-Gerin, J.-P., 1989. Thermalization of subexcitation electrons in solid water. *Radiat. Res.* 118: 46–62.

Goulet, T., and Jay-Gerin, J.-P., 1992. On the reactions of hydrated electrons with $^{\bullet}OH$ and H_3O^+. Analysis of photoionization experiments. *J. Chem. Phys.* 96: 5076–5087.

Goulet, T., Jay-Gerin, J.-P., Frongillo, Y., Cobut, V., and Fraser, M.-J., 1996. Rôle des distances de thermalisation des électrons dans la radiolyse de l'eau liquide. *J. Chim. Phys.* 93: 111–116.

Goulet, T., Patau, J.P., and Jay-Gerin, J.-P., 1990. Influence of the parent cation on the thermalization of subexcitation electrons in solid water. *J. Phys. Chem.* 94: 7312–7316.

Goulet, T., Jay-Gerin, J.-P., Frongillo, Y., Cobut, V., and Fraser, M.-J., 1996. Rôle des distances de thermalisation des électrons dans la radiolyse de l'eau liquide. *J. Chim. Phys.* 93: 111–116.

Green, N.J.B., Pilling, M.J., Pimblott, S.M., and Clifford, P., 1990. Stochastic modeling of fast kinetics in a radiation track. *J. Phys. Chem.* 94: 251–258.

Guzonas, D., Wills, J., Dole, H., Michel, J., Jang, S., Haycock, M., and Chutumstid, M., 2010. Steel corrosion in supercritical water: An assessment of the key parameters. *Proceedings of the 2nd Canada-China Joint Workshop on Supercritical-Water-Cooled Reactors, Toronto, Ontario, Canada, April 25-28*. Canadian Nuclear

Society, Toronto, Ontario, Canada. ISBN: 0-919784-98-4.

Guzonas, D., and Cook, W.G., 2012. Cycle chemistry and its effect on materials in a supercritical water-cooled reactor: A synthesis of current understanding. *Corros. Sci.* 65: 48–66.

Guzonas, D., Novotny, R., Penttilä, S., Toivonen, A., and Zheng, W., 2018. *Materials and Water Chemistry for Supercritical Water-cooled Reactors*. Elsevier Ltd., Duxford, UK.

Haimovitz-Friedman, A., Kan, C.C., Ehleiter, D., et al., 1994. Ionizing radiation acts on cellular membranes to generate ceramide and initiate apoptosis. *J. Exp. Med.* 180: 525–535.

Harrison, R.L., 2010. Introduction to Monte Carlo simulation. *AIP Conf. Proc.* 1204: 17–21. doi:10.1063/1.3295638.

Hart, E.J., and Anbar, M., 1970. *The Hydrated Electron*. Wiley-Interscience, New York.

Hart, E.J., and Boag, J.W., 1962. Absorption spectrum of the hydrated electron in water and in aqueous solutions. *J. Am. Chem. Soc.* 84: 4090–4095.

Hatano, Y., Katsumura, Y., and Mozumder, A. (Eds.), 2011. *Charged Particle and Photon Interactions with Matter : Recent Advances, Applications, and Interfaces*. Taylor & Francis Group, Boca Raton, FL.

Heller, J.M., Hamm, R.N., Birkhoff, R.D., and Painter, L.R., 1974. Collective oscillation in liquid water. *J. Chem. Phys.* 60: 3483–3486.

Hensley, K., Carney, J.M., Mattson, M.P., et al., 1994. A model for beta-amyloid aggregation and neurotoxicity based on free radical generation by the peptide: Relevance to Alzheimer disease. *Proc. Natl. Acad. Sci. U.S.A.* 91: 3270–3274.

Herbert, J.M., and Coons, M.P., 2017. The hydrated electron. *Annu. Rev. Phys. Chem*. 68: 447–472.

Hervé du Penhoat, M.-A., Goulet, T., Frongillo, Y., Fraser, M.-J., Bernat, Ph., and Jay-Gerin, J.-P., 2000. Radiolysis of liquid water at temperatures up to 300 °C: A Monte Carlo simulation study. *J. Phys. Chem. A* 104: 11757–11770.

Hoffmann, M.M., and Conradi, M.S., 1997. Are there hydrogen bonds in supercritical water? *J. Am. Chem. Soc.* 119: 3811–3817.

IAEA, 2011. Stress corrosion cracking in light water reactors: Good practices and lessons learned. IAEA-Nuclear Energy Series No. NP-T-3.13. International Atomic Energy Agency, Vienna, Austria.

IAEA-TECDOC-799, 1995. Atomic and molecular data for radiotherapy and radiation research. International Atomic Energy Agency, Vienna, Austria.

Ichino, T., and Fessenden, R.W., 2007. Reactions of hydrated electron with various radicals: Spin factor in diffusion-controlled reactions. *J. Phys. Chem. A* 111: 2527–2541.

ICRU Report 16, 1970. *Linear Energy Transfer*. International Commission on Radiation Units and Measurements, Washington, D.C.

ICRU Report 55, 1996. *Secondary electron spectra from charged particle interactions.* International Commission on Radiation Units and Measurements, Bethesda, MD.

Inokuti, M., 1971. Inelastic collisions of fast charged particles with atoms and molecules: The Bethe theory revisited. *Rev. Mod. Phys.* 43: 297–347.

Islam, M.M., Lertnaisat, P., Meesungnoen, J., Sanguanmith, S., Jay-Gerin, J.-P., Katsumura, Y., Mukai, S., Umehara, R., Shimizu, Y., and Suzuki, M., 2017. Monte Carlo track chemistry simulations of the radiolysis of water induced by the recoil ions of the $^{10}B(n,\alpha)^{7}Li$ nuclear reaction. 1. Calculation of the yields of primary species up to 350 °C. *RSC Adv.* 7: 10782–10790.

Islam, M.M., Kanike, V., Meesungnoen, J., Lertnaisat, P., Katsumura, Y., and Jay-Gerin, J.-P., 2018. *In situ* generation of ultrafast transient "acid spikes" in the $^{10}B(n,\alpha)^{7}Li$ radiolysis of water. *Chem. Phys. Lett.* 693: 210–215.

Jarczyk, L., Knoepfel, H., Lang, J., Müller, R., and Wolfli, W., 1961. The nuclear reactor as a high intensity source for discrete gamma rays up to 11 MeV. *Nucl. Instrum. Methods* 13: 287–296.

Jonah, C.D., and Rao, B.S.M. (Eds.), 2001. *Radiation Chemistry: Present Status and Future Trends*. Elsevier, Amsterdam.

Jonah, C.D., 1995. A short history of the radiation chemistry of water. *Radiat. Res.* 144: 141–147.

Kallikragas, D., Guzonas, D., and Svishchev, I., 2015. Properties of aqueous systems relevant to the SCWR via molecular dynamics simulations. *AECL Nucl. Rev.* 4: 9–

22.

Kanike, V., Meesungnoen, J., and Jay-Gerin, J.-P., 2015. Acid spike effect in spurs/tracks of the low/high linear energy transfer radiolysis of water: Potential implications for radiobiology. *RSC Adv.* 5: 43361–43370.

Kanike, V., Meesungnoen, J., Sanguanmith, S., Guzonas, D., Stuart, C.R., and Jay-Gerin, J.-P., 2017. Generation of ultrafast transient acid spikes in high-temperature water irradiated with low linear energy transfer radiation. *CNL Nucl. Rev.* 6: 31–40.

Kaplan, I.G., and Miterev, A.M., 1987. Interaction of charged particles with molecular medium and track effects in radiation chemistry. *Adv. Chem. Phys.* 68: 255–386.

Karamitros, M., Mantero, A., Incerti, S., et al., 2011. Modeling radiation chemistry in the Geant4 toolkit. *Prog. Nucl. Sci. Technol.* 2: 503–508.

Karpov, D.I., and Medvedev, D.A., 2016. Density dependence of dielectric permittivity of water and estimation of the electric field for the breakdown inception. *J. Phys.: Conf. Ser.* 754: 102004.

Kim, H., Mitton, D.B., and Latanision, R.M., 2010. Effect of pH and temperature on corrosion of nickel-base alloys in high temperature and pressure aqueous solutions. *J. Electrochem. Soc.* 157: C194–C199.

Kriksunov, L.B., and Macdonald, D.D., 1995. Corrosion in supercritical water oxidation systems: A phenomenological analysis. *J. Electrochem. Soc.* 142: 4069–4073.

Kriksunov, L.B., and Macdonald, D.D., 1997. Potential-pH diagrams for iron in supercritical water. *Corrosion* 53: 605–611.

Kritsky, V.G., 1999. *Water Chemistry and Corrosion of Nuclear Power Plant Structural Materials*. American Nuclear Society, La Grange Park, IL.

Kuppermann, A., 1959. Theoretical foundations of radiation chemistry. *J. Chem. Educ.* 36: 279–285.

Lamb, W.J., Hoffman, G.A., and Jonas, J., 1981. Self-diffusion in compressed supercritical water. *J. Chem. Phys.* 74: 6875–6880.

LaVerne, J.A., 2000. Track effects of heavy ions in liquid water. *Radiat. Res.* 153: 487–496.

LaVerne, J.A., 2004. Radiation chemical effects of heavy ions. In: *Charged Particle*

and Photon Interactions with Matter: Chemical, Physicochemical, and Biological Consequences with Applications (Mozumder, A., and Hatano, Y., Eds.), pp. 403–429. Marcel Dekker, New York.

LaVerne, J.A., 2005. H_2 formation from the radiolysis of liquid water with zirconia. *J. Phys. Chem. B* 109: 5395–5397.

LaVerne, J.A., and Pimblott, S.M., 1995. Electron energy-loss distributions in solid, dry DNA. *Radiat. Res.* 141: 208–215.

Lea, D.E., 1946. *Actions of Radiations on Living Cells*. Cambridge University Press, Cambridge, UK.

Lei, X., Li, H., Zhang, Y., and Zhang, W., 2013. Effect of buoyancy on the mechanism of heat transfer deterioration of supercritical water in horizontal tubes. *ASME J. Heat Trans.* 135: 071703.

Lin, M., Muroya, Y., Baldacchino, G., and Katsumura, Y., 2010. Radiolysis of supercritical water. In: *Recent Trends in Radiation Chemistry* (Wishart, J.F., and Rao, B.S.M., Eds.), pp. 255–277. World Scientific, Singapore.

Lister, D.H., and Cook, W.G., 2014. Nuclear plant materials and corrosion. In: *The Essential CANDU* (Garland, W., Ed.), chap. 14. University Network of Excellence in Nuclear Engineering (UNENE), CANDU Owners Group, McMaster University, Hamilton, Ontario, Canada.

Lister, D., and Uchida, S., 2015. Determining water chemistry conditions in nuclear reactor coolants. *J. Nucl. Sci. Technol.* 52: 451–466.

Liu, G., Du, T., Toth, L., Beninger, J., and Ghandi, K., 2016. Prediction of rate constants of important reactions in water radiation chemistry in sub- and supercritical water: Equilibrium reactions. *CNL Nucl. Rev.* 5: 345–361.

Liu, G., Landry, C., and Ghandi, K., 2018. Prediction of rate constants of important chemical reactions in water radiation chemistry in sub and supercritical water: Non-equilibrium reactions. *Can. J. Chem.* 96: 267–279.

Locatelli, G., Mancini, M., and Todeschini, N., 2013. Generation IV nuclear reactors: Current status and future prospects. *Energy Policy* 61: 1503–1520.

Lousada, C.M., Soroka, I.L., Yagodzinskyy, Y., et al., 2016. Gamma radiation induces hydrogen absorption by copper in water. *Sci. Rep.* 6: 24234. doi:

10.1038/srep24234.

Ma, J., Wang, F., Denisov, S.A., Adhikary, A., and Mostafavi, M., 2017. Reactivity of prehydrated electrons toward nucleobases and nucleotides in aqueous solution. *Sci. Adv.* 3: e1701669.

Madugundu, G.S., Wagner, R.J., Cadet, J., et al., 2013. Generation of guanine-thymine crosslinks in human cells by one-electron oxidation mechanisms. *Chem. Res. Toxicol.* 26: 1031–1033.

Magee, J.L., 1953. Radiation chemistry. *Annu. Rev. Nucl. Sci.* 3: 171–192.

Magee, J.L., and Chatterjee, A., 1987. Track reactions of radiation chemistry. In: *Kinetics of Nonhomogeneous Processes* (Freeman, G.R., Ed.), pp. 171-214. Wiley, New York.

Markovic, V., 1989. Radiation chemistry: Little known branch of science. *IAEA Bulletin* 20: 20–28.

Marsalek, O., Uhlig, F., VandeVondele, J., and Jungwirth, P., 2012. Structure, dynamics, and reactivity of hydrated electrons by ab initio molecular dynamics. *Acc. Chem. Res.* 45: 23–32.

Marshall, W.L., and Franck, E.U., 1981. Ion product of water substance, 0–1000 °C, 1–10,000 bars. New international formulation and its background. *J. Phys. Chem. Ref. Data* 10: 295–304.

Matsuyama, A., and Namiki, M., 1965. The evidence for the formation of chlorine atoms in neutral aqueous solution containing chloride ions by ionizing radiations. *Agr. Biol. Chem.* 29: 593–594.

McCracken, D.R., Tsang, K.T., and Laughton, P.J., 1998. Aspects of the physics and chemistry of water radiolysis by fast neutrons and fast electrons in nuclear reactors. Report AECL No. 11895. Atomic Energy of Canada Limited, Chalk River, Ontario, Canada.

Meesat, R., Sanguanmith, S., Meesungnoen, J., Lepage, M., Khalil, A., and Jay-Gerin, J.-P., 2012. Utilization of the ferrous sulfate (Fricke) dosimeter for evaluating the radioprotective potential of cystamine: Experiment and Monte Carlo simulation. *Radiat. Res.* 177: 813–826.

Meesungnoen, J., 2007. Effect of multiple ionization on the radiolysis of liquid water

irradiated with heavy ions: A theoretical study using Monte Carlo simulations. Ph.D. thesis, Université de Sherbrooke, Sherbrooke. Québec, Canada.

Meesungnoen, J., and Jay-Gerin, J.-P., 2005. High-LET radiolysis of liquid water with $^{1}H^{+}$, $^{4}He^{2+}$, $^{12}C^{6+}$, and $^{20}Ne^{9+}$ ions: Effects of multiple ionization. *J. Phys. Chem. A* 109: 6406–6419.

Meesungnoen, J., Guzonas, D., and Jay-Gerin, J.-P., 2010. Radiolysis of supercritical water at 400 °C and liquid-like densities near 0.5 g/cm^3 – A Monte Carlo calculation. *Can. J. Chem.* 88: 646–653.

Meesungnoen, J., and Jay-Gerin, J.-P., 2011. Radiation chemistry of liquid water with heavy ions: Monte Carlo simulation studies. In: *Charged Particle and Photon Interactions with Matter. Recent Advances, Applications, and Interfaces* (Hatano, Y., Katsumura, Y., and Mozumder, A., Eds.), pp. 355–400. Taylor & Francis Group, Boca Raton, FL.

Meesungnoen, J., Sanguanmith, S., and Jay-Gerin, J.-P., 2013. Density dependence of the yield of hydrated electrons in the low-LET radiolysis of supercritical water at 400 °C: Influence of the geminate recombination of subexcitation-energy electrons prior to thermalization. *Phys. Chem. Chem. Phys.* 15: 16450–16455.

Meesungnoen, J., Sanguanmith, S., and Jay-Gerin, J.-P., 2015. Yields of H_2 and hydrated electrons in low-LET radiolysis of water determined by Monte Carlo track chemistry simulations using phenol/N_2O aqueous solutions up to 350 °C. *RSC Adv.* 5: 76813–76824.

Metatla, N., Lafond, F., Jay-Gerin, J.-P., and Soldera, A., 2016. Heterogeneous character of supercritical water at 400 °C and different densities unveiled by simulation. *RSC Adv.* 6: 30484–30487.

Michaud, M., and Sanche, L., 1987. Absolute vibrational excitation cross sections for slow-electron (1-18 eV) scattering in solid H_2O. *Phys. Rev. A* 36, 4684-4699.

Michaud, M., Cloutier, P., and Sanche, L., 1991. Low-energy electron-energy-loss spectroscopy of amorphous ice: Electronic excitations. *Phys. Rev. A* 44: 5624–5627.

Mirsaleh Kohan, L., Sanguanmith, S., Meesungnoen, J., Causey, P., Stuart, C.R., and Jay-Gerin, J.-P., 2013. Self-radiolysis of tritiated water. 1. A comparison of the

effects of ^{60}Co γ-rays and tritium β-particles on water and aqueous solutions at room temperature. *RSC Adv.* 3: 19282–19299.

Mitton, D.B., Yoon, J.-H., Cline, J.A., et al., 2000. Corrosion behavior of nickel-based alloys in supercritical water oxidation systems. *Ind. Eng. Chem. Res.* 39: 4689–4696.

Morrison, P., 1952. Radiation in living matter: The physical processes. In: *Symposium on Radiobiology: The Basic Aspects of Radiation Effects on Living Systems (Oberlin College, June 14-18, 1950)* (Nickson, J.J., Ed.), pp. 1–12. Wiley, New York.

Mozumder, A., and Magee, J.L., 1966*a*. Model of tracks of ionizing radiations for radical reaction mechanisms. *Radiat. Res.* 28: 203–214.

Mozumder, A., and Magee, J.L., 1966*b*. Theory of radiation chemistry. VII. Structure and reactions in low LET tracks. *J. Chem. Phys.* 45: 3332–3341.

Mozumder, A., 1999. *Fundamentals of Radiation Chemistry*. Academic Press, San Diego, CA.

Mozumder, A., and Hatano, Y. (Eds.), 2004. *Charged Particle and Photon Interactions with Matter : Chemical, Physicochemical, and Biological Consequences with Applications*. Marcel Dekker, New York.

Muroya, Y., Meesungnoen, J., Jay-Gerin, J.-P., Filali-Mouhim, A., Goulet, T., Katsumura, Y., and Mankhetkorn, S., 2002. Radiolysis of liquid water: An attempt to reconcile Monte Carlo calculations with new experimental hydrated electron yield data at early times. *Can. J. Chem.* 80: 1367–1374.

Muroya, Y., Lin, M., de Waele, V., Hatano, Y., Katsumura, Y., and Mostafavi, M., 2010. First observation of picosecond kinetics of hydrated electrons in supercritical water. *J. Phys. Chem. Lett.* 1: 331–335.

Muroya, Y., Sanguanmith, S., Meesungnoen, J., Lin, M., Yan, Y., Katsumura, Y., and Jay-Gerin, J.-P., 2012. Time-dependent yield of the hydrated electron in subcritical and supercritical water studied by ultrafast pulse radiolysis and Monte Carlo simulation. *Phys. Chem. Chem. Phys.* 14: 14325–14333.

Muroya, Y., Yamashita, S., Lertnaisat, P., Sanguanmith, S., Meesungnoen, J., Jay-Gerin, J.-P., and Katsumura, Y., 2017. Rate Constant for the $H^{\bullet} + H_2O \rightarrow {}^{\bullet}OH + H_2$

reaction at elevated temperatures measured by pulse radiolysis. *Phys. Chem. Chem. Phys.* 19: 30834–30841.

Nakano, J., Kaji, Y., Yamamoto, M., and Tsukada, T., 2014. Effects of hydrazine addition and N_2 atmosphere on the corrosion of reactor vessel steels in diluted seawater under gamma-rays irradiation. *J. Nucl. Sci. Technol.* 51: 977–986.

Neeb, K.H., 1997. *The Radiochemistry of Nuclear Power Plants with Light Water Reactors*. de Gruyter, Berlin, Germany.

Nikjoo, H., O'Neill, P., Goodhead, D.T., and Terrissol, M., 1997. Computational modelling of low-energy electron-induced DNA damage by early physical and chemical events. *Int. J. Radiat. Biol.* 71: 467–483.

Nikjoo, H., Uehara, S., and Emfietzoglou, D., 2012. *Interaction of Radiation with Matter*. Taylor & Francis Group, Boca Raton, FL.

NIST Chemistry WebBook, 2018. NIST Standard Reference Data No. 69. National Institute of Standards and Technology, U.S. Department of Commerce, Washington, D.C.

Ogura, H., and Hamill, W.H., 1973. Positive hole migration in pulse-irradiated water and heavy water. *J. Phys. Chem.* 77: 2952–2954.

Pan, X., Cloutier, P., Hunting, D., and Sanche, L., 2003. Dissociative electron attachment to DNA. *Phys. Rev. Lett.* 90: 208102.

Paretzke, H.G., 1974. Comparison of track structure calculations with experimental results. *Proceedings of the Fourth Symposium on Microdosimetry, Verbania-Pallanza, Italy* (Booz, J., et al., Eds.), vol. 1, pp. 141–165. Euratom 5122 d-e-f, Luxembourg.

Pastina, B., and LaVerne, J.A., 2001. Effect of molecular hydrogen on hydrogen peroxide in water radiolysis. *J. Phys. Chem. A* 105: 9316–9322.

Pimblott, S.M., Pilling, M.J., and Green, N.J.B., 1991. Stochastic models of spur kinetics in water. *Radiat. Phys. Chem.* 37: 377–388.

Pioro, I., 2011. The potential use of supercritical water-cooling in nuclear reactors. In: *Nuclear Energy Encyclopedia: Science, Technology, and Applications* (Krivit, S.B., Lehr, J.H., and Kingery, T.B, Eds.), pp. 309–347. Wiley, Hoboken, NJ.

Pitzer, K.S., 1983. Dielectric constant of water at very high temperature and pressure.

Proc. Natl. Acad. Sci. USA 80: 4575–4576.

Plante, I., 2009. Développement de codes de simulation Monte Carlo de la radiolyse de l'eau et de solutions aqueuses par des électrons, ions lourds, photons et neutrons. Applications à divers sujets d'intérêt expérimental. Ph.D. thesis, Université de Sherbrooke, Sherbrooke. Québec, Canada.

Plante, I., and Devroye, L., 2017. Considerations for the independent reaction times and step-by-step methods for radiation chemistry simulations. *Radiat. Phys. Chem.* 139: 157–172.

Platzman, R.L., 1958. The physical and chemical basis of mechanisms in radiation biology. In: *Radiation Biology and Medicine. Selected Reviews in the Life Sciences* (Claus, W.D., Ed.), pp. 15–72. Addison-Wesley, Reading, MA.

Platzman, R.L., 1962*a*. Superexcited states of molecules. *Radiat. Res.* 17: 419–425.

Platzman, R.L., 1962*b*. Dissociative attachment of subexcitation electrons in liquid water, and the origin of radiolytic "molecular" hydrogen. In: *Abstracts of Papers, Second International Congress of Radiation Research, Harrogate, England*, p. 128.

Press, W.H., Teukolsky, S.A., Vetterling, W.T., and Flannery, B.P., 1992. *Numerical Recipes in Fortran. The Art of Scientific Computing*. 2nd edn. Cambridge University Press, Cambridge.

Ram, N.B., Prabhudesai, V.S., and Krishnakumar, E., 2009. Resonances in dissociative electron attachment to water. *J. Phys. B: At. Mol. Opt. Phys.* 42: 225203.

Ramos-Méndez, J., Perl, J., Schuemann, J., McNamara, A., Paganetti, H., and Faddegon, B., 2018. Monte Carlo simulation of chemistry following radiolysis with TOPAS-nBio. *Phys. Med. Biol.* 63: 105014.

Reed, A.B., 2011. The history of radiation use in medicine. *J. Vasc. Surg.* 53: 3S–5S.

Reisz, J.A., Bansal, N., Qian, J., Zhao, W., and Furdui, C.M., 2014. Effects of ionizing radiation on biological molecules – Mechanisms of damage and emerging methods of detection. *Antioxid. Redox Signal.* 21: 260–292.

Risse, O., 1930. Die physikalische Grundlagen der chemischen Wirkungen des Lichtes und der Röntgenstrahlen. *Ergebn. Physiol.* 30: 242–293.

Rinard, P.M., 1991. Neutron interactions with matter. In: *Passive Nondestructive Assay of Nuclear Materials* (Reilly, D., Ensslh, N., Smith, Jr., H., and Kreiner, S., Eds.),

chap. 12, pp. 357–378. Los Alamos Technical Report NuREG/cR-5550. U.S. Nuclear Regulatory Commission, Washington, D.C.

Röntgen, W.C., 1895. Über eine neue Art von Strahlen. *Sitzungsberichte der Physikalisch-Medizinischen Gesellschaft zu Würzburg*, No. 9, pp. 132–141.

Rudd, M.E., 1990. Cross sections for production of secondary electrons by charged particles. *Radiat. Prot. Dosim.* 31: 17–22.

Rudd, M.E., Kim, Y.-K., Madison, D.H., and Gay, T.J., 1992. Electron production in proton collisions with atoms and molecules: Energy distributions. *Rev. Mod. Phys.* 64: 441–490.

Sanguanmith, S., Muroya, Y., Meesungnoen, J., Lin, M., Katsumura, Y., Mirsaleh Kohan, L., Guzonas, D., Stuart, C.R., and Jay-Gerin, J.-P., 2011. Low-linear energy transfer radiolysis of liquid water at elevated temperatures up to 350 °C: Monte Carlo simulations. *Chem. Phys. Lett.* 508: 224–230.

Sanguanmith, S., Meesungnoen, J., and Jay-Gerin, J.-P., 2012. Density dependence of the "escape" yield of hydrated electrons in the low-LET radiolysis of supercritical water at 400 °C. *Phys. Chem. Chem. Phys.* 14: 11277–11280.

Sanguanmith, S., Meesungnoen, J., and Jay-Gerin, J.-P., 2013. Time-dependent yield of $^{\bullet}$OH radicals in the low linear energy transfer radiolysis of water between 25 and 350 °C. *Chem. Phys. Lett.* 588: 82–86.

Sanguanmith, S., Meesungnoen, J., Guzonas, D., Stuart, C.R., and Jay-Gerin, J.-P., 2016. Radiolysis of supercritical water at 400 °C: A sensitivity study of the density dependence of the yield of hydrated electrons on the (e^-_{aq} + e^-_{aq}) reaction rate constant. *J. Nucl. Eng. Radiat. Sci.* 2: 021014.

Satio, N., Tsuchiya, Y., Yamamoto, S., et al., 2006. Chemical thermodynamic considerations on corrosion products in supercritical-water-cooled reactor coolant. *Nucl. Technol.* 155: 105–113.

Satoh, T., Uchida, S., Sugama, J.-I., Yamashiro, N., Hirose, T., and Morishim, Y., 2004. Effects of hydrogen peroxide on corrosion of stainless steel, (I) Improved control of hydrogen peroxide remaining in a high temperature high pressure hydrogen peroxide loop. *J. Nucl. Sci. Technol.* 41: 610–618.

Şener, G., et al., 2006. Propylthiouracil-induced hypothyroidism protects ionizing

radiation-induced multiple organ damage in rats. *J. Endocrinology* 189: 257–269.

Sharma, K.K.K., Swarts, S.G., and Bernhard, W.A., 2011. Mechanisms of direct radiation damage to DNA: The effect of base sequence on base end products. *J. Phys. Chem. B* 115: 4843–4855.

Sigmund, P., 1982. Kinetic theory of particle stopping in a medium with internal motion. *Phys. Rev. A* 26: 2497–2517.

Simons, J., 2006. How do low-energy (0.1-2 eV) electrons cause DNA-strand breaks? *Acc. Chem. Res.* 39: 772–779.

Sims, H.E., Henshaw, J., and Bartels, D.M., 2013. Modelling the critical hydrogen concentration in the AECL test reactor. *Radiat. Phys. Chem.* 82: 16–24.

Sommerfeld, T., 2007. Doorway mechanism for dissociative electron attachment to fructose. *J. Chem. Phys.* 126: 124301.

Spinks, J.W.T, and Woods, R.J., 1990. *An Introduction to Radiation Chemistry*. 3rd edn. Wiley, New York.

Spohr, R., 1990. *Ion Tracks and Microtechnology: Principles and Applications*. Vieweg, Braunschweig, Germany.

Stenström, W., and Lohmann, A., 1933. Standardization of Roentgen dosage by means of methylene blue. *Radiology* 21: 29–36.

Sterniczuk, M., and Bartels, D.M., 2016. Source of molecular hydrogen in high-temperature water radiolysis. *J. Phys. Chem. A* 120: 200–209.

Stoller, R.E., Toloczko, M.B., Was, G.S., et al., 2013. On the use of SRIM for computing radiation damage exposure. *Nucl. Instrum. Methods Phys. Res. B* 310: 75–80.

Sunaryo, G.R., Katsumura, Y., and Ishigure, K., 1995. Radiolysis of water at elevated temperatures. III. Simulation of radiolytic products at 25 and 250 °C under the irradiation with γ-rays and fast neutrons. *Radiat. Phys. Chem.* 45: 703–714.

Swiatla-Wojcik, D., and Buxton, G.V., 1995. Modeling of radiation spur processes in water at temperatures up to 300 °C. *J. Phys. Chem.* 99: 11464–11471.

Swiatla-Wojcik, D., and Buxton, G.V., 1998. Modelling of linear energy transfer effects on track core processes in the radiolysis of water up to 300 °C. *J. Chem. Soc., Faraday Trans.* 94: 2135–2141.

Swiatla-Wojcik, D., and Buxton, G.V., 2010. Reply to comment on the possible role of the reaction $H^{\bullet} + H_2O \rightarrow H_2 + {}^{\bullet}OH$ in the radiolysis of water at high temperatures. *Radiat. Phys. Chem.* 79: 52–56.

Symons, M.C.R., 1994. Direct and indirect damage to DNA by ionising radiation. *Radiat. Phys. Chem.* 43: 403–405.

Tabata, Y., Ito, Y., and Tagawa, S. (Eds.), 1991. *CRC Handbook of Radiation Chemistry*. CRC Press, Boca Raton, FL.

Takiguchi, H., Ullberg, M., and Uchida, S., 2004. Optimization of dissolved hydrogen concentration for control of primary coolant radiolysis in pressurized water reactors. *J. Nucl. Sci. Technol.* 41: 601–609.

Taube, H., 1957. Photochemical reactions of ozone in solution. *Trans. Faraday Soc.* 53: 656–665.

Thomson, J.J., 1897. Cathode rays. *Phil. Mag.* 44: 293–316.

Thwaites, D.I., 1983. Bragg's rule of stopping power additivity: A compilation and summary of results. *Radiat. Res.* 95: 495–518.

Tippayamontri, T., Sanguanmith, S., Meesungnoen, J., Sunaryo, G.R., and Jay-Gerin, J.-P., 2009. Fast neutron radiolysis of the ferrous sulfate (Fricke) dosimeter: Monte Carlo simulations. *Recent Res. Devel. Physical Chem.* 10: 143–211.

Toburen, L.H., 2004. Ionization and secondary electron production by fast charged particles. In: *Charged Particle and Photon Interactions with Matter: Chemical, Physicochemical, and Biological Consequences with Applications* (Mozumder, A., and Hatano, Y., Eds.), pp. 31-74. Marcel Dekker, New York.

Toburen, L.H., 2014. Development of Monte Carlo track structure codes. https://three.jsc.nasa.gov/articles/Monte-Carlo-Track-Structure-Toburen.pdf.

Turner, J.E., Magee, J.L., Wright, H.A., Chatterjee, A., Hamm, R.N., and Ritchie, R.H., 1983. Physical and chemical development of electron tracks in liquid water. *Radiat. Res.* 96: 437–449.

Uchida, S., Naitoh, M., Uehara, Y., et al., 2008. Chemistry in surface boundary layers as related to flow accelerated corrosion of carbon steel in high temperature water. *ECS Trans.* 11: 13–26.

Uchida, S., 2008. Corrosion of structural materials and electrochemistry in high

temperature water of nuclear power systems. *Power Plant Chem.* 10: 630–649.

Uchida, S., and Katsumura, Y., 2013. Water chemistry technology – one of the key technologies for safe and reliable nuclear power plant operation. *J. Nucl. Sci. Technol.* 50: 346–362.

Uematsu, M., and Frank E.U., 1980. Static dielectric constant of water and steam. *J. Phys. Chem. Ref. Data* 9: 1291–1306.

Vaiente, M., Molina, W., Carrizales Silva, L., et al., 2016. Fricke gel dosimeter with improved sensitivity for low-dose-level measurements. *J. Appl. Clin. Med. Phys.* 17: 402–417.

Verma, M.P., 2003. A thermodynamic assessment of dissociation constant of water. *Proceedings of the Twenty-Eighth Workshop on Geothermal Reservoir Engineering, Stanford University, Stanford, California, January 27–29*. Paper No. SGP-TR-173.

von Sonntag, C., 2006. *Free-Radical-Induced DNA Damage and Its Repair: A Chemical Perspective*. Springer-Verlag, Berlin.

Walker, D.C., 1967. The hydrated electron. *Q. Rev. Chem. Soc.* 21: 79–108.

Wang, C.-R., Nguyen, J., and Lu, Q.-B., 2009. Bond breaks of nucleotides by dissociative electron transfer of nonequilibrium prehydrated electrons: A new molecular mechanism for reductive DNA damage. *J. Am. Chem. Soc.* 131: 11320–11322.

Was, G.S., Ampornrat, P., Gupta, G., Teysseyre, S., West, E.A., Allen, T.R., et al., 2007. Corrosion and stress corrosion cracking in supercritical water. *J. Nucl. Mater.* 371: 176–201.

Watt, D.E., and Alkharam, A.S., 1994. Charged particle track structure parameters for application in radiation biology and radiation chemistry. *Int. J. Quantum Chem.* 52: 195–207.

Weingärtner, H., and Franck, U.E., 2005. Supercritical water as a solvent. Angewandte Chemie Int. Ed. 44: 2672–2692.

Westacott, R.E., Johnston, K.P., and Rossky, P.J., 2001. Simulation of an S_N1 reaction in supercritical water. *J. Am. Chem. Soc.* 123: 1006–1007.

Willacy, M., 2013. Fukushima leak questions handling of nuclear plant crisis.

https://www.abc.net.au/7.30/fukushima-leak-questions-handling-of-nuclear-plant/4969818.

Wilson, C.D., Dukes, C.A., and Baragiola, R.A., 2001. Search for the plasmon in condensed water. *Phys. Rev. B* 63: 121101.

Yang, H., Jin, X., Kei Lam, C.W., and Yan, S.K., 2011. Oxidative stress and diabetes mellitus. *Clin. Chem. Lab. Med.* 49: 1773–1782.

Yetisir, M., Gaudet, M., Pencer, J., McDonald, M., Rhodes, D., Hamilton, H., and Leung, L., 2016. Canadian supercritical water-cooled reactor core concept and safety features. *CNL Nucl. Rev.* 5: 189–202.

Zaider, M., and Brenner, D.J., 1984. On the stochastic treatment of fast chemical reactions. *Radiat. Res.* 100: 245–256.

Zeigler, B.P., and Reynolds, R.G., 1985. A hierarchical information processing model for adaptation to technological change. *Syst. Res.* 2: 309–317.

Ziegler, J.F., Biersack, J.P., and Ziegler, M.D., 2015. *SRIM – The Stopping and Range of Ions in Matter*. SRIM Co., Chester, MD.

Ziegler, J.F., Ziegler, M.D., and Biersack, J.P., 2010. SRIM – The stopping and range of ions in matter (2010). *Nucl. Instrum. Methods Phys. Res. B* 268: 1818–1823.